COMPUTATIONAL ANALYSIS OF PATTERN GENERATION IN REDUCED VERTEBRATE MOTOR CIRCUIT MODELS

by

Abigail Snyder

B.S. Mathematics, University of Pittsburgh, 2010

M.A. Mathematics, University of Pittsburgh, 2012

Submitted to the Graduate Faculty of
the Kenneth P. Dietrich School of Arts and Sciences in partial fulfillment
of the requirements for the degree of

Doctor of Philosophy

University of Pittsburgh

2016

UNIVERSITY OF PITTSBURGH

DIETRICH SCHOOL OF ARTS AND SCIENCES

This dissertation was presented

by

Abigail Snyder

It was defended on

July 18th, 2016

and approved by

Jonathan E. Rubin, Department of Mathematics

G. Bard Ermentrout, Department of Mathematics

Brent Doiron, Department of Mathematics

Douglas J. Weber, Department of Physical Medicine and Rehabilitation

Dissertation Director: Jonathan E. Rubin, Department of Mathematics

COMPUTATIONAL ANALYSIS OF PATTERN GENERATION IN REDUCED VERTEBRATE MOTOR CIRCUIT MODELS

Abigail Snyder, PhD

University of Pittsburgh, 2016

Rhythmic behaviors such as breathing, walking, and scratching are vital to many species. Such behaviors can emerge from groups of neurons, called central pattern generators (CPGs), in the absence of rhythmic inputs. In vertebrates, the identification of the cells that constitute the CPG for particular rhythmic behaviors is difficult, and often, its existence has only been inferred. In the second and third chapters of this thesis, we use two reduced mathematical models to investigate the capability of a proposed network to generate multiple scratch rhythms observed in turtles. Under experimental conditions, intact turtles generate several rhythmic scratch motor patterns corresponding to non-rhythmic stimulation of different body regions. These patterns feature alternating phases of motoneuron activation that occur repeatedly, with different patterns distinguished by the relative timing and duration of activity of hip extensor, hip flexor, and knee extensor motoneurons. We show through simulation that the proposed network can achieve the desired multi-functionality, even though it relies on hip unit generators to recruit appropriately timed knee extensor motoneuron activity. We develop a phase space representation which we use to derive sufficient conditions for the network to realize each rhythm and which illustrates the role of a saddle-node bifurcation in achieving the knee extensor delay. This framework is harnessed to consider bistability and to make predictions about the responses of the scratch rhythms to input changes for future experimental testing. We also consider a stochastic spiking model to reproduce firing rate changes observed in experiment, explore the relative contributions of different parameters in the model to the observed changes, support our collaborators' hypothesis regarding these changes, and provide our collaborators with predictions for future experiments. In the fourth chapter of this thesis, we present a theoretical study examining whether three mechanisms suggested by deletion experiments can operate in the same CPG for an extensor-flexor pair in the mammalian central nervous system during locomotion. We arrive at unique solution properties produced by each of the three mechanisms for use in future experiments. Our findings propose explanations for the coexistence of the three experimentally suggested yet seemingly contradictory mechanisms for rhythmogenesis.

TABLE OF CONTENTS

LIST OF TABLES

LIST OF FIGURES

PREFACE

This dissertation was supported by NSF awards EMSW21-RTG 0739261, DMS-1021701, DMS-1312508. Content in Chapter 2 appeared in “Conditions for Multi-functionality in a Rhythm Generating Network Inspired by Turtle Scratching” in the Journal of Mathematical Neuroscience, vol. 5, 2015, copyright to Springer.

I am extremely grateful to my committee - Bard, Brent, and Doug - for their constructive criticism and helpful comments. Your advice has undoubtedly improved this work. A tremendous thank you to the collaborators I have worked with over the course of this dissertation: Ari Berkowitz, Ilya Rybak, and Jessica Ausborn. To my advisor, Jonathan Rubin, a thousand warm thank you’s. You were patient, kind, and understanding when many others would not have been. I hope to take the lessons I have learned from you in kindness, drive, and thoughtfulness with me as I move forward.

I would not have been able to complete this work without a huge support system, my supportive and loving parents, and my unbelievably understanding friends: Kate, Jill, Mark, Leah, Lucy, Glenn, Jeff, and others. To my father’s advisor, George - thank you for being foolish enough to guide another Snyder through their twenties. And to my partner, I cannot begin to express my gratitude for your love and my confusion that you still somehow like me after all of this.

1.0 INTRODUCTION

Research showing that the mammalian spinal cord can generate rhythmic stepping patterns without rhythmic input dates back to the work of T. G. Brown in the early twentieth century [10, 11]. This work contains the initial proposal of the half-center oscillator model of the spinal locomotor network: a motor pattern is generated by rhythmic alternation of flexor and extensor muscle activity in the absence of sensory afferents or rhythmic inputs. This approach was supported in experiments (largely recording from muscle nerves) throughout the next 100+ years: crayfish, newts, leeches, cockroaches, turtles, and cats have all been found to produce rhythmic motor patterns in the absence of sensory input [50, 46]. These experiments across a wide variety of species support the hypothesis that alternating flexor and extensor activity can be generated solely by the central nervous system without rhythmic inputs. These networks of neurons which produce rhythmic output in the absence of rhythmic input are referred to as *central pattern generators* (CPGs). CPGs are responsible for a variety of rhythmic behaviors such as walking, digesting, breathing, swimming, and scratching [1, 28, 27, 29].

Brown's half-center model has been implemented in many ways. In A. Lundberg's Half-Center hypothesis, two excitatory interneuron populations excite flexor and extensor motoneuron populations, and inhibit each other through excitation of inhibitory interneurons [40]. All flexor neurons at hip, knee, and ankle belong to the same flexor half-center, and all extensor neurons at those degrees of freedom belong to the same extensor half-center, thus fine details of many behaviors are lost. The Half-Center hypothesis predicts that there cannot be rhythmic activity of an agonist without alternating rhythmic activity of its antagonist; it also fails to explain motor patterns with mixed synergies such as the rostral scratch in turtle and the paw shake in cat [61].

A slightly different, yet still traditional network for a motor behavior hypothesizes that each major muscle group (knee, hip, etc.) is controlled by its own populations of flexor and extensor motoneurons. A network involving, for example, the hip and knee, would consist of four motoneuron populations corresponding to hip extensor, hip flexor, knee extensor, and knee flexor. Each of those populations would be activated by its own excitatory interneuron population, and those interneuron populations would interact with each other through inhibitory sub-populations. The nature of these interactions is currently unknown: due to the complexity of the vertebrate spinal cord, identifying all interneuron populations relevant to a given motor pattern (much less their interactions) is a difficult task for motor pattern physiologists [41]. An example of such an approach is the Unit-Burst-Generator (UBG) (sometimes referred to as Unit Pattern Generator or UPG) hypothesis for control of cat hindlimb stepping [28, 27]: each UBG is a module of neurons that control musculature for each possible direction of limb motion possible in an associated antagonist muscle pair. In the above example, there would be a hip extensor module consisting of motoneurons, excitatory interneurons, and inhibitory interneurons; there would be similar modules for hip flexor, knee extensor, and knee flexor. These modules would then interact with each other in generating a rhythm. This modular approach has been used in studying other systems such as stick insect, turtles, and lamprey [13, 51, 26].

In contrast to the alternating relationship between excitation and inhibition described above, concurrent excitation and inhibition is also an important feature of neuronal networks seen in experiments in lamprey, embryonic frogs, adult turtle, and neonatal rats [37, 19, 51, 3, 48], in addition to the cat. During some rhythms (e.g. during rostral scratching in turtle [51, 3]), each motoneuron receives concurrent excitation and inhibition, rather than alternating as above. One interpretation of this contrast is that the alternating/reciprocal and concurrent views of excitatory and inhibitory inputs to motoneurons represent features that do not coexist in the same network. There is, however, ample experimental evidence demonstrating both alternating and concurrent excitation and inhibition: some inhibition alternates with excitation, and other inhibition is concurrent with excitation during different phases of a motoneuron's activity. Additional experimental and theoretical work featuring both alternating and concurrent excitation and inhibition present in a single network are described in studies of the CPGs for sea slug feeding, lamprey, zebrafish and tadpole swimming, turtle scratching, and rodent locomotion [55, 37, 12, 25, 19, 51, 48, 47].

Additionally, the question of network multi-functionality must be considered: is a network capable of generating more than one motor pattern from the same muscles and motoneurons, or is there a unique CPG for each motor pattern an animal can generate? The latter seems inefficient and is not entirely supported by experimental evidence. Recordings in both invertebrate and vertebrate systems find that some interneurons are active in multiple rhythms generated by the same sets of muscles and motoneurons. Examples include tadpole swimming and struggling, mollusk withdrawal and escape swimming, cat scratching and walking, and in multiple forms of scratching in the turtle [32, 9, 45]. This evidence suggests that a single network of neurons can produce distinct motor patterns involving the same muscles under varying inputs. For invertebrate networks where complete connectivity diagrams have been produced (e.g. crustacean stomatogastric system), the nature of multi-functional networks can be fully understood [70]. However, the vertebrate nervous system is sufficiently large that the structure of the spinal network cannot easily be deduced from individual neuron recordings [41, 31].

Past theoretical research has focused on several different aspects that arise in multi-functionality, including the general organizing principles governing CPGs [39, 29], and the notion that an organism may exhibit different motor patterns by selecting different CPGs [34], which in turn may be collections of burst-capable unit CPGs that each control a set of synergistic muscles [27]. Synchronization ([58, 24]) and near-synchronization [8] in networks of planar neuron models with strong synaptic coupling have been well studied. However, distinct delays in onset of activity of one motoneuron population relative to another (such as are present in rostral scratch in turtles [50, 5, 51]) do not appear to be as well-examined. More quantitative approaches in deriving optimal CPG network structures [15, 2] and determining parameter values necessary to coordinate multiple CPGs to generate multiple rhythms [34] have been undertaken in systems with features amenable to use of an objective cost function.

Previous study of transitions between neurons during antiphase rhythm generation classified them by the “escape” and “release” mechanisms [20, 56, 69]; previous modeling efforts in the turtle found, among other results, that escape from reciprocal inhibition transitions were key in correctly generating the caudal scratch and forward swim movements [31]. The escape mechanism occurs when the silent cell is able to overcome the inhibition it receives and enter the active phase. In the case of differential equations resulting in cubic voltage nullclines, this happens when the silent neuron has access to or gets above (in the case of persistent sodium currents) the left knee of its cubic nullcline. Whether this access is intrinsic to the neuron or arises as a result of inhibition to the silent cell decaying depends on the parameters used in a given model. The release mechanism occurs when the active cell transitions from the active to the silent phase and releases the inhibited cell. In the case of differential equations resulting in cubic voltage nullclines, this happens when the active neuron has access to or gets below (in the case of persistent sodium currents) the right knee of its cubic nullcline. Again, this access may be either intrinsic to the active neuron or may be the result of synaptic interactions. Examples of these transitions are given in a variety of different nullcline configurations throughout this thesis and are shaped by the model parameters implemented. Individually, when transitions occur by escape, increased excitatory drive leads to an increase in frequency of the resulting oscillation; when transitions occur by release, increased excitatory drive leads to a decrease in frequency of the resulting oscillation. When a combination of escape and release is involved, the effect of excitatory drive on oscillation frequency is more difficult to predict.

We examine the capabilities of reduced, mathematical models of vertebrate motor circuits that incorporate may of these features to display multi-functionality. In Chapter 2, we will examine the capability of a reduced, hip-dominated neuronal network to generate two distinct scratching rhythms in the adult red-eared turtle. Our experimental collaborators proposed a network in which hip-related interneurons also project to knee extensor motoneurons to explain their experimental findings of individual interneurons activating in both pocket and rostral scratching behaviors [5]. In previous work [57], we presented a model of this network, demonstrated that it was capable of producing multi-functional outputs in response to differing inputs, and we derived sufficient conditions for rhythm selection. We developed a slow phase plane framework that we used to make additional predictions for our experimental collaborators, and that can be used to analyze similar problems. We also indicate some limitations of our relaxation oscillator modeling approach and directions for future research. These published results are included here. In Chapter 3, we will address some of the limitations of the model in Chapter 2. We will introduce a stochastic spiking model that imposes fewer requirements on interneuron populations in the network architecture introduced in [5]. We will use this model to reproduce firing rate changes observed in experiment, explore the relative contributions of different parameters in the model to the observed changes, support our collaborators' hypothesis regarding these changes, and provide our collaborators with predictions for future experiments. We will finish with a discussion of this approach's shortcomings, and the mathematical methods we use in our parameter explorations.

One of the interesting features seen in vertebrate motor patterns is deletions: one extensor or flexor population ceases for a period during normal rhythm generation before returning to activity. During a variety of deletions during rostral scratch in turtle and during stepping in cats [16, 61, 11, 54, 42], when either the extensor or flexor motoneuron ceases for a period, the other becomes tonically active. This suggests that tonic activity may be the intrinsic behavior of an isolated motoneuron, and that it is the inhibitory interaction between the extensor and flexor related interneurons that generate rhythmic activity. In other words, these experimental findings support the traditional half-center oscillator approach developed by Brown [11] and provide experimental support that rhythmic spinal CPGs have modular organization. Other experimental findings seem to indicate that some CPGs or CPG modules are actually intrinsically rhythmogenic. Studies in mouse spinal cord and in cat suggest a flexor-dominated CPG organization in which the flexor module has intrinsic rhythmic capabilities and the extensor module is intrinsically tonic [71, 21]. Finally, some recent optogenetic experiments in mice in which excitatory and inhibitory interneurons are genetically targeted for controlled activation have suggested that both the extensor and flexor modules possess intrinsic rhythmic properties. This local rhythmic activity is hypothesized to be recruited during motor behaviors to form a network of rhythm generators [30].

To study this phenomenon, we extend our focus beyond turtle results to examine more general behavior of extensor-flexor pairs. In Chapter 4, we will present a theoretical study examining whether all three of the mechanisms suggested by deletion experiments can operate in the same CPG, and arrive at unique solution properties produced by each of the three mechanisms for use in future experiments. We will introduce a reduced mathematical model in which both extensor and flexor neurons are represented by single non-spiking neurons coupled by mutual inhibition for qualitative analysis of system dynamics. This reduced model produces stable rhythmic patterns in both symmetric and asymmetric network structures, and we examine frequency modulation as external drive to one or both half-centers in this model varies. Our findings suggest different regimes in locomotor CPG operation and proposes explanation for the coexistence of the three experimentally suggested yet seemingly contradictory mechanisms for rhythmogenesis. We will finish with a discussion of this approach's shortcomings and directions for future study.

2.0 CONDITIONS FOR MULTI-FUNCTIONALITY IN A RHYTHM GENERATING NETWORK INSPIRED BY TURTLE SCRATCHING

In this chapter, we employ mathematical modeling to explore the multi-functionality of a single neuronal network underlying two distinct scratching rhythms in turtles. Under experimental conditions, intact red-eared turtles are observed to generate a variety of rhythmic motor patterns corresponding to stimulation of different body regions (including caudal scratch, rostral scratch, pocket scratch, and forward swim; see Figure 1) [4]. All of these patterns feature alternating phases of motoneuron activation that occur repeatedly, while different patterns are distinguished by the relative timing and duration of activity of hip extensor motoneurons, hip flexor motoneurons and knee extensor motoneurons. Notably, these stable, rhythmic behaviors arise in the absence of rhythmic stimulation, suggesting that a central pattern generator (CPG) may be responsible. Spinalized turtles, in which motor pathways from higher brain areas have been cut, display corresponding fictive behaviors in response to the same forms of stimulation, which suggests that necessary components for rhythm generation are present in the brain stem and spinal cord [50, 51, 5, 4]. However, even with restriction to these areas, the complexity of the neuronal networks in turtle have made it impractical to locate the relevant CPG neurons experimentally.

As an alternative, researchers have, on theoretical grounds, proposed structures that may represent important components or principles involved in the function of the relevant CPGs [5]. Computational methods offer a natural means to investigate these structures' properties and generate predictions about them that may guide future experimental investigations. In this work, we use computational methods to study turtle pocket scratch (pocket) and rostral scratch (rostral) motor pattern generation.

Previous theoretical work on motor pattern generation in turtles ([31, 59]) focused on the generation of caudal scratch and forward swim rhythms from a variety of network architectures, testing their compatibility with several observed experimental characteristics. In contrast, we test whether a specific proposed network architecture [5] is capable of robustly generating both pocket and rostral scratch rhythms via only a change in inputs. Common to both works is the notion of eliciting multiple rhythms from a fixed network. Indeed, both approaches depart from the traditional unit burst generator framework (in which there exist specific excitatory and inhibitory populations dedicated to controlling the activity of motoneurons associated with each joint, [27]). The models in the earlier paper included distinct interneurons projecting to each motoneuron (MN), but these could interact directly in the rhythm generation process; furthermore, inhibition was restricted to interactions shaping the interneuron outputs, rather than impinging on MNs directly [31]. Here, we do not maintain a complete segregation of projection targets and instead show that by considering only hip-related pools of excitatory and inhibitory interneurons, each projecting to both hip and knee MNs, appropriate knee-hip timing relations can be produced.

While the specific network architecture that we consider is motivated by findings from experiments in turtles, our model has a variety of features that are interesting from a mathematical point of view and that may be of use in other modeling work. Wherever possible, we use a general framework and mathematical approach to gain insight into the mechanisms underlying our key results: a single network can (in a nontrivial way) produce two distinct rhythms selected by constant input levels, the timing of activation of a neuron receiving concurrent excitation and inhibition at all times can be controlled by different inputs under different conditions, and a delay in the onset of activity of one neuron relative to another can arise robustly in a model network lacking any explicit inclusion of delay. Our general mathematical approach will allow our findings, while made in a model for turtle motor rhythm generation, to be extensible to other networks with fairly general features.

In Section 2.1, we provide an overview of past experimental results, and synthesize these results into a series of key features our model must produce. An introduction to the network architecture we model, the structural features we impose on it, the fast/slow decomposition we use in analysis, and some of our basic parameter sets is given in Section 2.2. In Section 2.3, we present baseline results showing that a change in input can give distinct output patterns. In Section 2.4, we construct a slow phase plane framework and use it to derive sufficient conditions on inputs for distinct rhythm generation; we also use this framework to identify a key differentiator in inputs that will lead to different rhythms. We reproduce the results of dual-stimulation experiments and use them to provide a negative criterion to rule out different parameter sets for our collaborators in Section 2.5. In Section 2.6, we use our model to make additional predictions and suggestions for experiments our collaborators have interest in performing. In the discussion, we summarize our findings and indicate limitations, with a focus on avenues for future work. A variety of notation is used in this chapter, which we summarize in Table 1. This work has been published in [57] but has been modified for readability.

2.1 EXPERIMENTAL BACKGROUND

Under experimental conditions, intact turtles generate a variety of rhythmic motor patterns corresponding to stimulation of different body regions (including caudal scratch, rostral scratch, pocket scratch, and forward swim; see Figure 1) [4]. All of these patterns feature alternating phases of motoneuron activation that occur repeatedly, while different patterns are distinguished by the relative timing and duration of activity of hip extensor motoneurons, hip flexor motoneurons and knee extensor motoneurons.

Previous theoretical work examined eliciting both caudal scratch and forward swim from the same network [31]. In this chapter, we investigate whether a single network is capable of generating both the pocket and rostral scratching behaviors observed in the turtle hindlimb. Motoneuron behavior identifies each rhythm, shown in Figure 1. Specifically, hip flexor (HF) and hip extensor (HE) motoneuron populations activate in antiphase and do not receive temporally overlapping excitation and inhibition [50, 51, 5]. Hip flexor is activated longer than hip extensor in rostral, and the reverse holds in pocket. Finally, knee extensor (KE) is activated with hip extensor in pocket. Knee extensor is activated with hip flexor with a delay in onset in rostral.

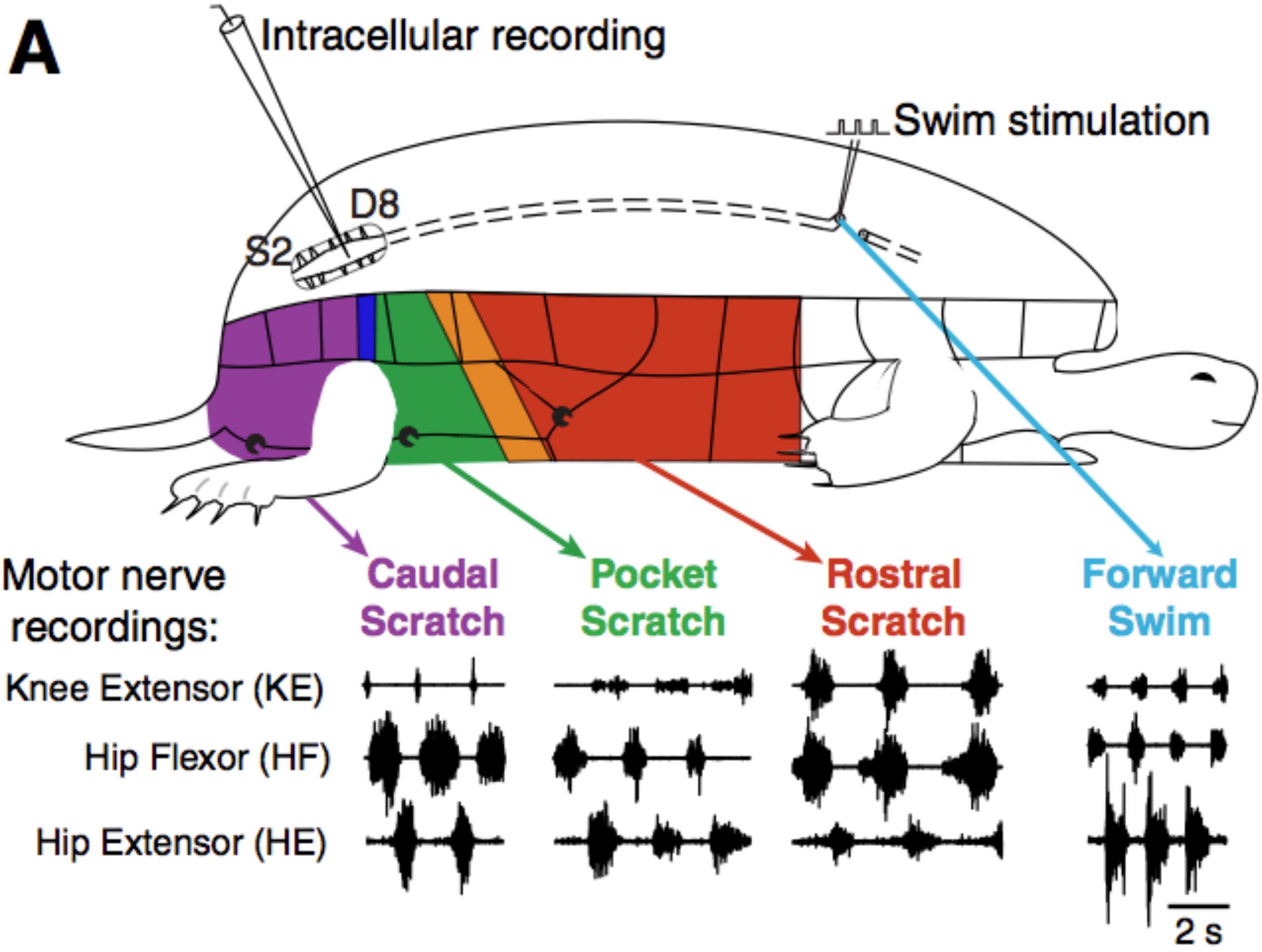

Figure 1: Illustration of how stimulation of different sites, via an electrode for swim or body surface contact for scratch, elicits different patterns of activity in motoneuron recordings from turtle. The scratching rhythms refer to muscle activation in the hindlimb. Figure source: Berkowitz, A.: Physiology and morphology of shared and specialized spinal interneurons for locomotion and scratching. J Neurophysiol. 99(6), 2887–2901 (2008). [4].

Much of the experimental work in turtle has demonstrated that knee extensor MNs receive temporally overlapping excitation and inhibition and that the time courses of the inputs to knee extensor MNs are similar to those of inputs to hip flexor MNs in rostral and to hip extensor MNs in pocket [5, 50, 51, 3]. Berkowitz and Stein argued that an architecture featuring excitatory and inhibitory pools of interneurons for each of hip extensor and hip flexor (with each MN population active in synchrony with its respective excitatory pool), which also project to knee extensor MNs, could be more consistent with experimental findings than other architectures [5]. The idea that different rhythm generators can control knee extensor MN timing in different rhythms also fits in with recent observations from experiments in the mouse hindlimb locomotor network, which suggest that intrinsically rhythmic interneuron modules can be flexibly recruited to drive MN pools [30].

To summarize the experimental features we wish to reproduce:

- HF and HE activate in antiphase and do not receive temporally overlapping excitation and inhibition [50, 51, 5].
- HF is activated longer than HE in rostral (Figure 1, reversed in pocket).
- KE is activated and terminates activity with HE in pocket. KE is activated and terminates with HF, with a delay in onset in rostral.

These features will serve as benchmarks as we evaluate the success or failure of our simulations. In the next section, we will present the architecture we implement, provide a mathematical description of neurons in our model, and we will describe the structural assumptions we are making, the fast/slow decomposition we use in analysis, and the parameter sets we implement.

2.2 NETWORK ARCHITECTURE AND MODEL

A possible motor CPG architecture differing from the traditional UPG view was proposed based on experimental results on turtle scratching rhythms [5] (Figure 2, left). EP is the excitatory motor pool that drives HE, with the P denoting that it is the hip muscle with greater active duration in pocket; IP is the corresponding inhibitory interneuron population for HE. Similarly, ER is the excitatory motor pool that drives HF, with the R denoting that it is the hip muscle with greater active duration in rostral; IR is the corresponding inhibitory interneuron population for HF. Departing from the traditional UPG approach, there are no dedicated excitatory and inhibitory interneuron pools corresponding to knee extensor. Rather, all four of the hip-related motor pools project to knee extensor as well.

As has been well established, however, drawing a plausible wiring diagram for a rhythmic circuit does not allow the immediate inference of actual circuit activity patterns [1]. To explore network dynamics, we implement a simplified version of the proposed architecture, featuring a layer of interneuron pools indexed by labels $i \in \{IP, EP, ER, IR\}$ interacting with each other and feeding forward to a layer of MNs indexed by labels $i \in \{HE, KE, HF\}$ that do not interact. In lieu of an excitatory pool exciting an inhibitory sub-population that in turn inhibits or disinhibits inhibitory pools as originally proposed (e.g. EP excites a sub-population that inhibits IP and disinhibits IR, Figure 2, left), in our model E and I pools are linked, for simplicity, via direct synaptic connections (Figure 2, right). A variety of notation is used throughout this chapter and is detailed in Table 1.

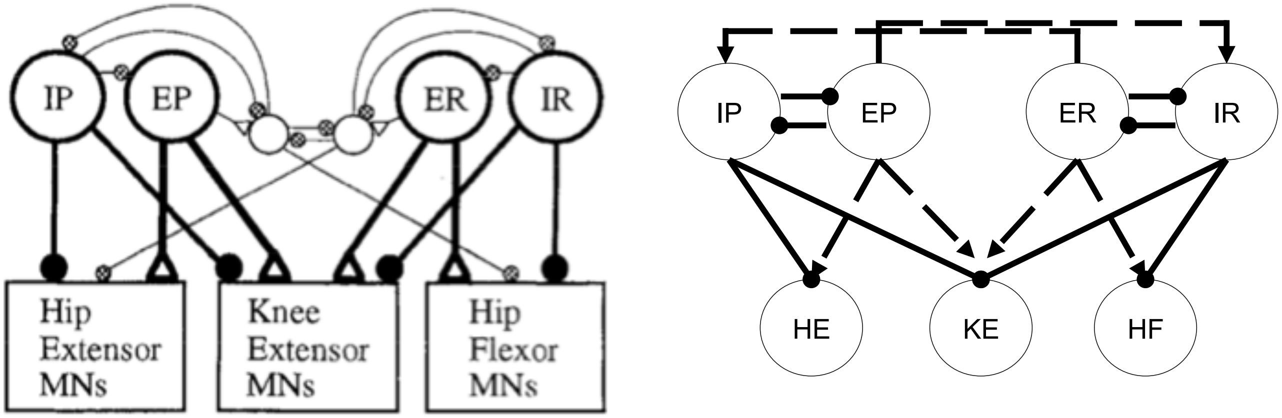

Figure 2: Proposed (left,[5]) and implemented (right) network architectures. Solid circles correspond to inhibitory synaptic connections, open triangles (left) and dashed arrows (right) to excitatory ones. Figure source for proposed architecture: Berkowitz, A., Stein, P.: Activity of descending propriospinal axons in the turtle hindlimb enlargement during two forms of fictive scratching: phase analyses. J Neurosci. 14(8), 5105–5119 (1994).

Table 1: Variables and notation used in Chapter 2

V_i	membrane potential for population i
h_i	deinactivation of persistent sodium current for population i
s_i	slow synaptic gating variable for population i
I_{NaP}	persistent sodium current
I_{syn}	synaptic input from the network
I_{ext}	external synaptic input
$F(V_i, h_i, s_i)$	right hand side of the voltage differential equation
$g_i(V_i, h_i)$	right hands side of the persistent sodium differential equation
$g_{syn}^{i,j}$	synaptic weight of the synapse from population j to population i
i_i^{ext}	weight of external drive to population i
$\mathbf{s}$	vector of all synaptic variables in the network
$V_{i,X}(h, \mathbf{s})$	left ($X = L$), middle ($X = M$) or right ($X = R$) branch of the cubic voltage nullcline for population i
$p_{i,X}(\mathbf{s})$	fixed point located on the $X \in \{L, M, R\}$ branch of the voltage nullcline for population i
$(V_i^{JU}(\mathbf{s}), h_i^{JU}(\mathbf{s}))$	jump up curve, curve in slow phase space from which population i may enter the active phase
$(V_i^{JD}(\mathbf{s}), h_i^{JD}(\mathbf{s}))$	jump down curve, curve in slow phase space from which population i may enter the silent phase
s_{max}	maximum value achieved by synaptic gating variable
$s_{dynamic}$	synaptic gating variable evolving in time for a given portion of the rhythm, while the other synaptic

	gating variable is fixed
$I = \{i_{IP}^{ext}.i_{EP}^{ext}, i_{ER}^{ext}, i_{IR}^{ext}\}$	set of external drives to populations of interneurons
$T_{active}^{j}(I)$	length of time population j is active for a given I
s_{SN}	value of s at which saddle node bifurcation occurs
$s_{ER}^{min}(I)$	minimum value achieved by s_{ER} for a given I
$I_s = [s_{ER}^{min}(I), s_{SN}]$	values of s_{ER} from which KE can enter the active phase
h_{max}	$h_{EP}^{JD}(s_{max}) = h_{ER}^{JD}(s_{max})$, the largest h_{KE} value at which KE can enter the silent phase
$h_{min}(I)$	$h_{ER}^{JD}(s_{ER}^{min}(I))$, the value of h_{KE} on the ER curve of jump down knees corresponding to $s_{ER}^{min}(I)$
$I_h = [h_{min}(I), h_{max}]$	values of h_{KE} at which KE can enter the silent phase
LK_{I_s}	the part of the curve of jump up knees corresponding to $s \in I_s$
$T(I)$	time for s to decay from s_{SN} to $s_{ER}^{min}(I)$
$h(a; b, c)$	h_{KE} value at time a for a trajectory that started at time 0 with initial condition $(h_{KE}, s) = (b, c)$
$h_{ER}^{min}(I)$	h value on the ER jump up curve given by $s_{ER}^{min}(I)$
h_{SN}^{+}	forward flow of (h_{SN}, s_{SN}) for time $T(I)$
h_{SN}^{-}	backward flow of (h_{SN}, s_{SN}) to the line $s = s_{max}$
$h_{s_{min}}^{-}$	backward flow of $(h_{ER}^{JU}(s_{ER}^{min}(I)), s_{ER}^{min}(I))$ to the line $s = s_{max}$
t^{*}	minimal time spent in the silent phase by KE

Based on the experimental recordings shown in Figure 1 and the architecture in Figure 2, the parsimonious assumptions are that HE activates in synchrony with its excitatory interneuron population EP, which activates in antiphase with the inhibitory interneuron population IP, while HF activates in synchrony with its excitatory interneuron population ER, which activates in antiphase with the inhibitory interneuron population IR. The nature of the rhythms (Figure 1) indicates additionally that HE and HF must activate in antiphase for both rhythms, with HF activated longer in rostral and HE activated longer in pocket. It was hypothesized that KE receives inputs that are similar to those received by HF in rostral and similar to those received by HE in pocket [51]. The subsequently proposed architecture in Figure 2, however, suggests that the inputs to KE are proportional to those to both HE and HF, which makes it less clear why KE synchronizes with HF, after some delay, in rostral and with HE in pocket (Figure 1), which is what we seek to explain.

Since we seek to assess the basic rhythm generating capabilities of the proposed architecture, we model each neuronal population in the network as a single cell, leaving issues of heterogeneity for future investigation; we nonetheless refer to each as a "population" in the remainder of the paper (cf. [53]). Inasmuch as the relevant rhythm generating neurons in turtle have not been identified, the specific currents that are central to their rhythmicity are not known. Given this situation, it makes sense to avoid overly specific assumptions about the dynamics of model components. The dynamically simple Wilson-Cowan equations were used in related previous work [31] to model forward swim and caudal scratch rhythms. However, there is a delay in the onset of knee extensor activity relative to hip extensor in caudal scratch that was not modeled in the earlier study. Since the delay of knee extensor onset in rostral scratch is one of the key features that we seek to model, and phase plane considerations suggest that the monotone nullclines of a Wilson-Cowan system cannot give a significant delay, the Wilson-Cowan framework does not appear to be appropriate for our study.

As an alternative, we use a minimal Hodgkin-Huxley type model for each population. We chose an inward, slowly deinactivating persistent sodium current (I_{NaP}) as the primary current controlling oscillations in our model. This current has been used in previous CPG modeling studies [20, 14, 54, 53], has been observed experimentally in neurons in other CPGs [68], and is well suited to supply the voltage plateaus underlying bursts of spikes. Since past computational and mathematical work has established that certain classes of currents endow models with similar properties, this specific current choice is not critical for qualitative aspects of our model's behavior, and our results will apply immediately to networks featuring other inward, slowly deinactivating currents [35, 20]. We omit the details of actual spikes in our model, since the relative durations of active periods, not specific spiking dynamics, are the primary results that we seek to reproduce and since plateau potentials are observed in turtle motoneurons[33, 7]. As a result, we obtain an analytically tractable framework, which would not be possible from incorporation of detailed models for turtle motoneuron dynamics [7, 6].

Given these considerations, our model for each interneuron population takes the form

$$\begin{aligned} C_m\dot{V_i} &= -I_{NaP}(V_i,h_i) - I_L(V_i) - \textstyle\sum_{j\neq i} I_{syn}(V_i,s_j) - I_{ext}(V_i) \\ &\equiv F_i(V_i,h_i,\mathbf{s}) \\ \dot{h_i} &= (h_\infty(V_i) - h_i)\tau_h(V_i) \equiv g_i(V_i,h_i) \\ \dot{s_i} &= \alpha(1-s_i)s_\infty(V_i) - \beta s_i \end{aligned} \tag{2.1}$$

where V_i denotes voltage, h_i the inactivation of the persistent sodium current I_{NaP}, s_i the fraction of the maximal synaptic conductance that is induced by the population's activity, and $\mathbf{s}$ the vector of s variables of all populations in the network (although the evolution of V_i is independent of s_i). In the voltage equation for population i, $I_{NaP}(V_i,h_i) = g_{NaP}m_\infty h(V_i - e_{Na})$, $I_L(V_i) = g_L(V_i - e_L)$ is a leak current, $I_{syn}(V_i,s_j) = g^{ij}_{syn}s_j(V_i - e_{syn})$ for $e_{syn} \in \{e^{exc}_{syn}, e^{inh}_{syn}\}$ denotes synaptic current induced by population j, $I_{ext}(V_i) = (i^{ext}_i)(V_i - e^{exc}_{syn})$ denotes excitatory synaptic current with conductance i^{ext}_i from a source outside the network, m_∞, h_∞ and s_∞ are monotone sigmoidal functions given by $x_\infty(v) = (1+\exp((v-x_{half})/\theta_x))^{-1}, x \in \{m,h,s\}$ with m_∞ and s_∞ increasing and h_∞ decreasing, and $\tau_h(v) = \epsilon\cosh((v-h_{half})/2\theta_h)$ for $0 < \epsilon \ll 1$. All synaptic inputs are defined with $g^{ij}_{syn} > 0$; whether a synaptic input is excitatory or inhibitory is determined by its reversal potential e_{syn}. Default parameter values used in simulations are listed in Table 2; values of i^{ext}_i are varied and are discussed as they arise in our analysis.

Table 2: Model Parameters for Chapter 2

parameter	units
C_m	0.21 pF
g_{NaP}	10 nS
e_{Na}	50 mV
g_L	2.8 nS
e_L	-65 mV
m_{half}	-37 mV
θ_m	-6 mV
h_{half}	-30 mV
θ_h	6 mV
ϵ	0.01 ms^{-1}
s_{half}	-43 mV
θ_s	-0.1 mV
e_{syn}^{inh}	-80 mV
e_{syn}^{exc}	0 mV
α	1
β	0.08

2.2.1 Structural hypotheses

With these parameter values, our model equations satisfy several structural hypotheses. We base our analytical arguments on these hypotheses, so that our results extend beyond our specific choices of model functions and parameter values.

(H1) For each population i, for all relevant synaptic inputs $\mathbf{s}$, the V_i nullcline, $\{(V_i, h_i) : F_i(V_i, h_i, \mathbf{s}) = 0\}$, is cubic in the (V_i, h_i) phase plane. This nullcline includes left, middle, and right branches, denoted respectively by $V = V_{i,L}(h, \mathbf{s})$, $V = V_{i,M}(h, \mathbf{s})$, and $V = V_{i,R}(h, \mathbf{s})$ with $V_{i,L} < V_{i,M} < V_{i,R}$ for each $(h, \mathbf{s})$ for which all three exist. For our choice of model, for fixed $\mathbf{s}$, $V_{i,L}$ and $V_{i,R}$ increase as a function of h and $V_{i,M}$ decreases as a function of h, so this will henceforth be assumed as well, although it is not required for our results to hold. Figure 3 illustrates these structures and those introduced in subsequent hypotheses.

(H2) For each population i, the h_i nullcline, $\{(V_i, h_i) : g_i(V_i, h_i) = 0\}$, is monotone decreasing.

(H3) In the absence of synaptic coupling ($g_{syn} = 0$), each population has a unique fixed point, $p_{i,R}^{FP}(0) = (V_{i,R}^{FP}(0), h_{i,R}^{FP}(0))$, on the right branch of the V_i nullcline for a range of input conductances, i_i^{ext}.

(H4) In the presence of coupling ($g_{syn} > 0$) and with input strength i_i^{ext} fixed within the range we consider, the right fixed point is retained and left $p_{i,L}^{FP}(\mathbf{s}) = (V_{i,L}^{FP}(\mathbf{s}), h_{i,L}^{FP}(\mathbf{s}))$ and middle $p_{i,M}^{FP}(\mathbf{s}) = (V_{i,M}^{FP}(\mathbf{s}), h_{i,M}^{FP}(\mathbf{s}))$ fixed points are gained and lost via saddle-node bifurcations that occur for some nonzero choices of the synaptic input $\mathbf{s}$ (for example, see Figure 4).

These hypotheses restrict the system to have between one and three fixed points for all relevant inputs and coupling strengths. Fixed points on the right branch of the V_i nullcline correspond to tonic spiking behavior (since the model lacks spike generating currents), while fixed points on the left branch of the V_i nullcline correspond to a relatively constant low voltage. Therefore, hypothesis 3 means each population is intrinsically tonically active (Figure 3, right fixed point). In our desired network activity, bursting behavior in a population of neurons consists of regular alternations between states of low voltage near some family of left nullcline branches $V_{i,L}^{FP}(\mathbf{s})$ (silent phase) and states of tonic spiking (i.e., elevated voltage) near some family of right nullcline branches $V_{i,R}^{FP}(\mathbf{s})$ (active phase), linked via abrupt voltage transitions of significant amplitude, corresponding to jumps between branches.

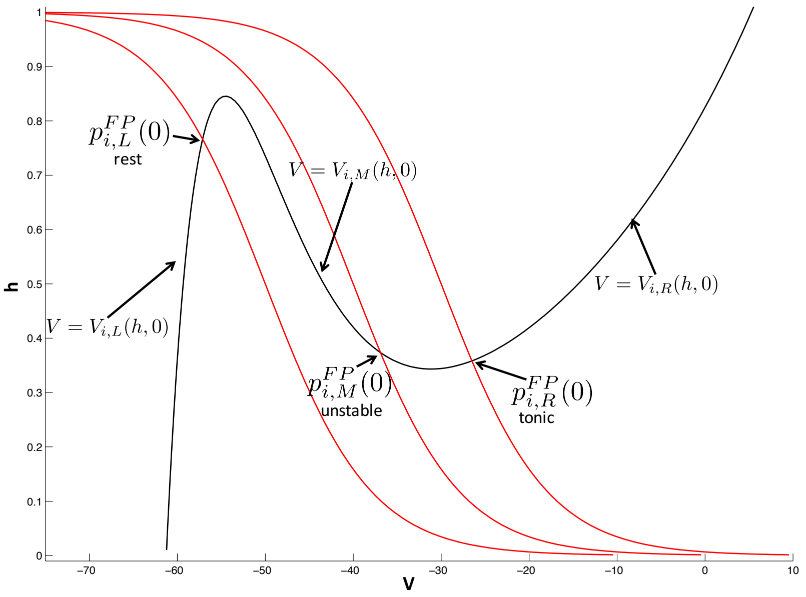

Figure 3: Nullcline configurations for varying values of θ_h (shifting the h-nullcline, red) to illustrate key structures in phase space.

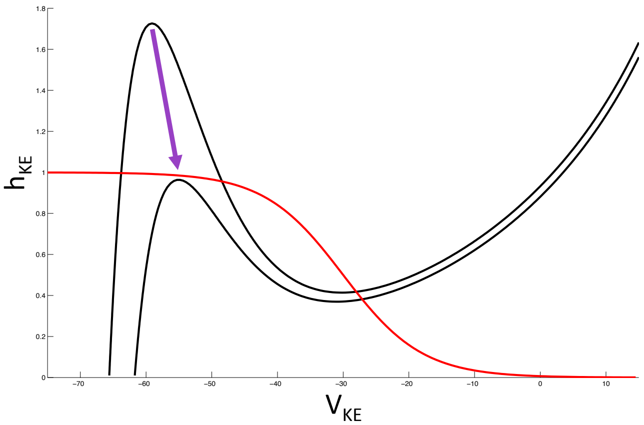

Figure 4: Rostral delay mechanism for KE. Saddle node bifurcation in the (V_{KE}, h_{KE}) phase plane. The red curve is the h_{KE}-nullcline, while the black curves are V_{KE}-nullclines for differing combinations of synaptic input. The change between these two combinations induces a saddle node bifurcation.

A key point is that hypotheses 3 and 4 together imply that transitions from the silent to the active phase must occur by escape. Given a mutually inhibitory pair of populations where one is active and the other is silent, the silent population may become active by reaching the jump up (left) knee of its V nullcline (i.e., left fold of its family of V-nullclines, parameterized by the synaptic strength s controlled by the other population). Doing so allows it to jump to the active phase, inhibiting the other population and, for sufficiently large g_{syn}, relegating the other population to the silent phase. When these conditions are met, the two populations form a half-center oscillator in which switches between phases are controlled by the silent population [69, 56]. This occurs even though the active population still maintains its right fixed point because the network is tuned for transitions by the escape mechanism. Thus, in addition to the surfaces of fixed points for each population, $p_{i,X}^{FP}(\mathbf{s}) = (V_{i,X}^{FP}(\mathbf{s}), h_{i,X}^{FP}(\mathbf{s})), X \in \{L, M, R\}$, of mathematical importance are also the surfaces of jump up and jump down V-nullcline folds, or knees, for each population: $(V_i^{JU}(\mathbf{s}), h_i^{JU}(\mathbf{s}))$ and $(V_i^{JD}(\mathbf{s}), h_i^{JD}(\mathbf{s}))$. For fixed levels of external and synaptic inputs, the jump up (down) knee corresponds to a local maximum (minimum) of the V_i nullcline. A surface of knees is then the surface of these local extrema, parameterized by the values of the synaptic input variables, for a fixed external input strength.

2.2.2 Fast/slow decomposition

Based on our parameter choices (Table 2), for each i, we consider that jumps between branches of a V-nullcline occur instantaneously relative to the rate of I_{NaP} (de)inactivation and relative to the slow decay of s_i (set by the small value of β) in the silent phase. Furthermore, we have performed simulations with a very steep synaptic activation function $s_\infty(v)$, since θ_s is quite small. Thus, for purposes of analysis, we write $\beta = \epsilon\tilde{\beta}$, define $\tau = \epsilon t$, and let prime denote differentiation with respect to τ. We then extract from system (2.1) in the $\epsilon \to 0$ limit a fast subsystem governing jumps between phases:

$$\begin{aligned} C_m\dot{V}_i &= F_i(V_i, h_i, \mathbf{s}), j \neq i \\ \dot{h}_i &= 0 \\ \dot{s}_i &= \alpha(1 - s_i)s_\infty(V_i), \end{aligned} \tag{2.2}$$

a slow subsystem governing evolution within the silent phase:

$$\begin{aligned} h_i' &= g_i(V_{i,L}(h_i, \mathbf{s}), h_i), \\ s_i' &= -\tilde{\beta} s_i, \end{aligned} \tag{2.3}$$

and a slow subsystem governing evolution within the active phase

$$\begin{aligned} h_i' &= g_i(V_{i,R}(h_i, \mathbf{s}), h_i), \\ s_i &= 1. \end{aligned} \tag{2.4}$$

At any time when there is no population making a fast jump, the collection of populations evolves in a high-dimensional slow phase space with governing equations given by making an appropriate choice of either equations (2.3) or equations (2.4) for each population.

Suppose we consider a collection of N interacting populations. Since s_i does not affect V_i, h_i directly, it is useful to project the trajectory to an N-dimensional slow phase space for each population, with dimensions corresponding to that population's h variable along with the s variables for the other $N-1$ populations. The population's jump up and jump down knees, $(V_i^{JU}(\mathbf{s}), h_i^{JU}(\mathbf{s}))$ and$(V_i^{JD}(\mathbf{s}), h_i^{JD}(\mathbf{s}))$, are then given by surfaces in its slow phase space (e.g. [24, 52]).

2.2.3 Parameter sets

We simulated system (2.1) using XPPAUT [23] to find parameter values for which the network (Figure 2, right) would generate a rostral scratch rhythm under one set of constant external input strengths, $\{i_i^{ext}\}_{\mathcal{R}}$, and a pocket scratch rhythm under a different set of constant external input strengths, $\{i_i^{ext}\}_{\mathcal{P}}$ (see Figure 1). We required that synaptic weights, $\{g_{syn}^{ij}\}$, were fixed at the same values for both rhythms, such that our results would represent activation of a fixed network by two different forms of stimulation, presumably representing effects of body surface stimulation in two different regions (Figure 1).

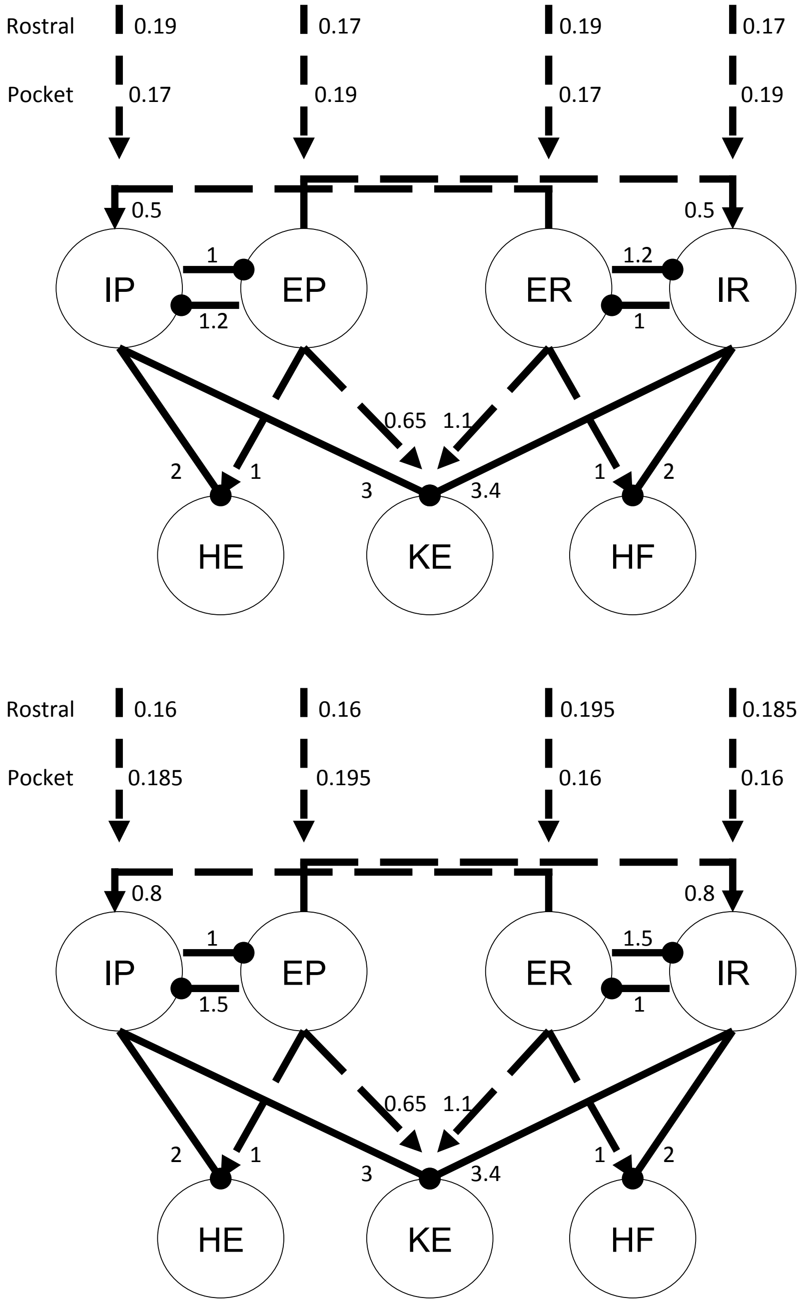

Figure 5: Synaptic weights. Two different sets of synaptic weights g_{syn}^{ij} and external input strengths i_i^{ext} used in our simulations of system (2.1), with units (mS) omitted. Top: "standard" weights; bottom: "strong cross-excitation" weights. Solid lines ending in circles denote inhibitory connections; dashed lines ending in arrows represent excitatory ones. Both sets of weights include certain symmetries but the activity they support is robust to asymmetric perturbations.

Two distinct classes of synaptic weights were implemented in the network, standard (S) and strong cross-excitation (SCE) (Figure 5). The S class is based on the idea that a rostral-inducing stimulus should strongly recruit the excitatory ER pool responsible for driving HF and less strongly recruit the inhibitory IR pool that blocks this action, and similarly for pocket. These input levels can also be interpreted as all four interneuron populations receiving a baseline level of input, with ER, IP receiving additional input in rostral and EP, IR receiving additional input in pocket. The synaptic outputs from the interneuron populations are given in Figure 6.

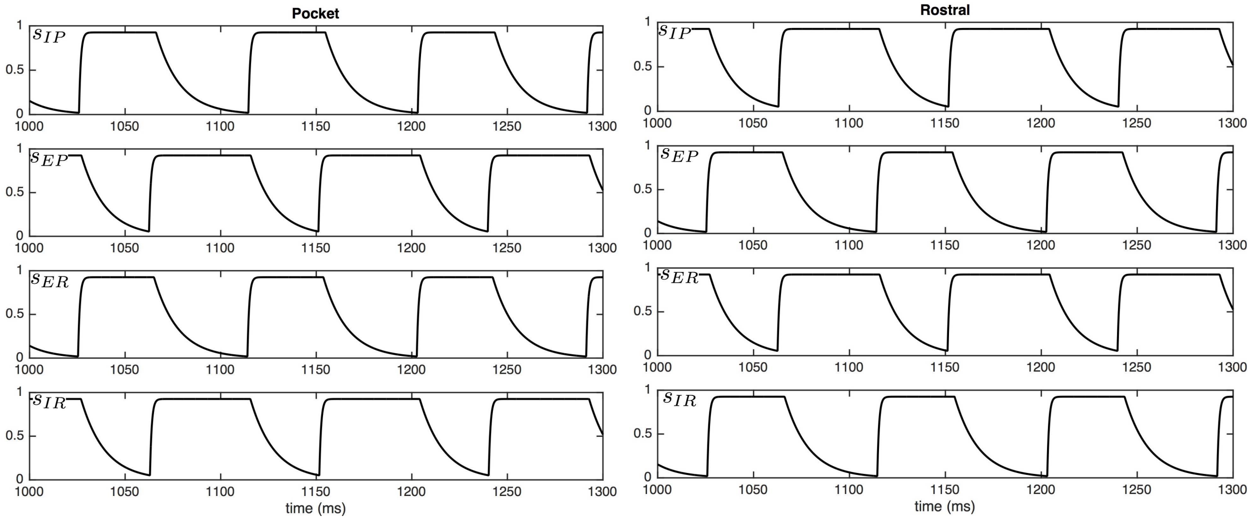

Figure 6: Interneuron synaptic outputs in pocket (left) and rostral (right) in the S parameter set. The plateau of values of $s_i(t)$ near 1 correspond to the active phase of population i. During the silent phase of population i, $s_i(t)$ is decaying.

The SCE class is based on the reasoning that the entire rostral pool, including both ER and IR, should be most strongly stimulated by rostral-inducing stimuli, and similarly for pocket. We call this weight class SCE because a stronger cross-excitation from ER to IP and from EP to IR (0.8 nS versus 0.5 nS) was used to promote synchrony between these pairs of populations in this case. Here, all four interneuron populations can be viewed as receiving a baseline level of input, but with an additional input boost to the "active side". The synaptic outputs from the interneuron populations are given in Figure 7.

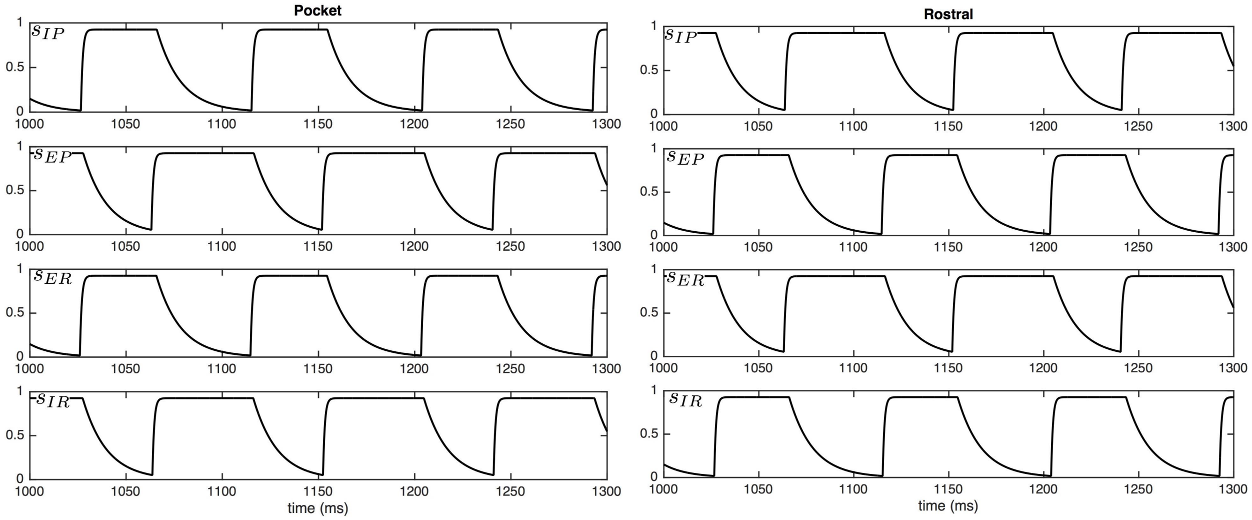

Figure 7: Interneuron synaptic outputs in pocket (left) and rostral (right) in the SCE parameter set. The plateau of values of $s_i(t)$ near 1 correspond to the active phase of population i. During the silent phase of population i, $s_i(t)$ is decaying.

In both cases, the synaptic weights at the interneuron level (not to the MNs) are just a minimal combination that allows oscillations to occur; that is, decreasing any of the weights appreciably without changing others to compensate leads to loss of all oscillations. The baseline input strengths (0.17 nS in S and 0.16 nS in SCE) were chosen such that no oscillations are elicited when no interneuron populations receive additional drive. The S and SCE weights are similar in the sense that they result in qualitatively similar interneuron dynamics and output from the interneurons to the MNs. This output is largely constrained by the required behavior of HF and HE:

- HF and HE activate in antiphase and do not receive temporally overlapping excitation and inhibition [50, 51, 5] meaning that IP must be in antiphase with EP and IR in antiphase with ER (Figure 2 right panel).
- In light of these antiphase relations, it is natural for EP, IR to activate in synchrony and ER, IP to activate in synchrony.
- HF is activated longer than HE in rostral (Figure 1, Figure 2 right panel, Figure 5), hence ER must receive more input than EP in rostral (reversed in pocket).

Any synaptic weights selected must satisfy these constraints. Furthermore, as will be seen in the next section, a certain general relationship among the synaptic weights to KE must be satisfied to allow both rhythms to be elicited from the network.

In this section, we presented the architecture implemented, a mathematical description of neurons in our model, and we described the structural assumptions, the fast/slow decomposition, and the parameter sets we use. We also introduced definitions of key quantities that arise in our analysis. In the next section, we will present baseline simulations that show our model is capable of producing both the pocket and the rostral scratch rhythms via changing inputs.

2.3 BASELINE SIMULATION RESULTS

With the S and SCE weights, the network can generate both rostral and pocket rhythms, selected by the external input strengths $\{i_i^{ext}\}$ as shown in Figure 5; see Figure 8 for an example simulation with the S class. Thus, we have confirmed the conjecture that the architecture illustrated in Figure 2 is capable of such multi-functionality, suggesting its viability as a building block of circuits generating multiple output rhythms from a single set of MNs and muscles. Naturally, for both the S and SCE weights, there is a range of each input parameter $\{i_i^{ext}\}$ over which each rhythm persists. As mentioned previously, the reason that both architectures work is because they produce qualitatively similar interneuron activity patterns and corresponding outputs from the interneurons to the MNs; note that the connections from the interneurons to the MNs are weighted the same across both weight classes. The mathematical analysis done in the next section shows that sufficient changes in these interneuron-to-MN weights would cause the network to lose the desired behavior.

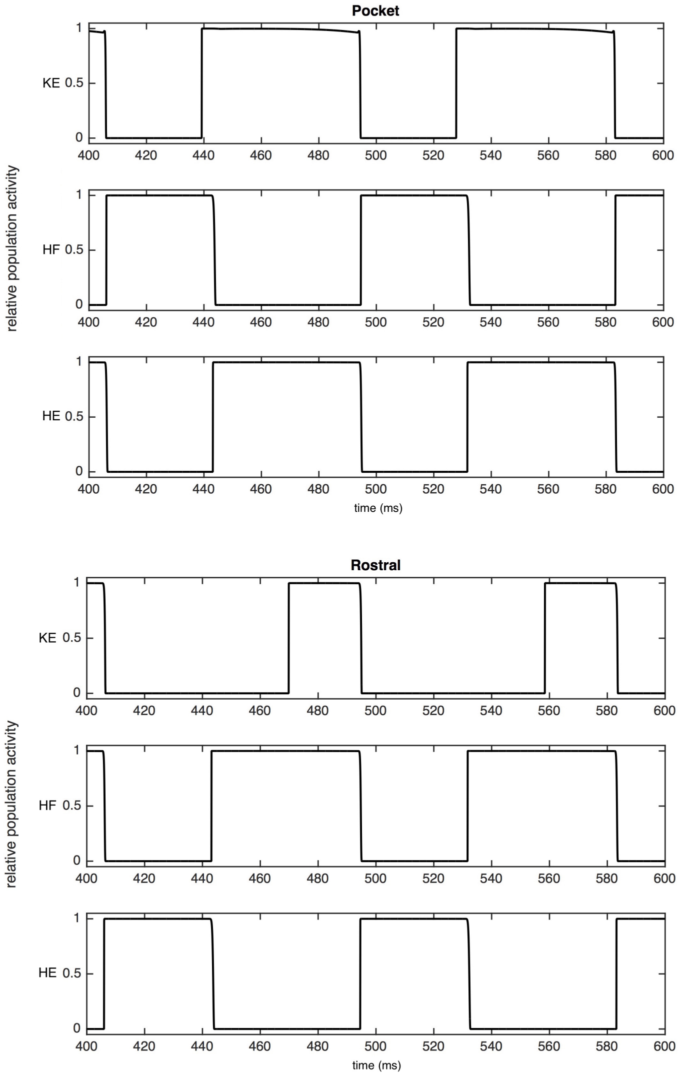

Figure 8: Basic simulation results. Example voltage traces for MN populations resulting from simulation of system (2.1) with the S weights. Note that the relative timing and durations of activity in the simulation match the recordings in Figure 1. The SCE weights produce the desired relative timing and durations as well (not shown).

In this section, we presented baseline simulations that show our model is capable of producing both the pocket and the rostral scratch rhythms via changing inputs. In the next section, we will describe the slow phase plane framework we developed for this system, and then we will use this framework to derive and illustrate the sufficient conditions on inputs in both pocket and rostral.

2.4 SUFFICIENT CONDITIONS FOR RHYTHMS

Because hip extensor and hip flexor each only receive antiphase excitation and inhibition and maintain the same antiphase relationship with each other across both rhythms, it seems reasonable to choose comparable synaptic weights from the interneuron populations to HE and HF. We henceforth assume that these weights and the weights within the interneuron network are fixed such that this antiphase behavior, with appropriate relative phase durations, occurs. Because KE receives temporally overlapping excitation and inhibition, synchronizes with a different hip component in each rhythm, and exhibits a delay in onset relative to its hip partner in rostral and not pocket, the synaptic weights to KE are much more constrained. We will consider dynamics in certain slow phase spaces to derive conditions on these weights that yield multi-functionality of the networks shown in Figure 5, which generalize to any model with a qualitatively similar structure.

2.4.1 Reduction of slow phase space dimension

To focus on KE, we need consider only a subset of the slow variables in the model. KE receives four synaptic inputs with conductance variables $\{s_{EP}, s_{ER}, s_{IP}, s_{IR}\}$, which activate on the fast time scale (equation (2.2)) and decay on the slow time scale (equation (2.3)). Additionally, the inactivation of persistent sodium for KE, h_{KE}, evolves on the same slow time scale. Therefore, there is a five-dimensional slow phase space for KE. Analyzing dynamics in this full, five-dimensional space is impractical.

To reduce dimension further, we identify the interneuron pairs that activate together, (EP, IR) and (ER, IP), to form a single half-center oscillator and we consider a reduced model to describe KE activity, illustrated in Figure 9. With this reduction, using $e^{exc}_{syn} = 0$, $s_{ER} = s_{IP}$, and $s_{EP} = s_{IR}$, the synaptic input for knee extensor becomes

$$I^{KE}_{syn} = s_{ER}[(g_{IP} + g_{ER})V_{KE} - g_{IP}e^{inh}_{syn}] + s_{EP}[(g_{IR} + g_{EP})V_{KE} - g_{IR}e^{inh}_{syn}].$$

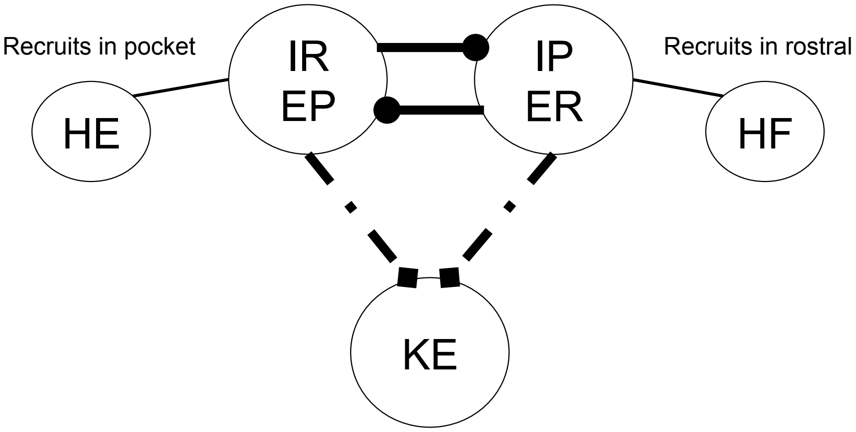

Figure 9: Reduced knee extensor module. Reduced module controlling knee extensor activity. Two interneuron units form a half-center oscillator, linked by mutual inhibition (thick solid lines). Each unit recruits a corresponding hip MN (thin solid lines) and supplies a hybrid excitatory and inhibitory input to KE (dot dashed lines with squares), with a single corresponding synaptic conductance variable.

This step reduces our phase space from five dimensions to three, with variables (h_{KE}, s_{EP}, s_{ER}). The projection of the periodic pocket trajectory of the reduced model to (h_{KE}, s_{EP}, s_{ER}) space is shown in the top left of Figure 10, along with several curves that are important for understanding KE dynamics. These plots are critical to our analysis. When ER is active, $s_{ER} \approx s_{max}$, so the corresponding part of the trajectory, color coded red, lies approximately on the $\{s_{ER} = s_{max}\}$ plane within phase space, which is the back right face of the cube shown. Similarly, the epoch with EP active has $s_{EP} \approx s_{max}$ and yields a trajectory, color coded black, near the back left face of the cube. As an alternative to considering a three-dimensional phase space, however, it is convenient to switch between a pair of two-dimensional slow phase planes, corresponding to the back two faces in the top left of Figure 10, as EP and ER alternate between periods of silence and activity. These are shown in the top right of Figure 10. For example, while EP is active, s_{ER} evolves and the projection of the trajectory to the (h_{KE}, s_{ER}) plane is shown as the thick black curve. Of course, even after EP switches from active to silent, the projection of the trajectory to the (h_{KE}, s_{ER}) plane still exists; the projected trajectory segment after the switch is shown as the thin black curve. Using similar considerations for the projection to (h_{KE}, s_{EP}), we in fact plot two copies of the full trajectory, each in its own two-dimensional phase plane, one with the trajectory shown thick while EP is active and thin while ER is active, and the other the opposite. The switch from EP active to ER active occurs abruptly when s_{EP} begins its slow decay from s_{max} and s_{ER} increases very rapidly (instantly in the singular limit) to s_{max}, and we switch each curve from thick to thin when $s_{EP} = s_{ER}$ occurs.

Finally, since the values over which s_{ER} and s_{EP} vary over each period are similar, both slow phase planes can be compressed to a single plot. Again, when this plot is displayed in the bottom part of Figure 10, we show two copies of the trajectory. For the black (red) copy, $s_{dynamic}$ should be interpreted as s_{ER} (s_{EP}), with thick and thin parts as in the separate two-dimensional plots (thick black when EP is active such that s_{ER} decays gradually, thick red when ER is active such that s_{EP} decays gradually).

For fixed input levels (s_{EP}, s_{ER}), the V_{KE}-nullcline has one or more fixed points, a jump up knee, and a jump down knee. These become two-dimensional surfaces under variation of both inputs, while fixing one input at s_{max} selects a one-dimensional curve. In Figure 10, the curves of fixed points for $s_{EP} = s_{max}$ are shown in green and for $s_{ER} = s_{max}$ in magenta; both show up in the bottom plot, but it is important to keep in mind that each is only meaningful when $s_{dynamic}$ has the correct interpretation. Similarly, the curves of knees are shown in dark blue and cyan. There are two cyan curves, with smaller h_{KE} values for jump down knees than for jump up. There is only one dark blue curve because the curve of jump up knees is outside of the relevant range of (h_{KE}, s) values when EP is active.

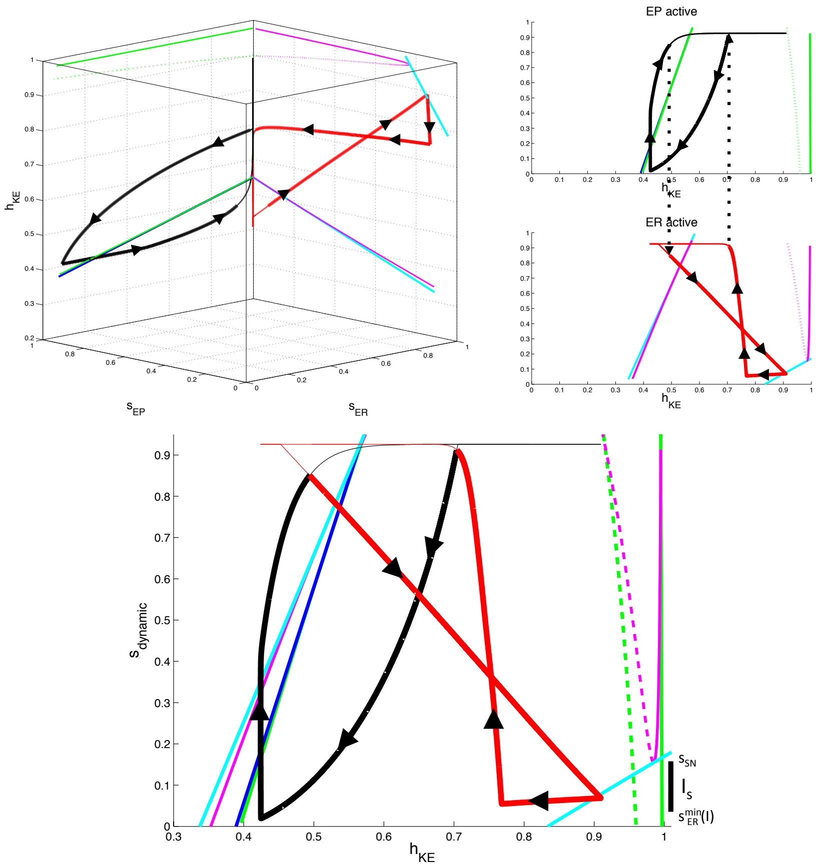

Figure 10: Reduction of knee extensor slow phase space dimension. Phase space views for the KE dynamics in the reduced module shown in Figure 9 during the pocket rhythm. Top left: full three-dimensional slow phase space. Top right: projections onto the two two-dimensional planes where the trajectory lies. Bottom: single, combined two-dimensional representation. In all plots, black and red curves are projections of parts or all of the trajectory of a periodic pocket scratch solution, with bold black and thin red denoting times when EP is active and bold red and thin black times when ER is active. Green curves denote the fixed point curves $p^{FP}_{KE,R}(\mathbf{s})$ (stable, solid), $p^{FP}_{KE,M}(\mathbf{s})$ (unstable, dashed), and $p^{FP}_{KE,L}(\mathbf{s})$ (stable, solid) (in order of increasing h_{KE}) while EP is active. Magenta curves denote the analogous curves of fixed points while ER is active. The dark blue curve is the curve of jump down knees while EP is active; cyan curves are jump down knees and jump up knees (larger h_{KE} values) while ER is active. Finally, dashed black curves in the top right indicate points on the two projections that correspond to the same times, when the switches between the EP active phase and the ER active phase occur.

2.4.2 Scratch trajectories and weights of synapses onto KE

To generate pocket and rostral scratch rhythms in our model, we had to select values for synaptic connections in the model network, which remain the same for both rhythms, and strengths of external inputs to the network, which differ between the rhythms. As mentioned previously, fixing the weights of synapses to the HE and HF MNs is not particularly interesting, since the desired antiphase activation patterns for each rhythm are set at the interneuron level in the full or reduced model. For convenience, we simply choose $g_{syn}^{HE,EP} = g_{syn}^{HF,ER}$ and $g_{syn}^{HE,IP} = g_{syn}^{HF,IR}$.

The weights of synapses onto KE are more interesting. To understand how these are constrained, we can focus on the reduced model, which maintains four distinct synaptic weights from the interneurons onto KE. With the convenient viewpoint that we have established, it is now helpful to consider the details of the trajectories for pocket scratch (Figure 10) and rostral scratch (shown in Figure 11 in a two-dimensional view analogous to the bottom panel of Figure 10) for our baseline parameter choices.

Recall that in the pocket rhythm, KE activates with HE, here represented by the activation of EP. When EP becomes active and the thick black part of the trajectory starts, h_{KE} decreases, corresponding to the trajectory being in the active phase for KE, near a right branch of the V_{KE}-nullcline. The trajectory cannot cross the curve of jump down knees (dark blue) with $s_{dynamic}$ decreasing, because it is blocked by the green fixed point curve (which almost coincides with the dark blue one in Figures 10, 11). The switch of $s_{dynamic}$ from decreasing to increasing corresponds to the activation of ER (and hence HF). The rise in $s_{dynamic}$ pulls the trajectory across the curve of jump down knees of the V_{KE}-nullcline (dark blue), terminating the active phase of KE. We then switch our view to the thick red trajectory, along which h_{KE} increases (and $s_{dynamic} = s_{EP}$ decreases), corresponding to the trajectory being in the silent phase for KE, near a left branch of the V_{KE}-nullcline. The trajectory actually reaches the curve of jump up knees (cyan), and hence KE activates before the activation of EP and HE cause $s_{dynamic} = s_{EP}$ to increase. But shortly after this switch, EP itself activates, yielding a rise in $s_{dynamic}$, and we switch back to the thick black trajectory, where we started. In fact, experiments reveal a natural variability in pocket scratch patterns. There are many experimental examples of pocket rhythms in which knee extensor becomes active just before hip extensor, at the final moments of hip flexor activity, and indeed a mean pocket rhythm computed from experimentation has this property [22]. Hence, this result provides validation that the solution that we have obtained provides a reasonable reduced representation of a pocket rhythm.

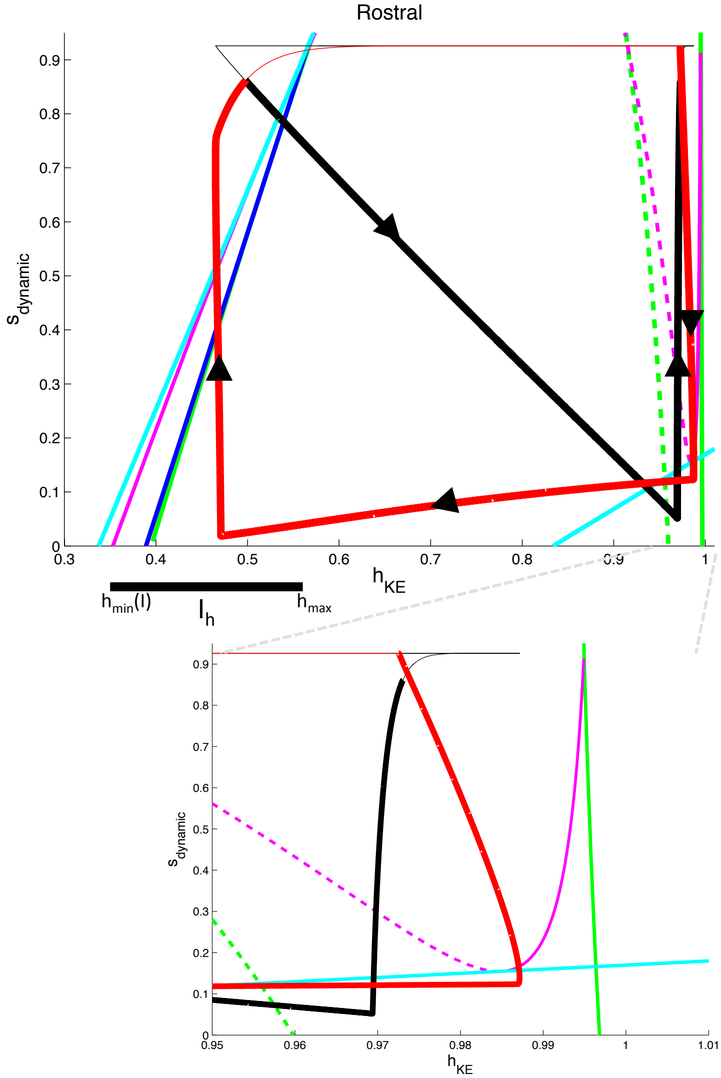

Figure 11: Rostral slow phase plane. Trajectory for KE for rostral scratch projected to a single slow phase plane. Coloring of curves is identical to Figure 10. Bottom: Zoomed view near the saddle-node bifurcation where the fold in the magenta fixed point curve intersects the cyan jump up knee curve for ER/HF active.

In the rostral rhythm, KE activation follows that of HF, here represented by the activation of ER, with a delay. When ER becomes active, and the thick red part of the trajectory starts, KE is still in the silent phase, with a fixed point on the left branch of the V_{KE}-nullcline (solid magenta line at the far right of Figure 11, see especially Figure 11 bottom.). As $s_{dynamic}$ decreases, the trajectory approaches the corresponding branch of fixed points, and KE cannot activate until this branch undergoes a saddle node bifurcation (meeting the dashed fixed point branch in the figure) at the curve of jump up knees of the V_{KE}-nullcline (lower right cyan curve; also see Figure 4). At the bifurcation, KE activates and h_{KE} starts to decay, with the trajectory heading toward the magenta curve of fixed points in the left part of the Figure. When the activity of ER terminates, $s_{dynamic}$ increases, which pulls the trajectory through the curve of jump down knees (cyan) and hence switches KE to the silent phase. With EP now activated (thick black part of the trajectory) and KE silent, h_{KE} increases, but there is no curve of jump up knees available to reach over the relevant range of $(h_{KE}, s_{dynamic})$ (note the absence of a dark blue curve in the lower right of Figure 11, analogous to its absence in Figure 10). Thus KE remains silent until the active phase of EP ends, $s_{dynamic}$ rises, and ER activates at the transition from the thick black to the thick red part of the trajectory, where we started.

From our investigations, it appears that obtaining both pocket and rostral scratch rhythms with the same set of synaptic weights through the dynamic mechanisms we have described requires certain phase plane features and timing relations, which arise in the trajectory descriptions we have provided. Classifying these in terms of particular phases of rhythms, the requirements on the trajectory projected to KE space are as follows:

(i) **pocket, EP active**: trajectory must not reach the curve of jump down knees as $s_{dynamic}$ decreases yet must cross it as $s_{dynamic}$ rises.

(ii) **pocket, ER active**: trajectory must reach the curve of jump up knees as $s_{dynamic}$ decreases, but only sufficiently late in the phase.

(iii) **rostral, ER active**: trajectory must follow a curve of fixed points to a saddle node bifurcation at the curve of jump up knees, must subsequently not reach the curve of jump down knees as $s_{dynamic}$ decreases, and must cross the jump down knees as $s_{dynamic}$ rises.

(iv) **rostral, EP active**: trajectory must not reach the curve of jump up knees as $s_{dynamic}$ decreases.

The first part of requirement (iii) is critical for imposing a delay between ER activation and KE activation. Requirement (iv) goes together with (iii); certainly no delay would be possible if the trajectory reached a curve for the activation of KE even before ER activated at all! To achieve requirements (iii) and (iv), we find that it is necessary but not sufficient for $g_{syn}^{KE,EP}, g_{syn}^{KE,IP}, g_{syn}^{KE,ER}, g_{syn}^{KE,IR}$ to be such that that the ER/IP active pair has an overall more excitatory effect on KE than the EP/IR active pair. Once these requirements are imposed, we find that KE also activates while ER is still active in the pocket rhythm; requirement (ii) constrains weights so that this happens as late as possible, providing a realistic pocket rhythm. Finally, both requirements (i) and (iii) are partially trivial, since the trajectory is blocked from reaching jump down knees by the location of fixed point curves. Nonetheless, they do constrain weights to ensure that h_{KE} decays sufficiently during each active phase such that subsequent rises in $s_{dynamic}$ can pull the trajectory across the curves of jump down knees, transitioning KE to the silent phase along with its interneuron partner, as desired.

2.4.3 Conditions for rhythm selection and slow phase plane analysis/contraction arguments

With our synaptic weights onto KE and slow phase plane structure fixed to satisfy the requirements described in the previous subsections, for each rhythm, we now derive certain conditions on the set of inputs $I = \{i_{IP}^{ext}, i_{EP}^{ext}, i_{ER}^{ext}, i_{IR}^{ext}\}$, which ensure that that rhythm will be selected. Some of these conditions are necessary, while together the collection is sufficient, although we cannot rule out that there may be different necessary and sufficient conditions elsewhere in parameter space. At a minimum, it is always necessary that the inputs actually elicit oscillations, both at the interneuron and the motoneuron levels. For convenience in what follows, define $T_{active}^{j}(I)$ as the length of time for which population j is active for a given set of input parameters I as above.

Recall that we have defined a slow phase plane structure in which activation occurs by gaining access to the curve of jump up knees with ER active (as discussed in the previous subsection). For simplicity, we henceforth refer to $s_{dynamic}$ as s. We define the interval $I_s = [s_{ER}^{min}(I), s_{SN}]$. s_{SN} is defined as the value of s at which the saddle-node bifurcation of fast subsystem critical points occurs with ER active (Figures 10,11), and $s_{ER}^{min}(I)$ is simply the minimum value to which s_{ER} decays. The dependence of s_{ER}^{min} on input arises because the set I determines how long ER is active and hence how far s_{ER} decays from s_{max}. The interval I_s is illustrated for a particular input set I in Figure 10.

We note that in the singular limit, s jumps to s_{max} at the instant (with respect to the slow time scale) of the switch between EP active and ER active. (In our simulations, such as Figures 10 and 11, we are away from the singular limit and hence the switch occurs at some $s^* < s_{max}$. The value of s^* can be easily approximated as $s^* \approx s_{max}e^{-\beta t}$ where, using the differential equation for s in (2.1), t satisfies $s_{max}e^{-\beta t} = (s^{min}(I) - s_{max})e^{-(\alpha+\beta)t} + s_{max}$ given the minimal value of $s_{dynamic}$ is $s^{min}(I)$. This equality illustrates how $t \to 0$ and hence $s^* \to s_{max}$ as $\alpha \to \infty$, corresponding to a complete separation of time scales.) We assume that $h_{EP}^{JD}(s_{max}) = h_{ER}^{JD}(s_{max})$ and denote this h-value by h_{JD}, since we observe this convergence of right knee curves numerically. We define a second interval $I_h = [h_{min}(I), h_{JD}]$, where $h_{min}(I)$ is the value of h_{KE} along the ER curve of jump down knees at $s = s_{ER}^{min}(I)$. This interval specifies the full set of h_{KE} values from which a jump down will yield a crossing of the curve of knees. The interval I_h is illustrated for a particular input set I in Figure 11.

2.4.4 Pocket

Recall the form of the pocket rhythm, illustrated in Figure 10 and Figure 12. Since HE is active longer than HF in this rhythm, we take $i_{ER}^{ext} < i_{EP}^{ext}$, which leads to $T_{active}^{ER}(I) < T_{active}^{EP}(I)$. In a successful pocket rhythm, KE activation can occur at any value of $s_{dynamic} = s_{ER} \in I_s$. The closer to $s_{ER}^{min}(I)$ that activation occurs, the less the overlap of KE and HF activations. With the above constraints and definitions, the pocket rhythm will exist for any set of inputs for which I_s is mapped to $int(I_s)$ under the slow flow pieced together by appropriate selection of (2.3) and (2.4). By continuity, it is sufficient for the existence of a stable pocket rhythm to find conditions on I under which the endpoints s_{SN} and $s_{ER}^{min}(I)$ are mapped into the interior of I_s. We use slow phase plane arguments to do so.

Figure 12: Pocket rhythm. Pocket rhythm: duration and timing of MN activations in simulations (left) and experimental recordings from MNs (right). Recall that HF activates with ER and HE with EP.

Fix input set I. Note that there is an ordering of trajectories starting from the relevant part of the cyan curve of jump up knees corresponding to ER active, given by $LK_{I_s} := \{(h_{KE}, s) : s \in I_s, h_{KE} = h_{ER}^{JU}(s)\}$. That is, suppose $(h_1, s_1), (h_2, s_2) \in LK_{I_s}$ with $h_1 > h_2$ and hence $s_1 > s_2$. Flow (h_1, s_1) forward under (2.3), obtaining a trajectory $(h_1(t), s_1(t))$, until $s_1(t) = s_2$. Similarly, denote the forward flow from (h_2, s_2) as $(h_2(t), s_2(t))$. If $h_1(t) > h_2$ $(h_1(t) < h_2)$, then $h_1(t+\tau) > h_2(\tau)$ $(h_1(t+\tau) < h_2(\tau))$ for all τ until $s_1(t+\tau) = s_2(\tau) = s_{ER}^{min}(I)$ and the ER active phase ends. Moreover, by continuity, all points on LK_{I_s} are ordered in this sense. Thus, the trajectory from LK_{I_s} that attains the minimal h value when $s = s_{ER}^{min}(I)$ is either the one starting from $s = s_{SN}$ (corresponding to $<$ in the statements above) or that from $s = s_{ER}^{min}(I)$ (corresponding to $>$). It turns out that the more interesting case, for which our argument yields one additional sufficient condition, occurs when the minimal h corresponds to the initial condition $s = s_{SN}$, with the initial value of h given by $h_{SN} := h_{ER}^{JU}(s_{SN})$, so without loss of generality we henceforth assume that this orientation holds (Figure 13).

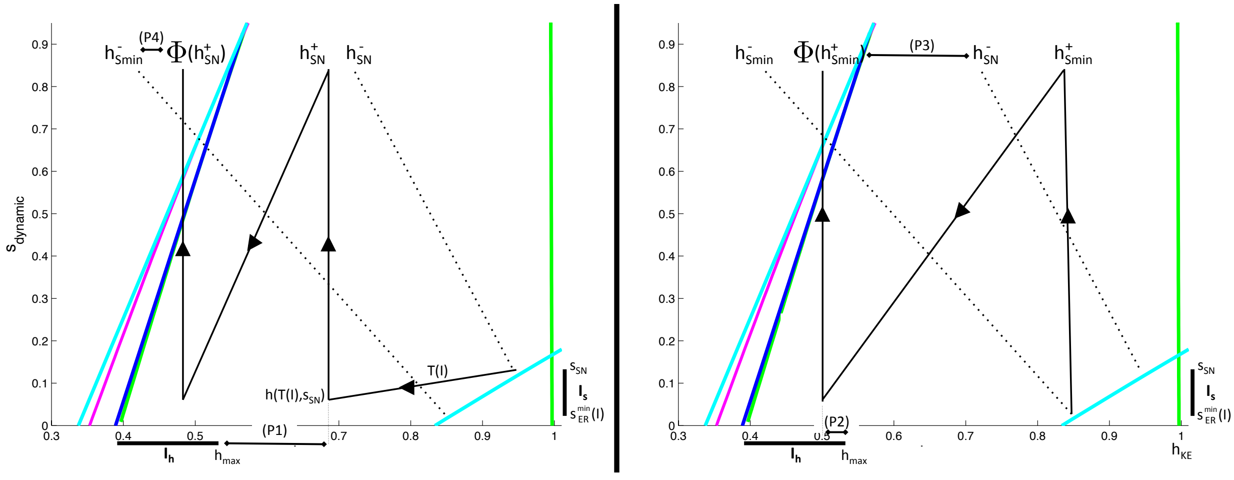

Figure 13: Contraction argument for pocket rhythm. Useful trajectories for deriving sufficient conditions for a stable pocket rhythm. Solid black lines are flows forward from a known point. Dotted black lines represent backward flows. Left: The conditions that arise when a flow is initiated from s_{SN}. Right: The conditions that arise when a flow is initiated from $s^{min}_{ER}(I)$.

Now, let $T(I) = (1/\beta)\ln(s_{SN}/s^{min}_{ER}(I))$ denote the time for s to decay from s_{SN} to $s^{min}_{ER}(I)$. Suppose we choose an initial condition such that KE activation occurs at $s = s_{SN}$ during the ER active phase. We introduce the notation $h(a; b, c)$ to denote the h_{KE} value at time a for a trajectory that started at time 0 with initial condition $(h_{KE}, s) = (b, c)$. The first sufficient condition that we include is that the resulting KE trajectory does not cross a curve of jump down knees when EP takes over from ER:

$$(P1) \quad h^+_{SN} := h(T(I); h_{SN}, s_{SN}) > h_{max},$$

Condition $(P1)$ ensures that the KE active phase overlaps with the active phase of EP and hence HE, as desired; in other words, $T^{KE}_{active}(I) > T(I)$ (Figure 13, left).

Next, we impose a condition to ensure that KE activation ends when EP activation does. This condition forces the KE trajectory with largest h value to lie in I_h at the end of the EP active phase. This trajectory has initial condition $(h^{min}_{ER}(I), s_{max})$ at the start of the

EP active phase, where $h_{ER}^{min}(I) := h_{ER}^{JU}(s_{ER}^{min}(I))$, and evolves under (2.3) with EP active for time $T_{active}^{EP}(I)$ (to $\{s = s_{EP}^{min}(I)\}$). The condition (Figure 13, right) is:

$$(P2) \quad h(T_{active}^{EP}(I); h_{ER}^{min}(I), s_{max}) < h_{max}.$$

Next, we obtain two conditions that are sufficient to ensure that the flow of LK_{I_s} yields trajectories that return to $int(LK_{I_s})$ and that do so while ER is active. To state these conditions, we need to make use of the backwards flow of the endpoints (h_{SN}, s_{SN}) and $(h_{ER}^{JU}(s_{ER}^{min}(I)), s_{ER}^{min}(I))$ back to the line $\{s = s_{max}\}$ under system (2.3) with ER active. Denote the h-coordinates of these intersections by h_{SN}^{-} and $h_{s_{min}}^{-}$, respectively, with $h_{s_{min}}^{-} < h_{SN}^{-}$ by continuity. Recall that the forward trajectory from the endpoint (h_{SN}, s_{SN}) has $h = h_{SN}^{+} := h(T(I); h_{SN}, s_{SN})$ when EP becomes active (see Condition $(P1)$ and Figure 13, left). With these definitions, the final sufficient conditions, which guarantee that the next KE activation occurs from $int(LK_{I_s})$, read

$$(P3) \quad h(T_{active}^{EP}(I); h_{ER}^{min}(I), s_{max}) < h_{SN}^{-},$$

$$(P4) \quad h(T_{active}^{EP}(I); h_{SN}^{+}, s_{max}) > h_{s_{min}}^{-}.$$

$(P1)-(P4)$ are conditions on relative orderings of points in the slow phase space that may result under certain choices of I. To appreciate that when I is chosen to satisfy Conditions $(P1)-(P4)$, together with the earlier condition that $T_{active}^{ER}(I) < T_{active}^{EP}(I)$, it follows that LK_{I_s} is mapped into its own interior under the flow and there exists a stable periodic pocket rhythm, note that the time of evolution from $s = s_{max}$ down to $s = s_{ER}^{min}(I)$ under (2.3) with EP active is exactly time $T_{active}^{EP}(I)$. Conditions $(P3)-(P4)$ ensure that all trajectories emanating from LK_{I_s} end up with $h \in (h_{min}^{-}, h_{SN}^{-})$ when ER first activates. From the time of ER activation, these trajectories all evolve under (2.3) from $s = s_{max}$, and Conditions $(P3)-(P4)$ imply that they reach $int(LK_{I_s})$. In particular, they arrive with $s > s_{ER}^{min}(I)$ and hence they do so after times that are less than $T_{active}^{ER}(I)$, before the end of the ER active phase, as desired.

In summary, we conclude that for a choice of synaptic weights such that our earlier assumptions on the structure of phase space are satisfied, for any choice of I such that $(P1)-(P4)$ hold, there exists an open set of initial conditions supporting a stable, periodic pocket rhythm. Choices of weights that shrink s_{SN} toward $s_{ER}^{min}(I)$, narrowing I_s, yield less overlap between the phases when KE and HF are active at the end of the ER active phase, and hence more experimentally realistic solutions. This change can be achieved, for example, by weakening the excitation from ER to KE relative to the inhibition from IP to KE; however, making this excitation too weak will prevent KE activation entirely and destroy the rhythm.

2.4.5 Rostral

Next, recall the form of the rostral rhythm, illustrated in Figure 11. Since HF is active longer than HE in this rhythm, we take $i_{EP}^{ext} < i_{ER}^{ext}$, which leads to $T_{active}^{EP}(I) < T_{active}^{ER}(I)$. In the rostral rhythms that we seek, we assume that KE activation occurs with $s_{dynamic} = s_{SN}$ with ER (and thus HF) active, in order to achieve the delay with respect to HF activation in a robust way, keeping the same synaptic weights as in the pocket case. We also require that KE activation ends at the same time as ER activation. We now use slow phase plane arguments to derive sufficient conditions for the existence of a stable rostral rhythm that meets these constraints.

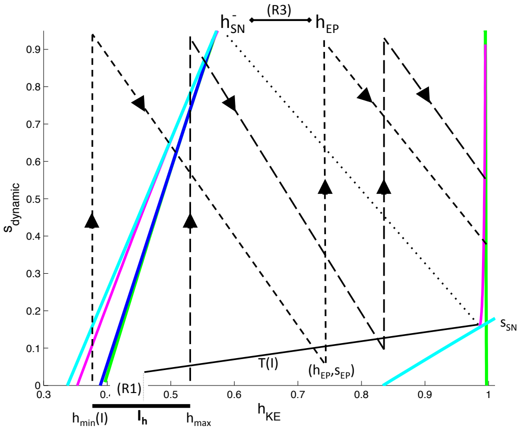

Figure 14: Contraction argument for rostral rhythm. Useful trajectories for deriving sufficient conditions for a stable rostral rhythm. The solid black line denotes the flow forward from (h_{SN}, s_{SN}). Dashed black lines indicate flows forward from two points (h_{max}, s_{SN}) and $(h_{min}(I), s_{SN})$. The dotted black line represents a backward flow.

The trajectory for the desired rhythm should reach the curve of jump up knees with $s = s_{SN}$ and ER active and flow from there to the interval I_h. Using our previous definitions of $T(I)$ and h_{SN}, a sufficient condition to achieve this requirement is simply (Figure 14):

$$(R1) \quad h(T(I); h_{SN}, s_{SN}) \in I_h.$$

Next, it suffices to impose conditions under which the flow maps the interval I_h back to the curve of jump up knees where it intersects $\{s = s_{SN}\}$ at some time after ER has already activated but while ER is still active. To derive these, it suffices to consider the trajectories generated by the forward flow from the endpoints of I_h, namely $(h_{min}(I), s_{ER}^{min}(I))$ and $(h_{max}, s_{ER}^{min}(I))$. There are two aspects to this mapping requirement. One is that all trajectories have time to reach $\{s = s_{SN}\}$ from $\{s = s_{max}\}$ (Figure 14), a condition for which can be written in two equivalent forms using the notation we have introduced:

$$(R2) \quad s_{SN} > s_{ER}^{min}(I) \;\Leftrightarrow\; T_{active}^{ER}(I) > (1/\beta)\ln(s_{max}/s_{SN}).$$

The other aspect is that even the trajectory with minimal h value, which originates from $(h_{min}(I), s_{ER}^{min}(I))$ just before EP activates, must be able to reach (h_{SN}, s_{SN}) while ER is active. This trajectory flows forward from $(h_{min}(I), s_{max})$ under (2.3) with EP active, say to (h_{EP}, s_{EP}), and then continues forward under (2.3) with ER active from (h_{EP}, s_{max}) (Figure 14). Our additional sufficient condition is therefore

$$(R3) \quad h_{EP} > h_{SN}^{-},$$

where h_{SN}^{-} is derived from the backwards flow of (2.3) with ER active as in the previous subsection.

Conditions $(R1)-(R3)$, together with the earlier condition that $T_{active}^{EP}(I) < T_{active}^{ER}(I)$, are sufficient for all initial conditions within I_h to pass through (h_{SN}, s_{SN}), in the singular limit, albeit at different times, and reach the interior of I_h with ER active, which guarantees a stable rostral rhythm. We observe that our strong structural requirement that KE activation occurs at a saddle-node bifurcation of fast subsystem equilibria, which ensures a robust delay of KE activation relative to ER (and hence HF) activation as seen in the rostral rhythm, makes our remaining sufficient conditions for the existence of a stable rostral rhythm milder than those we invoked to ensure the existence of a stable pocket rhythm.

2.4.6 Key differentiator between rhythms

The work in this section supplies a variety of conditions on the relative positions of various trajectories such that when a set of inputs allows an appropriate collection of conditions to be satisfied, a pocket or rostral rhythm results. From this analysis and our numerical simulations, we can extract a key factor that distinguishes whether a rhythm generated by an input set is likely to be a pocket rhythm or a rostral rhythm. Given an initial condition on LK_{I_s} with ER active,

- inputs that lead to $h_{KE} > h_{max}$ at the termination of ER activity push the solution toward pocket.

- inputs that lead to $h_{KE} < h_{max}$ at the termination of ER activity push the solution toward rostral.

In other words, roughly speaking, the rhythm is selected based on whether or not the KE trajectory has access to a curve of jump down knees from which to enter the silent phase at the switch from ER activity to EP activity (Figure 15). Of course, this access depends on the time remaining with ER active after KE activates, which in turn depends on all relationships presented in the previous two subsections. Nonetheless, a numerical exploration of this timing issue can give a quick, rough idea of which solutions will be favored for a given input set, an option that would not have been obvious without our analysis. Further, this analysis provides a framework in which features can be examined thoroughly, which we harness in the next section.

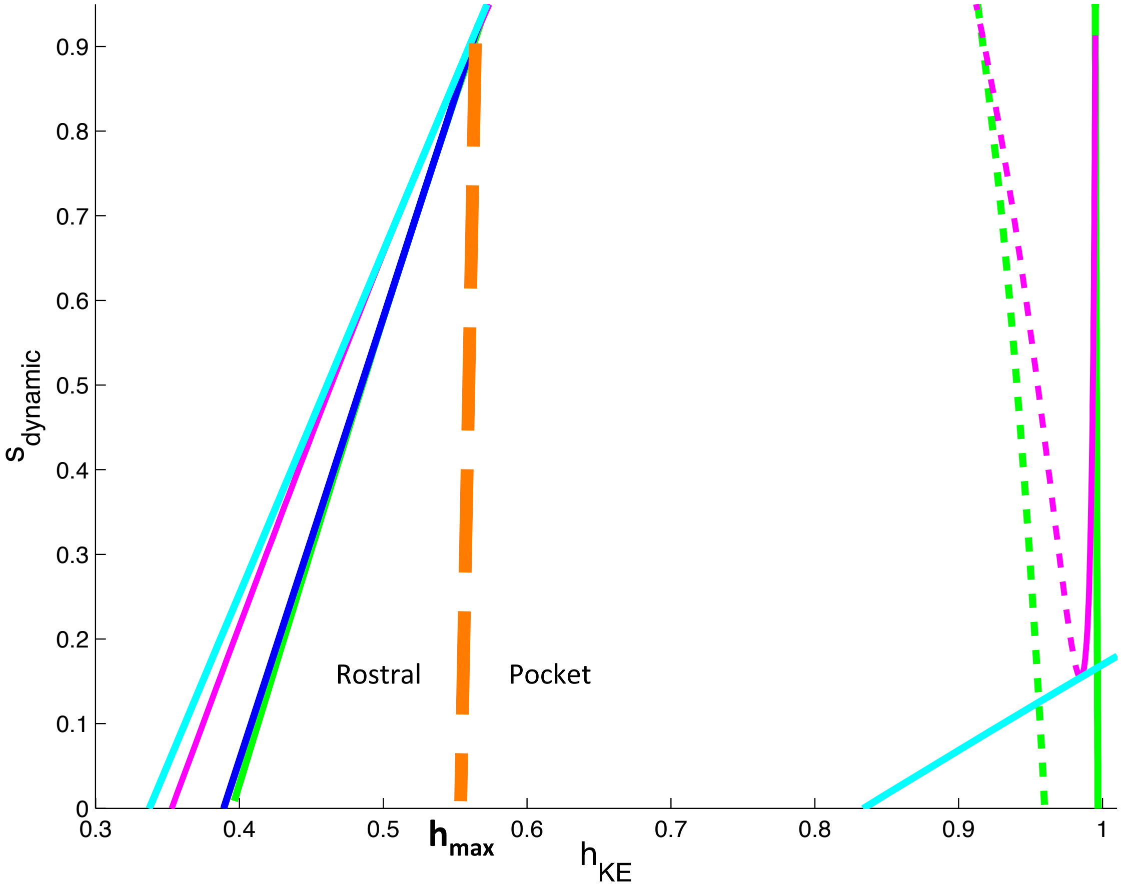

Figure 15: Key differentiator. The location of a trajectory at the end of the ER active phase, relative to h_{max}, ends up being the key separator in the slow phase plane between inputs that elicit rostral and those that elicit pocket.

In this section, we derived sufficient conditions on inputs for rostral versus pocket rhythm selections. We described the slow phase plane framework we developed for this system, and then we used this framework to derive and illustrate the sufficient conditions on inputs in both pocket and rostral. We also found a key differentiator between inputs that generate each rhythm. In the next section, we will reproduce dual-stimulation experiments [16], expand upon these to make predictions, and provide negative criteria that our collaborators can use to differentiate between parameter sets in practice.

2.5 EXPERIMENTS AND SIMULATIONS WITH INPUT SWITCHING

We can test the experimental relevance of our model by trying to simulate some additional experiments that have been performed involving the rostral and pocket rhythms. Furthermore, now that we understand the dynamic mechanisms underlying each rhythm and the rhythm selection process, we can understand the outcomes of simulations in these scenarios.

In their 1988 work seeking to further typify scratch and swim behavior, Currie and Stein [16] explored the presentation of rhythm-specific stimulation during ongoing scratch activity. For example, while the turtle was exhibiting the rostral scratch pattern (following stimulation in the rostral body region), stimulation was provided in the pocket body region, which could eventually lead to a period of blended rhythm, followed by the pocket scratch (Figure 1, Figure 16).

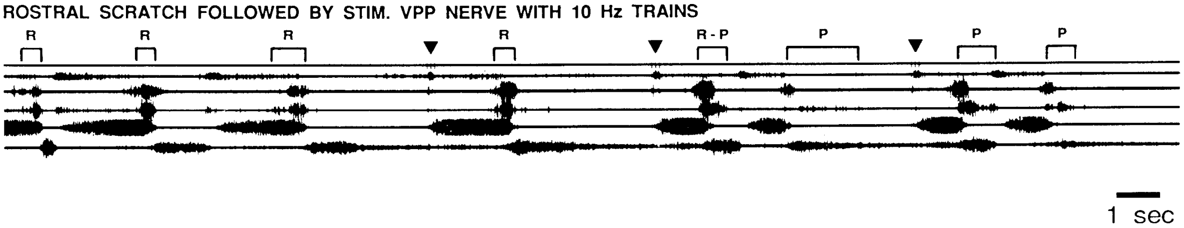

Figure 16: Currie and Stein 1988 experiments. Converting a rostral rhythm to a pocket rhythm. Bottom three traces show MN activity corresponding to KE, HF, and HE, respectively. Initial bouts of activity represent a rostral rhythm with large delay of KE activation relative to HF. Transient pulse stimulation of the VPP nerve (inverted triangles) eventually switches the network into a pocket rhythm. Figure source: Currie, S.N., Stein, P.: Electrical activation of the pocket scratch central pattern generator in the turtle. J Neurophysiol. 60, 2122–2137 (1988) [16]

To reproduce this experiment, we consider the result of an instantaneous switch of inputs. That is, a rostral input set, $I_{rostral}$, is given to the system. After several periods, at the end of a phase of HE activity (as in the experiment), the inputs are switched to a pocket input set, I_{pocket}. With both the Standard and Strong Cross-Excitation synaptic weights, this change in inputs leads to a similar transition to pocket as seen in the experiment (Figure 17).

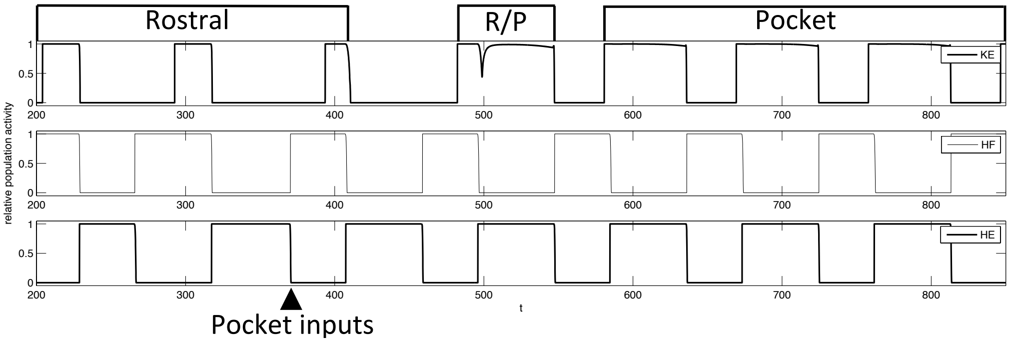

Figure 17: Simulation of Currie and Stein 1988 experiments. A switch from rostral inputs to pocket inputs, at the time indicated by the arrow, causes the model behavior to transition from rostral to blended output to pocket. Standard weights were used, with similar results obtained for SCE weights (not shown). Inputs: $I_{rostral} = \{i_{IP} = 0.19, i_{EP} = 0.17, i_{ER} = 0.19, i_{IR} = 0.17\}$, $I_{pocket} = \{i_{IP} = 0.17, i_{EP} = 0.19, i_{ER} = 0.17, i_{IR} = 0.19\}$.

Our phase plane analysis makes it easy to understand the switch in dynamics. Once pocket inputs are applied, KE still reaches the SN bifurcation and activates while EP and HF are active, as in rostral. But the pocket inputs shorten $T^{ER}_{active}(I)$, allowing EP and hence HE to take over before h_{KE} decays down to h_{max}. Thus KE remains active when EP/HE activates, yielding a cycle that blends features of rostral and pocket followed by rapid convergence to a pocket rhythm.

We also consider the reverse scenario of applying rostral inputs during an ongoing pocket rhythm. Interestingly, simulations of this manipulation yield different results depending on whether we use our Standard or SCE synaptic weights. In the Standard set up, interrupting pocket at the end of an HE cycle with two different input sets, each of which yields a rostral rhythm when applied to the model in a rest state, induces two qualitatively different behaviors. In one case, even with the rostral inputs, a rhythm that can be classified as pocket persists, although HF is active slightly longer than HE, unlike the prototypical pocket rhythm (Figure 18, top). In the other case, the rostral inputs cause a switch to the rostral rhythm (Figure 18, bottom).

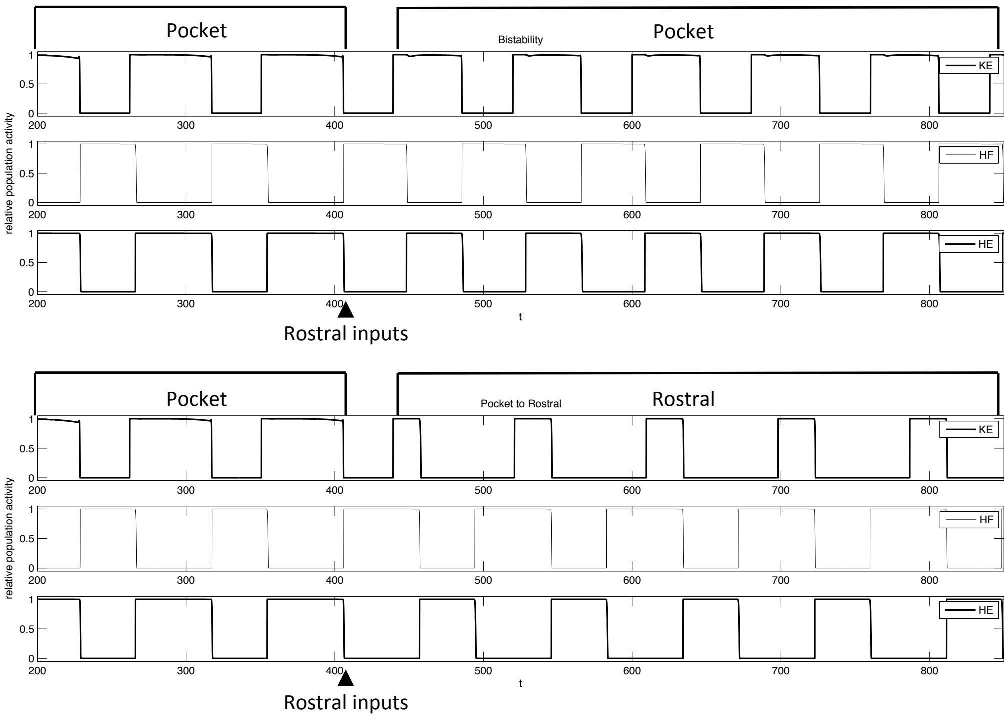

Figure 18: Pocket to rostral simulations. Applying rostral inputs during a pocket rhythm may or may not induce a switch to rostral. A pocket rhythm was induced using $I_{pocket} = \{i_{IP} = 0.17, i_{EP} = 0.19, i_{ER} = 0.17, i_{IR} = 0.19\}$. Inputs were switched at the time indicated by the arrows to one of two different input sets, each of which evoked rostral from rest. Top: $I^1_{rostral} = \{i_{IP} = 0.19, i_{EP} = 0.18, i_{ER} = 0.19, i_{IR} = 0.18\}$ maintains the pocket rhythm, and hence uncovers bistability in the system. Bottom: $I^2_{rostral} = \{i_{IP} = 0.19, i_{EP} = 0.17, i_{ER} = 0.19, i_{IR} = 0.17\}$ leads to switching behavior as seen in experiments [16].

In the case where pocket persists, we conclude that the rostral inputs that are applied render the system bistable. These inputs are closer to I_{pocket} than are other rostral inputs that do not reveal bistability. In particular, the stronger inputs to IR and EP in the former case cause an earlier switch from HF to HE, allowing pocket dynamics to be maintained. In the SCE set up, we only observe bistability when biologically unrealistic inputs are given to the interneurons and it occurs at fewer input sets than is the cases in the S case. In other words, the SCE set up suppresses bistability.

2.5.1 Explanation of bistability (and lack thereof)

The analysis presented in this subsection relies on the framework we develop in Section 2.4. The selection between the two cases illustrated in Figure 18 essentially comes down to a race between EP (corresponding to HE) and KE: from the activation of ER/HF, does EP reach the jump up knee before h_{KE} is able to decay to reach h_{max}? If EP does activate first, then the rhythm remains in pocket. If KE reaches h_{max} first, then a switch to rostral can occur. The data used to generate Figure 18 indicates that a decrease in i_{EP} promotes this switch. This idea can be investigated more closely through a series of numerical calculations of these quantities, with a few approximations motivated by the framework that the slow phase plane analysis provides.

Heuristically, we can see why SCE would tend to suppress bistability, based on the SCE synaptic weights (Figure 5). For a pocket rhythm to persist despite rostral inputs, the ER active phase must remain sufficiently short that EP can activate before h_{KE} drops to h_{max} (Figure 15). Because transitions in our networks occur by escape, this requirement means that EP or IR must be able to activate before the ER stays active too long. In SCE, however, the weights of synaptic inhibition from ER to IR and excitation from ER to IP are strong, relative to the S case. These synaptic connections are exactly the ones that would suppress the activation of EP and IR and thus prolong the ER active phase, causing KE to jump down with ER and inducing a switch from pocket to rostral.

We next considered a homotopy between the input sets within each parameter regime. In both the S and SCE parameter cases, $\lambda = 0$ corresponds to the pocket inputs and $\lambda = 1$ corresponds to the rostral inputs. In Figure 19, we plot the activation delay of knee extensor (red) and hip extensor (blue) relative to the activation of hip flexor. Delays that have negative values correspond to knee extensor synchronizing with hip extensor (pocket), delays that have positive values correspond to rostral synchrony, and delays that have a 0 value correspond to steady state, non-rhythmic solutions. This helps explain the existence of bistability in the S case: inputs that lead to rostral synchrony from rest occur at $\lambda = 0.1, 0.2,$ and 0.3, very close to the pocket inputs. When these inputs are given to a system already in pocket, the pocket rhythm may persist. In the SCE case, one may expect similar bistability to occur at inputs given by $\lambda = 0.3$, and indeed this is seen in simulation. However, such input values correspond to biologically unrealistic inputs, emphasizing that the existence of bistability in experiment corresponds to an unrealistic assumption in the set up of our model. Finally, it is worth noting that the bistability occurs in a much smaller range of inputs in the SCE case than in the S case, supporting that the SCE setup suppresses bistability. Additional parameter tuning may be able to eliminate the possibility of bistability entirely, while still maintaining biologically realistic inputs.

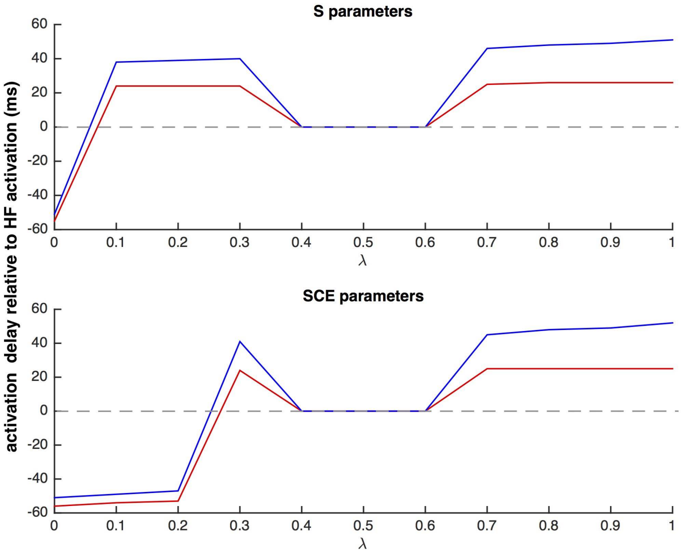

Figure 19: The activation delay of knee extensor (red) and hip extensor (blue) relative to the activation of hip flexor, as the homotopy parameter λ varies between pocket inputs ($\lambda = 0$) and rostral inputs ($\lambda = 1$) in each parameter set S and SCE. Delays that have negative values correspond to knee extensor synchronizing with hip extensor (pocket), delays that have positive values correspond to rostral synchrony, and delays that have a 0 value correspond to steady state, non-rhythmic solutions.

In this section, we reproduced dual-stimulation experiments [16], expanded upon these to make predictions, and provide negative criteria that our collaborators can use to differentiate between parameter sets in practice. In the next section, we consider input scaling simulations to make additional predictions about the relative contributions of excitation and inhibition to motoneuron duty cycle.

2.6 PREDICTIONS

The observation that some weight and input parameter sets yield bistability and others do not offers some potential for making predictions. That is, if bistability is observed experimentally, then we can conservatively state that it should rule out certain parameter combinations within the underlying rhythm generating circuit, if indeed that circuit is qualitatively represented by our model. For example, although our simulations were not exhaustive, together with the heuristic arguments we have provided they suggest that an observation of bistability of pocket and rostral rhythms in response rostral inputs would represent evidence against SCE weights, in which both the excitatory and the inhibitory interneurons projecting to HF are more strongly recruited by rostral stimulation than are the corresponding HE-projecting interneurons.

More generally, we can also observe that if a single circuit generates both pocket and rostral rhythms, then one rhythm may be more resistant to input-induced switching than the other, as we have seen by introducing rostral input during an ongoing pocket rhythm. This is an important observation: Suppose that two separate modules generated pocket and rostral rhythms. In that case, introducing a rostral input during ongoing pocket would necessarily recruit the rostral module, likely perturbing the pocket rhythm in some way that is more significant than seen in our simulations. Hence, bistability may be used to help distinguish between these possible rhythm generation frameworks (see also [31]).

Additionally, we can consider the effect of scaling inputs to the interneurons. We consider what happens in the SCE regime when all four inputs are scaled by the same factor, only the E inputs (to EP, ER) are scaled by the same factor, or only the I inputs (to IP, IR) are scaled by the same factor (Figure 20). In the first case (Figure 20, left), we see that increasing inputs (black to gray) leads to a decrease in active phase length for both KE and the dominant IN population (namely HE in pocket and HF in rostral) with almost no change in phase duration for the other population. This result, which is consistent with the stipulation that phase transitions occur by escape and also with past work exploring asymmetries in persistent sodium half-center oscillator models [56], [20], represents a testable prediction. Next, we find that scaling only the inputs to the excitatory INs leads to almost the same changes in active phase durations as occur when all inputs are scaled (Figure 20, left versus middle), while there is virtually no change in active phase length across different scalings of the inputs to the inhibitory INs (Figure 20, right). These results indicate that the escape of the excitatory INs from the silent phase largely controls rhythm frequencies. In fact, we find that the external input to the inhibitory interneurons can be removed and the synchrony patterns of the rhythms (but not the delay in rostral) can be maintained (data not shown), because the excitatory INs still recruit the inhibitory populations to become active. These predictions are more difficult to test, given that these populations of interneurons have not yet been identified, but remain for future experimental consideration.

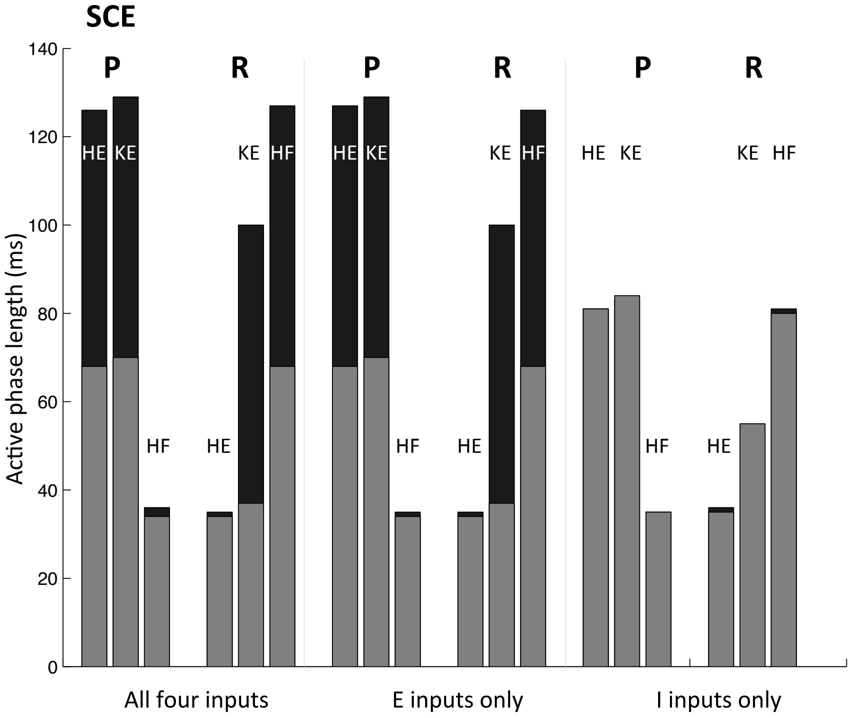

Figure 20: SCE duty cycles. Effect of input scaling on phase durations in SCE regime. The black bars represent the durations of the active phases of HE, KE, and HF when the indicated inputs are uniformly decreased by multiplication by a scaling factor less than one, just large enough to maintain each rhythm. The gray bars represent the durations of the active phases of HE, KE, and HF when the scaling factor is greater than one, near the upper bound for maintaining each rhythm.

We repeat this experiment with the S regime (Figure 21) and find generally very similar results. However, it is worth noting that, in the S regime, the changes in active phase durations across similar scaling is much less than in the SCE regime. Additionally, there is a much greater change in active phase durations in rostral than in pocket. These differences, in addition to the bistability observed, may serve to differentiate the S regime from the SCE regime in practice.

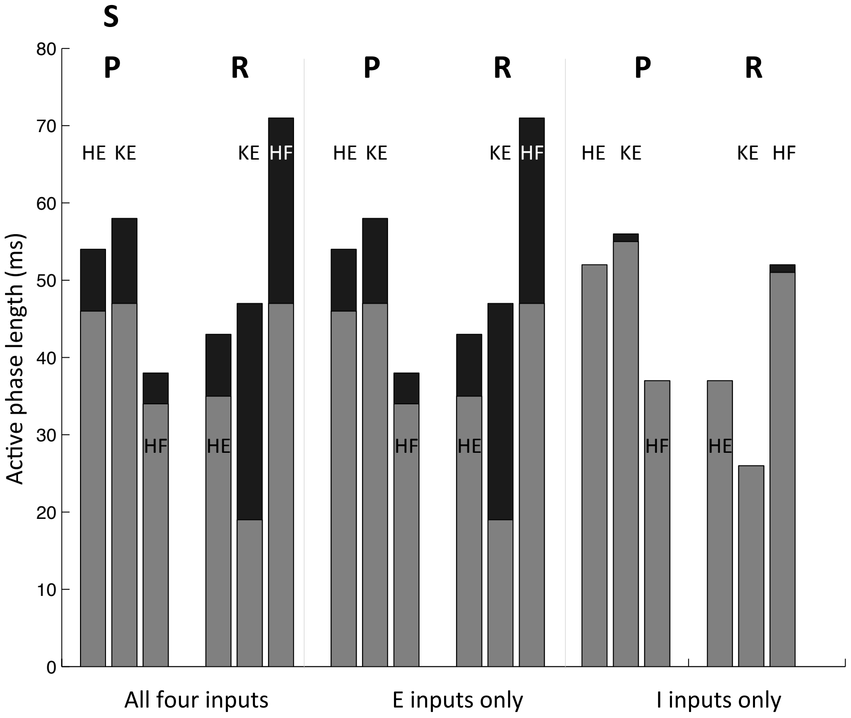

Figure 21: S duty cycles. Effect of input scaling on phase durations in S regime. The black bars represent the durations of the active phases of HE, KE, and HF when the indicated inputs are uniformly decreased by multiplication by a scaling factor less than one, just large enough to maintain each rhythm. The gray bars represent the durations of the active phases of HE, KE, and HF when the scaling factor is greater than one, near the upper bound for maintaining each rhythm.

In this section, we considered input scaling simulations to make additional predictions about the relative contributions of excitation and inhibition to motoneuron duty cycle.

2.7 DISCUSSION

It has been postulated that turtle scratching and swimming arise when "behavioral modules" interact and combine to control "muscle synergies" producing appropriately coordinated motor outputs [9], but there is a large gap between such an abstract statement and concrete hypotheses about the neuronal networks involved. While a specific wiring diagram for a single circuit that could parsimoniously drive both pocket and rostral scratching has been proposed [5], it is well known that connectivity diagrams alone do not uniquely map to output patterns [1]. We have performed a computational and mathematical study to investigate whether the proposed unified CPG network, which features only hip-related populations of interneurons, could indeed be responsible for the generation of two different turtle scratch rhythms with distinct knee-hip synchrony patterns. Importantly, these patterns are selected by changing external inputs to the interneurons, with the same synaptic weights between interneurons, and from interneurons to motoneurons, preserved for both. Through the use of slow phase plane arguments, we were able to explain how particular phase space and bifurcation structures underlie the generation of the rhythms and to derive sufficient conditions on these structures that guarantee the existence of stable rhythms. This analysis was possible due to time scale decomposition and certain model reductions, despite the relative high-dimensionality of the model system; because our conditions are stated in terms of dynamic structures, they apply beyond the particular model features, such as a slowly inactivating persistent sodium current, used in our simulations. Even with model reductions, the synaptic variables evolving during each stage of each rhythm were hybrid variables, representing combined effects of excitatory and inhibitory inputs, which was one unusual aspect of our analysis.

Past research has focused on several different aspects that arise in multi-functionality, including the general organizing principles governing CPGs [39, 29], and the notion that an organism exhibits different motor patterns by selecting different CPGs [34], which may be collections of burst-capable unit CPGs that each control a set of synergistic muscles [27]. Similarly, recent experimental work in mice [30] found that the hindlimb locomotor network is composed of intrinsically rhythmic modules that each drive a pool of motoneurons.

Consistent with the unit CPG framework, the model that we consider includes separate hip extensor and hip flexor interneuron pairs (EP and IP, ER and IR); although each individual population is tonically active in the absence on inputs, each pair can generate bursts through a mechanism of escape from reciprocal inhibition, consistent with previous related work [31]. Our interneuron network includes fixed interconnections and projections both to antagonist hip interneurons and to hip motoneurons and is able to generate multiple rhythms under changes in inputs that alter the relative durations of the unit CPGs, without changing network connections. In contrast to the unit CPG idea, however, the hip interneurons also control knee extensor motoneurons in the model. Despite the multi-tasking demanded of the unit CPGs, we find that the network can generate multiple motor patterns, selected by tuning the relative strengths of their tonic inputs. That networks of unit CPGs can be influenced to demonstrate different activity patterns is not surprising, given the wide variety of activity patterns that can be elicited from a single neuron [17, 18], but the idea that CPGs for one unit can also be harnessed to control the timing of another joint is relatively novel. Although this idea makes sense in terms of efficient use of neuronal resources, evolutionary principles, and the observation that individual interneurons are active during multiple forms of activity [4], it remains to be determined whether this framework offers enough robustness for functional rhythm generation.

A distinctive feature of one of the rhythms considered, the rostral scratch, is a delay in the onset of KE motoneuron activity relative to HF onset. While synchronization ([58, 24]) and near-synchronization [8] in networks of planar neuron models with strong synaptic coupling has been well studied, the delay we consider appears to be novel. This delay significantly restricts the choices of synaptic weights to KE for which both rhythms can be elicited. The resulting phase plane structure leads us to observe that, given that the sufficient conditions on synaptic weights hold, the rhythm selected by a particular input set is largely determined by the position of the slow variable coordinate of a particular trajectory segment relative to a key value h_{max} at the termination of ER activity (Figure 15).

Unfortunately, from an experimental point of view, the specific rhythm generation conditions in our model are not accessible for many reasons, starting with the fact that the interneuron populations in the CPG have not been identified. However, our analysis yields the observation that in the framework we have considered, the KE motoneuron must activate slightly before the HE during the pocket rhythm, and this is exactly what is observed experimentally [22], which offers some validation for our approach. Furthermore, simulation of the model can help guide future experiments. In particular, the model network can exhibit bistability to rostral scratch inputs for some of the parameter values considered, which seems unlikely to arise with separate pocket and rostral generation modules (see also [31]). Thus, future experiments to explore this form of bistability could be useful. The slow phase plane approach that we have presented provides a framework that can be used to make predictions about specific experiments and to explain the mechanisms underlying observed outcomes. Our simulations also predict that changes in inputs to the CPG that are not strong enough to destroy an ongoing rhythm will alter the active phase durations of the hip MN that is dominant in that rhythm and of the knee extensor MN while leaving the other hip MN activity period almost entirely unchanged, and that these changes are controlled by the excitatory INs in the CPG. These outcomes likely result from the underlying assumption that activity transitions in our model occur through escape [69, 56], based on past experimentally constrained work modeling turtle motor CPGs [31], and alternative transition mechanisms should be considered if these predictions are falsified in future experiments.

During rostral scratching, hip extensor deletions can occur [66, 62]. In these deletions, hip extensor is silent while knee extensor behavior is entirely preserved (synchrony with hip flexor after a delay, periods of full activity and full quiescence); hip flexor fails to shut down fully during its quiescent period, as during normal rostral. This lack of quiescence presumably results from the absence of inhibition from hip extensor related motor pools. These deletions occur unpredictably in some preparations, although the frequency can be increased through particular experimental techniques [62]. Due to a combination of the proposed architecture and the use of deterministic differential equations to describe population behavior, it is not possible to reproduce this behavior fully in our model. The only way to shut down hip extensor behavior in both the standard and strong cross-excitation architectures, by only changing inputs and without changing synaptic weights from interneuron motor pools to the hip extensor (which would be a trivial but non-biological solution), is by decreasing input to IR and EP until oscillations are lost (Figure 2). While this does lead to tonic activity in hip flexor as desired, it also leads to tonic activity in knee extensor. One possible way to resolve this issue is to suppose that an additional source of inputs, not included in our model, provides enough inhibition to shut down knee extensor motoneurons while ER input is low. A need to invoke additional inputs to explain deletions suggests that hip-related motor pools may account for synchrony and relative timing of scratch rhythms but may not be sufficient to fully capture all motor behaviors observed. Although experiments suggest that inputs to knee extensor motoneurons are hip-related, it may be that knee motor pools (as in the standard UPG approach to rhythm generation) are present in a secondary role and that interneurons related to knee flexor activity provide inhibition that contributes to the termination of knee extensor activity. Alternatively, stochasticity may need to be taken into account to capture the full range of scratch rhythm phenomenology [38, 36]. Certainly, our model could be expanded to include additional neuron pools or stochastic mechanisms. Additional experimental work to constrain the mechanisms underlying deletions would be beneficial to help guide efforts in this direction.

It has been suggested that oscillations underlying turtle motor rhythms may be driven by concurrent excitation and inhibition, based on analysis of data showing that the estimated synaptic conductances for excitation and inhibition to turtle motoneurons oscillate in phase [3]. It is worth noting, however, that for the most part, neither the type (hip extensor, hip flexor, and so on) of motoneurons from which recordings were obtained nor the source of synaptic inputs was identified, so it is hard to know how to interpret these results. Past reviews [29] hypothesize that this may be an artifact of the experimental setup or a feature unique to motor pattern generation in turtles (as opposed to say mammals). These findings contrast with the traditional reciprocal model in which motoneurons receive synaptic excitation and inhibition in antiphase [56, 62], as imposed by the mutual inhibition between EP and IP and between ER and IR in our model network. Note that we chose this mutually inhibitory structure on experimental grounds: It has long been established that HE is active together with its excitatory motor pool of interneurons, EP; additionally, HE and HF activate in antiphase (Figure 1)[50]. The simplest way to meet these benchmarks is for EP to be active with IR and ER with IP, as imposed by mutual inhibition. Nonetheless, it would be interesting to explore how stochastic effects might allow multi-functionality of a rhythm generating circuit despite less segregated excitatory and inhibitory inputs to its motoneurons, especially since rhythm generation in several other CPG circuits involves some mixture of reciprocal and concurrent excitation and inhibition (see references in [62]).

Another important future challenge will be to bring this work together with other previous modeling efforts [31] to develop a system capable of generating all four observed motor patterns, forward swim and rostral, pocket, and caudal scratch. One possible approach would be the use of genetic algorithms to derive optimal CPG network structures [15, 2] or to determine parameter values necessary to coordinate multiple CPGs to generate multiple rhythms [34]. It is not clear what would constitute a practically useful objective function for a genetic algorithm approach, however. Including more of the known details about the ionic currents in turtle motoneurons [7] would be another way to tie our modeling more closely to the biology of turtle motor rhythms in future works.

3.0 STOCHASTIC SIMULATIONS OF TURTLE SCRATCH RHYTHMS

In the previous chapter, we introduced a deterministic relaxation oscillator based model for generating two different turtle scratch rhythms. We used dynamical systems tools to derive sufficient conditions for rhythm selection by inputs to a single network. Using insights from this analysis, we were able to make several testable predictions for use by experimentalists. The deterministic approach allowed the use of a well-established mathematical framework to derive sufficient conditions on parameters for the generation of multiple rhythms. However, due to the difficulty of identifying the interneurons involved in rhythm generation in vertebrates, the significant assumptions underlying the architecture used are potentially unrealistic. In particular, for the sake of tractability, strict antiphase relationships in the activity patterns of excitatory and inhibitory interneurons in the CPG were assumed in the analysis presented in Chapter 2. Some experimental results have proposed that such relationships are not the case during rostral scratching [51].

In this chapter, we present simulations from a second model of turtle scratching behavior. Experimental results regarding changes in the firing rate of motoneurons cannot be reproduced by a relaxation oscillator model, and these experimental findings motivate the introduction of a spiking model with stochasticity [5]. Previous authors (Figure 2 [5]) proposed that hip-related interneurons also provide input (or even control) knee extensor motoneurons. Using this stochastic spiking model, we explore the transformation of hip interneuron signals with prescribed properties into knee extensor motoneuron output signals. Non-exhaustive simulations exploring the relative roles of different parameters in the model are presented as well.

In Section 3.1, we provide an overview of experimental results that motivate our stochastic spiking model, and we summarize the features we our model must reproduce. The details of our model and the parameter regimes we consider are presented in Section 3.2. In Section 3.3, we show that our model produces rhythms that meet our experimental benchmarks from Section 3.1, and we show by example that the inclusion of noise improves the rhythms our model produces. In Section 3.4, we use our model to make predictions about the relative importance of excitation and inhibition to rhythm generation. We explore the impact of different model parameters in Section 3.5 and use these explorations to make suggestions for future avenues for experimentalists. In the discussion, Section 3.6, we summarize our results and provide future avenues for research. We end in Section 3.7 with a summary of the mathematical methods used in this chapter.

3.1 EXPERIMENTAL BACKGROUND

The relaxation oscillator model introduced in Chapter 2 can only reproduce experimental results regarding active versus silent behavior. A different model must be used to investigate rate changes in motoneuron spiking under different conditions. For example, research performed by Berkowitz and Stein in 1994 [5] demonstrates that most motoneurons 'generated spikes at a higher rate when they were active with weaker rhythmic modulation.' Their figure demonstrating this is reproduced here, Figure 22. "Unit" refers to a descending propriospinal axon. "VP-HP" is the ipsilateral hip flexor muscle nerve. When the unit fires at a higher frequency (Unit Freq. Aa in Figure 22), its activity is less modulated (Unit number 1 Aa). The hip muscle nerve, VP-HP is still rhythmic and would correspond to the activity of HF in our simulations. As the frequency of the unit decreases (Ab, Ac), the activity of the unit becomes more modulated, and the hip muscle nerve experiences shorter active durations. Berkowitz and Stein propose two different reasons for this result:

- (E1) The activity of the observed neurons had saturated at peak firing rate and additional rhythmic depolarization would not affect the firing rate.
- (E2) Rhythmic inhibition is more important than rhythmic excitation in generating the turtle scratch rhythms and thus whenever a motoneuron receives 'a greater proportion of inhibition, it fires at a lower rate but with stronger rhythmic modulation.'

Testing this result motivates the introduction of a second stochastic spiking model so that rate differences of motoneuron spiking can be better understood. In such a framework, the relative contribution of the rhythmicity of excitatory and inhibitory inputs to motoneurons can be explored. Additionally, the relaxation oscillator model presented in Chapter 2 relies very heavily on the assumption of strict antiphase relationships in the activity patterns of excitatory and inhibitory interneurons in the CPG. While this is a traditional simplifying assumption that does not necessarily contradict experimental observations, there is significant early work [50, 51] suggesting that there may be temporal overlap during some (but not all) of the rhythm period, see Figure 23. In particular, it was observed that in rostral, knee extensor may receive contemporary excitation and inhibition prior to activation, excitation during the active phase, and inhibition following the active phase. Pocket is characterized by the traditional antiphase relationships between excitation and inhibition used previously. Some more recent work [3] has found that motoneurons may actually experience concurrent excitation and inhibition throughout scratch rhythms, although the motoneurons in this work were not type-identified.

To summarize the experimental features we wish to reproduce:

- Motoneurons experience lower firing rates but increased rhythmic modulation in the presence of a greater proportion of inhibitory inputs, Figure 22.
- HF and HE activate in antiphase and do not receive temporally overlapping excitation and inhibition in pocket. They do receive temporally overlapping excitation and inhibition in rostral, Figure 23.
- KE is activated and terminates with HE in pocket. KE is activated and terminates with HF with a delay in onset in rostral.

Therefore, in this chapter, we use computational methods and numerical simulations to examine possible patterns of interneuron activity to the knee extensor motoneurons that are consistent with timing of knee extensor activation in pocket and rostral rhythms. We also consider the potential roles of stochasticity and the question of whether noise is required to achieve the pocket and rostral rhythms with overlapping excitatory and inhibitory inputs to motoneurons.

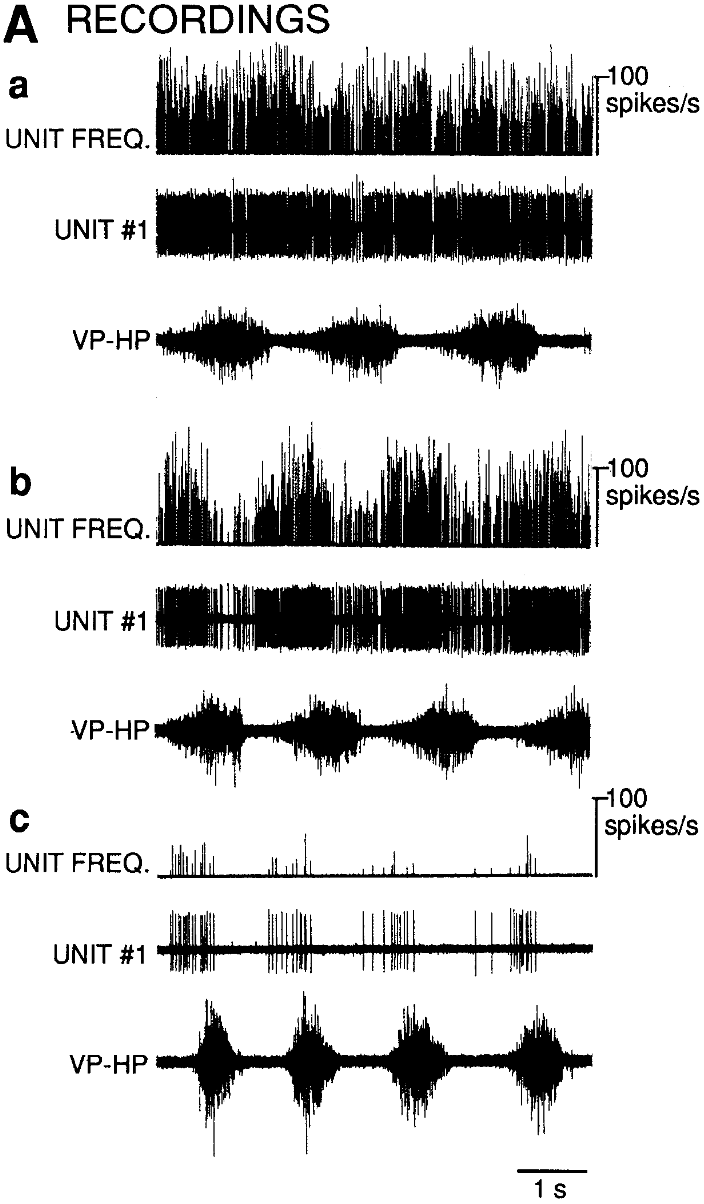

Figure 22: Relationship between a motoneuron unit's mean firing rate and the strength of rhythmic modulation of the unit's activity for different sites of stimulation. A, Concurrent recordings of a descending propriospinal axon and the ipsilateral VP-HP (hip flexor) muscle nerve, showing the association between lower unit firing rates and stronger rhythmic modulation of the unit's activity, for three stimulation sites: a, SP2; b, femoral 0; c, femoral 8. UNIT FREQ. instantaneous firing rate of recorded unit. Figure source: Berkowitz, A., Stein, P.: Activity of descending propriospinal axons in the turtle hindlimb enlargement during two forms of fictive scratching: phase analyses. J Neurosci. 14(8), 5105–5119 (1994) [5]

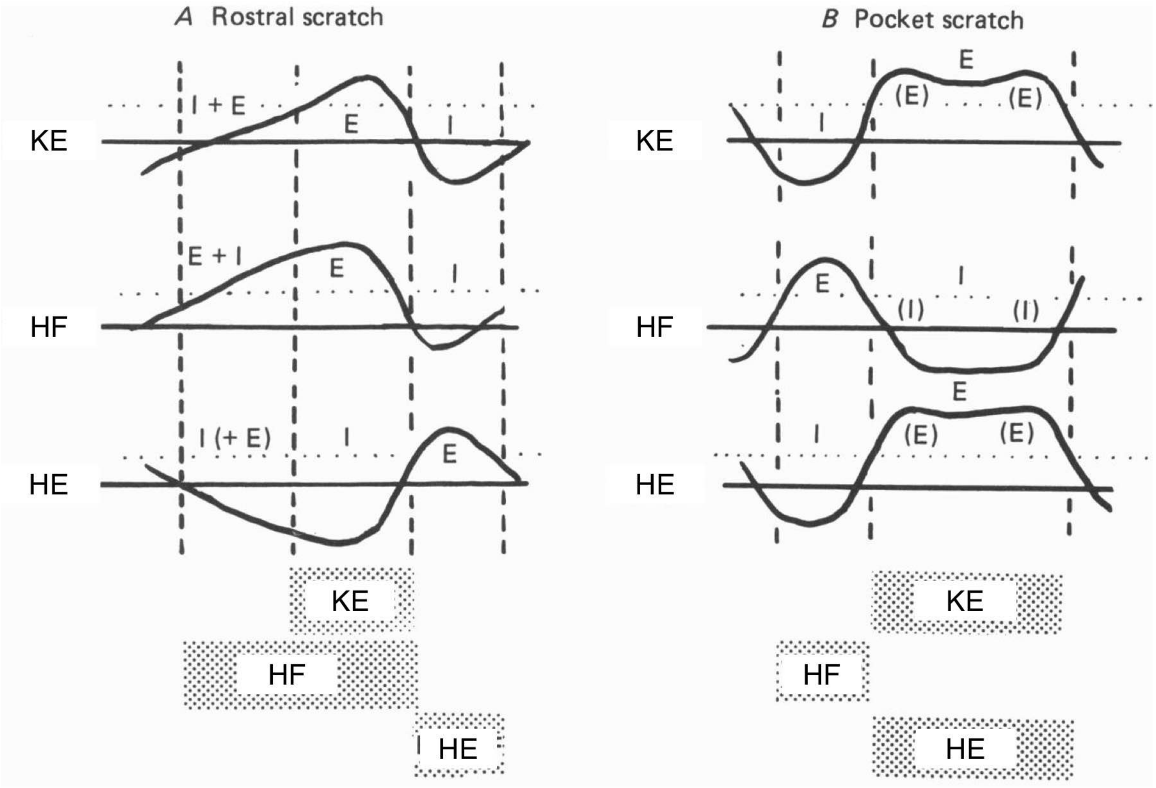

Figure 23: Schematic comparing voltage changes in knee extensor (KE), hip flexor (HF), and hip extensor (HE) motoneurons during rostral and pocket scratch. Motor pattern depicting timing of corresponding motor pool is shown at the bottom of each panel. Firing thresholds are shown as dotted horizontal line. I and E indicate synaptic inputs to motoneurons derived from data. Letters in parentheses indicate sign of synaptic drive predicted from preliminary observations. A, voltage changes during rostral scratch show similarity in quality of knee extensor and hip flexor voltage trajectories with difference in onset of firing. Hip flexor and hip extensor traces shown as near-mirror images. Prior to knee extensor activation, knee extensor and hip flexor are found to receive contemporary excitation and inhibition. The cessation of inhibition theoretically allows knee extensor to fire with a delay in onset. B, voltage changes during pocket scratch show synergy between knee extensor and hip extensor motoneurons, with antagonist drive to hip flexor motoneuron. Figure source: Stein, P., Robertson, G.: Synaptic control of hindlimb motoneurones during three forms of the fictive scratch reflex in the turtle. J Physiol. 404(1), 101-128 (1988) [51]

In this section, we summarized experimental results that motivated our implementation of a stochastic spiking model for turtle scratching, and we identified a series of features that a successful model will reproduce. In the next section, we will present the architecture we implement, provide a mathematical description of neurons in our model, and describe the parameter sets we use in simulations.

3.2 MODEL DESCRIPTION

A possible motor CPG architecture differing from the traditional unit burst generator view was proposed based on experimental results on turtle scratching rhythms [5]. Our implementation of their architecture for this model is given in Figure 24. Each hip motoneuron has its own excitatory and inhibitory pools of interneurons: hip flexor corresponds to ER (excitatory) and IR (inhibitory), hip extensor to EP (excitatory) and IP (inhibitory). Berkowitz and Stein [5] found strong experimental justification for a network that uses only hip-related interneuron populations to generate the correct knee-hip synchrony patterns found in rostral and pocket scratch (supported by our findings outlined in Chapter 2). Based on experimental findings, some preliminary assumptions are: hip extensor activates during activation of its excitatory motor pool EP and terminates during activation of its inhibitory motor pool IP, and hip flexor activates during activation of its excitatory motor pool ER and terminates during activation of its inhibitory motor pool IR [50, 51].

Rather than implement all connections among the interneurons in this model (grey connections in Figure 24), we prescribe their outputs and model their connections to the motoneurons (black connections). This allows exploration of more general synchronization properties and requirements rather than modeling the strong internal dynamics of populations. This also leads to the possibility of more experimentally tractable findings: many of our conclusions will focus strictly on inputs to the motoneurons, rather than the inputs to the hypothetical (and as yet unidentified) interneurons used in the model in Chapter 2. Indeed, this is in keeping with recent work [38] demonstrating that in a simplified setting, strong synaptic correlations may play a larger role in turtle scratch rhythm generation than strong intrinsic dynamics.

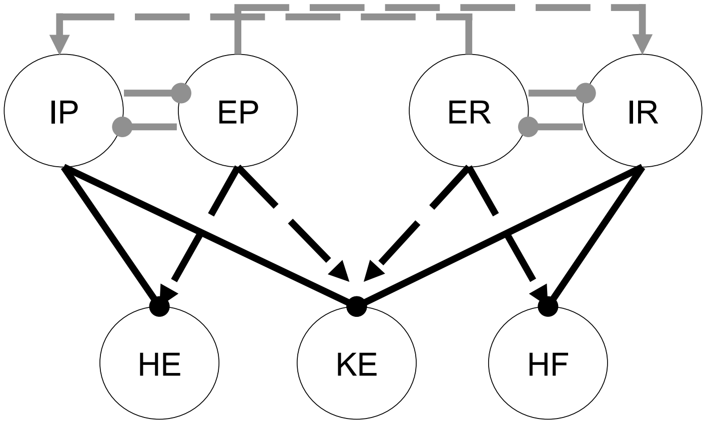

Figure 24: Architecture for the stochastic spiking model. The gray connections among the interneurons represent those implemented in the previous chapter. In this model, only the output from the interneuron layer to the motoneurons is implemented, shown as black connections.

We model the interneuron output as follows. In a particular rhythm (rostral or pocket), one side of the network (ER/IR or EP/IP) would be more strongly stimulated than the other; for example, ER and IR in rostral. The synaptic output of the stimulated side is modeled as a sine wave - the output is waxing and waning periodically to be consistent with some of the gradual changes in hypothesized inputs to motoneurons shown in Figure 23. The results from this choice are similar to those obtained when the stimulated side is modeled as a series of spikes arriving deterministically at a rate given by a sine wave. Modeling the synaptic output as a sine wave directly (instead of such a spike train) is more analytically tractable. The motivation is that the stimulated side is bursting strongly, overcoming any natural noise in the synapse. We will often refer to the stimulated side as the deterministic side. The non-stimulated side (or stochastic side) is modeled as a series of pulses, arriving in time as an inhomogeneous Poisson process with a rate $\lambda(t)$, also a sine wave. (See equations (3.1), (3.2), (3.3)). The non-stimulated side fires more sporadically than the stimulated side, but its output still presumably varies periodically over time since the non-stimulated hip motoneuron still exhibits rhythmic activity. Because hip extensor and hip flexor must be in antiphase, we do consider EP and ER to be in antiphase with each other. Similarly, IP and IR are in antiphase with each other. We introduce a parameter to represent the phase shift between IR and ER, ϕ. An example of such interneuron output is shown in Figure 25, top. The averages over 5000 trials for $s_{IP}(t)$ and $s_{EP}(t)$ are given in Figure 25, bottom.

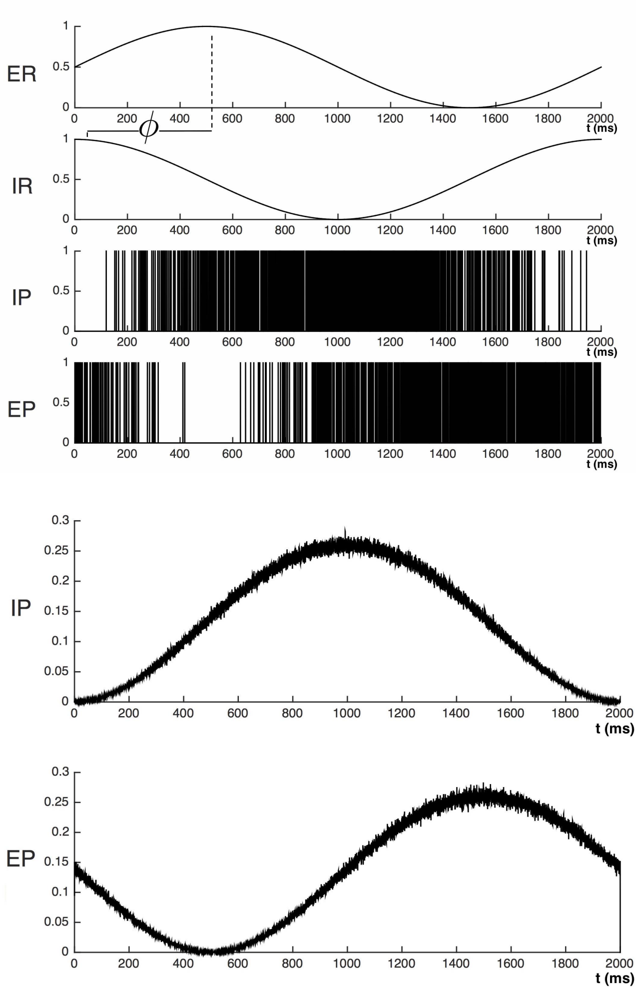

Figure 25: Top: Typical interneuron output for the rostral case with $\phi = \pi/2$ for clear visual separation. The traces labeled ER, IR, EP, IP are $s_{ER}(t), s_{IR}(t), s_{EP}(t), s_{IP}(t)$ in equation (3.2). The peaks of excitation are in antiphase and the peaks of inhibition are in antiphase. Bottom: The average over 5000 trials for $s_{IP}(t)$ and $s_{EP}(t)$, labeled IP and EP respectively.

.

Mathematically, the motoneurons are modeled as leaky integrate-and-fire (LIF) neurons:

$$\begin{aligned}
\tau_{KE}\dot{V_{KE}} &= \mu - V_{KE} + (g_{IP}s_{IP} + g_{IR}s_{IR})(V_{inh} - V_{KE}) \\
&\quad +(g_{EP}s_{EP} + g_{ER}s_{ER})(V_{exc} - V_{KE}) \\
\tau_{HE}\dot{V_{HE}} &= \mu - V_{HE} + g_{IP}s_{IP}(V_{inh} - V_{HE}) + g_{EP}s_{EP}(V_{exc} - V_{HE}) \\
\tau_{HF}\dot{V_{HF}} &= \mu - V_{HF} + g_{IR}s_{IR}(V_{inh} - V_{HF}) + g_{ER}s_{ER}(V_{exc} - V_{HF}) \\
V_{t^-} = 1 \implies V_{t^+} = -1
\end{aligned} \tag{3.1}$$

where τ_i is the time constant for population i, V_i denotes population activity for population i, μ is the leak reversal activity, g_j denotes synaptic weight from population j, and s_j denotes synaptic output from population j as described in Figure 25. All synaptic inputs are defined with $g_j > 0$; whether a synaptic input is excitatory or inhibitory is determined by its reversal potential V_{inh}, V_{exc}. There are times when it is more convenient to indicate the synaptic weight from the excitatory stochastic population more generally, g_{stochE}, meaning g_{ER} in pocket and g_{EP} in rostral. Similarly, g_{stochI} is a convenient term for g_{IR} in pocket and g_{IP} in rostral, g_{detE} for g_{EP} in pocket and g_{ER} in rostral, and g_{detI} for g_{IP} in pocket and g_{IR} in rostral. Values of g_j are varied and are discussed as they arise in our analysis.

For rostral:

$$\begin{aligned}
s_{IP}(t) &= \textstyle\sum_{t_i} \delta(t - t_i) \\
s_{EP}(t) &= \textstyle\sum_{t_e} \delta(t - t_e) \\
s_{IR}(t) &= \lambda_I^{mid} + \lambda_I^{mid}\sin(2\pi f t + \phi) \\
s_{ER}(t) &= \lambda_E^{mid} + \lambda_E^{mid}\sin(2\pi f t) \\
\\
\lambda_I(t) &= \lambda_I^{mid} + \lambda_I^{mid}\sin(2\pi f t + \pi + \phi) \\
\lambda_E(t) &= \lambda_E^{mid} + \lambda_E^{mid}\sin(2\pi f t + \pi) \\
\phi &= \pi/2
\end{aligned} \tag{3.2}$$

where t_i (t_e) are the spike times of the inhibitory (excitatory) inhomogeneous Poisson process, arriving at a rate $\lambda_I(t)$ ($\lambda_E(t)$). $\lambda_{E,I}^{mid}$ are the parameters used to control the total amplitude of the sine waves. $\lambda_{E,I}^{mid}$ vary and are discussed throughout our analysis.

For pocket:

$$\begin{aligned}
s_{IP}(t) &= \lambda_I^{mid} + \lambda_I^{mid}\sin(2\pi f t + \phi) \\
s_{EP}(t) &= \lambda_E^{mid} + \lambda_E^{mid}\sin(2\pi f t) \\
s_{IR}(t) &= \textstyle\sum_{t_i} \delta(t - t_i) \\
s_{ER}(t) &= \textstyle\sum_{t_e} \delta(t - t_e) \\
\\
\lambda_I(t) &= \lambda_I^{mid} + \lambda_I^{mid}\sin(2\pi f t + \pi + \phi) \\
\lambda_E(t) &= \lambda_E^{mid} + \lambda_E^{mid}\sin(2\pi f t + \pi) \\
\phi &= \pi
\end{aligned} \tag{3.3}$$

Handling the Poisson spikes takes some care, due to the required integration of $\delta(t)V(t)$ terms on the right hand side of equation (3.1). δ spikes are treated as short rectangular pulses to be integrated over. This translates to a voltage change from V to $V + \Delta V$ on a time step during which a stochastic arrival time t occurs.

To calculate ΔV, consider the arrival of a single rectangular pulse of height g at time t, lasting from time t to time $t + \hat{t}$. Then the differential equation $\tau V' = g(V_{rev} - V)$ is integrated to examine the effect of the pulse on voltage. Solving this first order linear differential equation gives $\Delta V = V(t + \hat{t}) - V(t) = (1 - e^{-\frac{g\hat{t}}{\tau}})(V_{rev} - V)$. Taking the limit as $\hat{t} \to \tau$ to represent a δ function, we get that the effect of a single pulse has the effect of changing the voltage from V to $V + \Delta V$ on a time step during the pulse occurs, for $\Delta V = (1 - e^{-g})(V_{rev} - V)$.

3.2.1 Synaptic parameter regimes

We consider two qualitatively different parameter regimes: a Symmetric regime in which multi-functionality can be examined, and an Asymmetric regime in which recruitment of knee extensor can be more broadly explored. Special focus is given to the behavior of knee extensor because it is more complicated than either hip motoneuron, receiving four overlapping synaptic inputs rather than two. Rostral is taken as a starting point over pocket because the relationship among the interneurons appears more complicated due to the excitation and inhibition overlap suggested by Figure 23, and because the delay in knee extensor onset relative to hip flexor has historically been a more difficult feature to capture [31, 57].

To switch between pocket and rostral rhythms in either regime, synaptic weights are not changed; rather, it is only the phase relationship of the interneurons ϕ, and the pair classified as deterministic or stochastic that changes: ER and IR are considered deterministic in rostral with $\phi = \pi/2$, and EP and IP are considered deterministic in pocket with $\phi = \pi$ (equations (3.2) and (3.3)). The effects of phase are examined in section 3.5.2.

Symmetric regime First, assume the connections in the network are symmetric (synaptic parameters from ER/IR are the same as from EP/IP) and do not change when the animal switches between pocket or rostral rhythms. The synaptic weights to knee extensor are $g_{ER} = g_{EP} = 0.8, g_{IR} = g_{IP} = 0.2$, with $\lambda_{E,I}(t)$ oscillating between 0 and 1. The synaptic weights are chosen such that for the rostral shift used, $\phi = \pi/2$, the deterministic inputs alone (ER and IR) are not sufficient to allow knee extensor to spike. This case uses $\tau_{KE} = \tau_{HE} = \tau_{HF} = 1.7$. The time constant can be decreased to 1 in the case of higher frequency input signals to the motoneurons.

To thoroughly examine the role of noise, we also consider the following scenario: the spike rate of the stochastically modeled side is switched on from 0 at a set time, after which spikes are generated by a homogeneous Poisson process with constant rate $\lambda_{E,I}(t) = \lambda_{E,I}^{mid}$. This is demonstrated in Figure 32.

Asymmetric regime Second is the case of an asymmetric network. This has very low synaptic weights to KE from the stochastic pair $g_{stochE} = 0.026, g_{stochI} = 0.0026$, with $\lambda_{E,I}(t)$, oscillating between 0 and 10. The synaptic weights from the deterministic pair are selected so that KE is as close as possible to the spiking threshold in rostral, but not able to cross in the absence of stochastic inputs, $g_{detE} = 0.827, g_{detI} = 0.199$. That is, in rostral $g_{ER} = 0.827$, and in pocket $g_{ER} = 0.026$. The weights from the other populations of interneurons to knee extensor also change between the two rhythms. Therefore, the network is not the same for each rhythm. However, we include this case because it is also capable of generating correct pocket and rostral rhythms. We use $\tau_{KE} = \tau_{HE} = \tau_{HF} = 1$, although the time constants used in the Symmetric case do give reasonable rhythms. Finally, stochastic inhibition plays a relatively weaker role than in the Symmetric, although it is possible to raise its impact and still find successful parameters (see section 3.5.1).

In this section, we presented the architecture we implement, provided a mathematical description of neurons in our model, and described the parameter sets we use in simulations. In the next section, we will present baseline simulations that show our model is capable of producing both the pocket and the rostral scratch rhythms, and that the inclusion of noise in our model improves the quality of rhythms produced.

3.3 NOISE IMPROVES QUALITY OF RHYTHM GENERATION

We show by direct comparison that not only is this model capable of producing the pocket and rostral rhythms, but also that the inclusion of noise improves the quality of such rhythms. Recall, the experimentally derived benchmarks for successful rhythms are:

- HF and HE activate in antiphase and do not receive temporally overlapping excitation and inhibition in pocket. They do receive temporally overlapping excitation and inhibition in rostral, Figure 23.
- KE is activated with HE in pocket. KE is activated with HF with a delay in onset in rostral.

. We no longer require that HE and HF have the relative durations shown in Figure 1. We examine qualitatively different types of noise (homogeneous and inhomogeneous Poisson processes), as well as the effects of removing the stochasticity from the spike trains of the stochastic side.

Symmetric regime Successful examples of the pocket and rostral rhythms can be seen in Figure 26. In subsequent numerical experiments, lower frequency inputs to the motoneurons are considered in order to make the system more amenable to analysis. The effects of frequency are detailed further in section 3.5.3.

Beginning with the pocket rhythm (EP, IP deterministic, ER, IR stochastic, equation (3.3)), the strongly antiphase nature of the interneurons means the deterministic populations dominate the stochastic, and KE displays synchrony with HE with no delays, as desired (Figures 1, 26 top, and 27). Rostral, (ER, IR deterministic, EP, IP stochastic, equation

(3.2)) exhibits more interesting behavior. Recall, the deterministic synaptic weights of $g_{ER} = 0.8, g_{IR} = 0.2$ are not sufficient to elicit firing without additional stochastic inputs. The early spiking (beginning around $t = 600ms$) of EP allows robust, early firing from knee extensor, giving a rostral rhythm with a delay (Figure 28). There is one notable issue in these and subsequent figures: in pocket, HF is active longer than HE; in rostral HE is active longer than HF. This could likely be improved with different modulation of inputs.

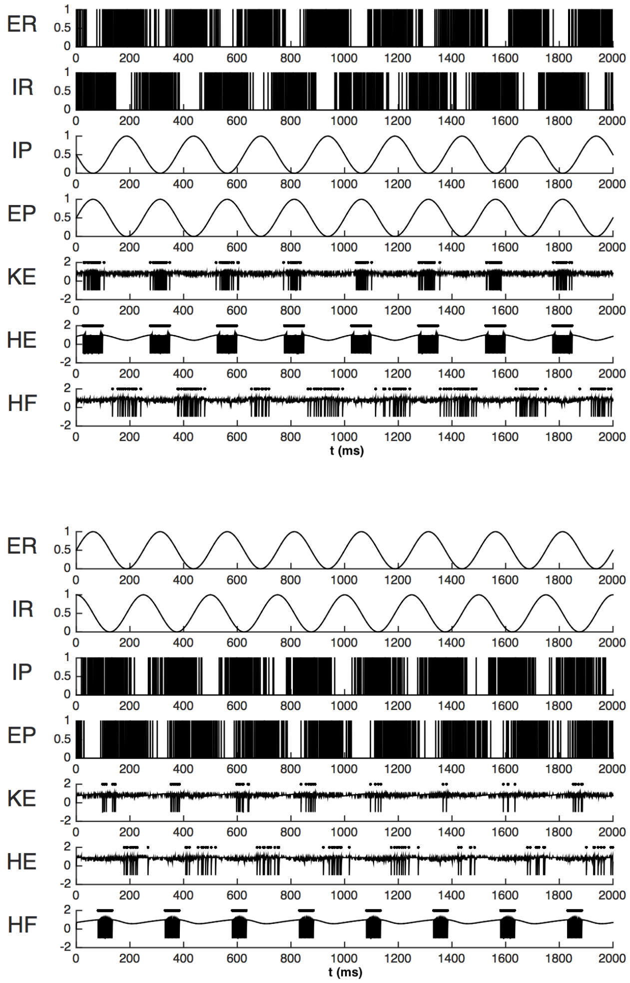

Figure 26: Basic simulation results of equation (3.1) and: equation (3.3) for pocket (top), equation (3.2) for rostral (bottom) with the Symmetric parameter regime. Note that the relative timing and durations of activity in the simulation match the recordings in Figure 1, with the exception of HE and HF relative durations.

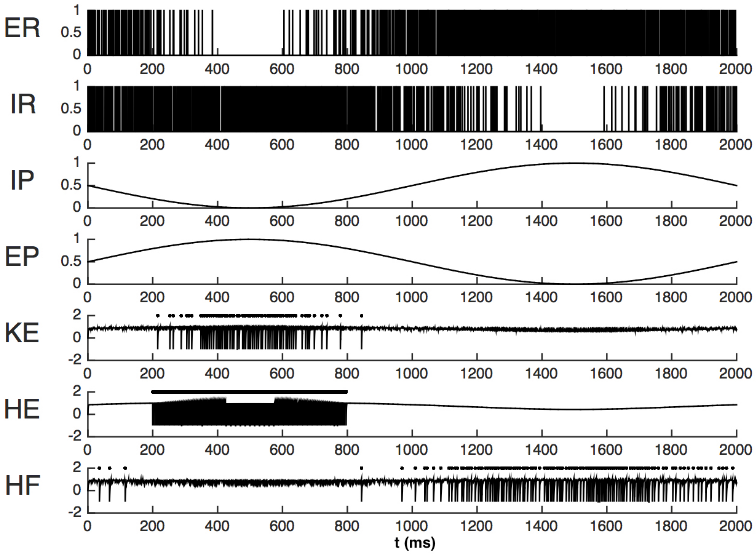

Figure 27: Simulation results of equations (3.1) and: (3.3) for pocket rhythm at a lower frequency than in Figure 26 in the Symmetric parameter regime.

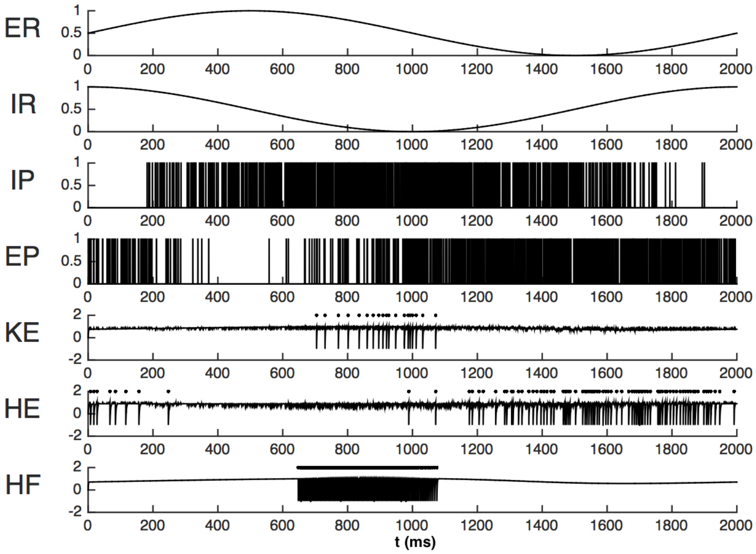

Figure 28: Simulation results of equation (3.1) and (3.2) for rostral rhythm at a lower frequency than in Figure 26 in the Symmetric parameter regime.

Stochasticity plays a key role in the rhythm generation when the motoneurons are modeled as leaky integrate-and-fire neurons rather than as the relaxation oscillators used in Chapter 2. To compare, the inhomogeneous Poisson process generating the stochastic spike trains is replaced with deterministic sinusoidal interspike intervals. In pocket (Figure 29 left), this leads to slightly delayed onset of KE with respect to HE, early termination of KE with respect to HE, and an incredibly short active phase of HF. In rostral (Figure 29 right), this change leads to termination of KE activity early relative to HF, no delay in onset of KE with respect to HF, and an incredibly short active phase of HE. In both rhythms, there is also an undesirably long period of complete motoneuron quiescence between the termination of hip flexor and the start of hip extensor activity.

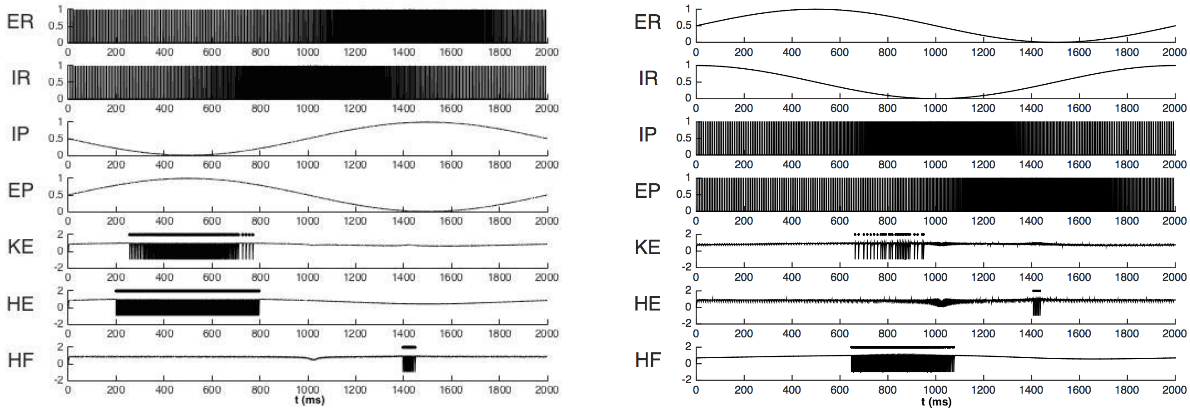

Figure 29: Impact of removing noise from spike trains of stochastic interneuron populations. Simulation results of equation (3.1) and: equation (3.3) for pocket (left), equation (3.2) for rostral (right) in the Symmetric parameter regime. The stochastic interneuron populations in each rhythm have deterministic sinusoidal interspike intervals in this simulation.

We quantify the improvement that the inclusion of noise provides in Figure 30: histograms over 10000 trials for knee extensor activation (left) and termination (right). Figure 30 also includes labels of the times of activation and termination for hip flexor, activation and termination for knee extensor when noise is removed from the spike trains of stochastic interneuron populations (Figure 29, right), and the mean time of knee extensor activation and termination in the presence of noise. The inclusion of noise increases the delay in knee extensor activity relative to hip flexor. More notably, the inclusion of noise causes knee extensor to terminate activity both later and closer to the termination of hip flexor activity.

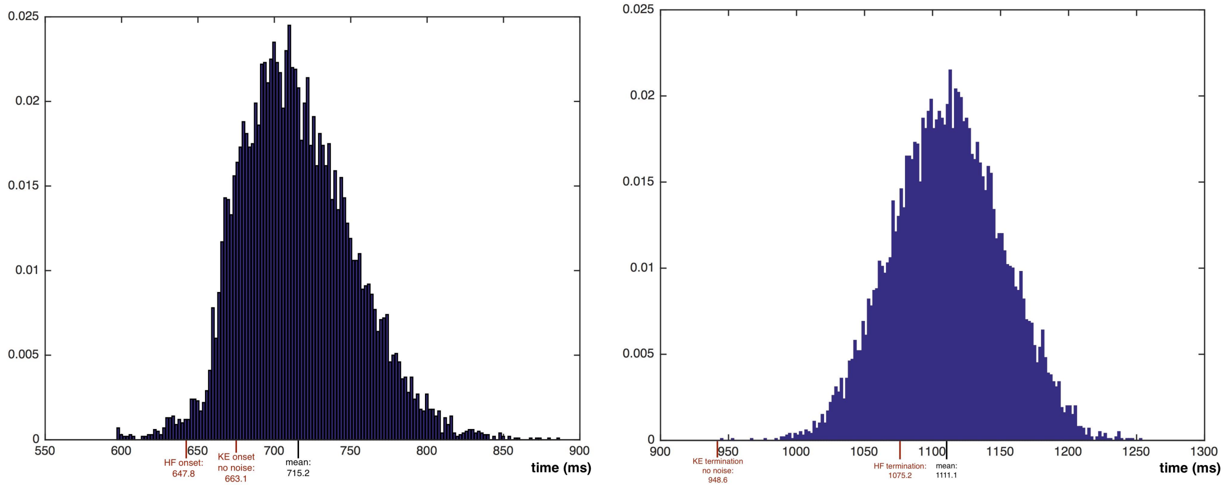

Figure 30: Impact of removing noise from spike trains of stochastic interneuron populations during the rostral rhythm. Left: histogram over 10000 trials for knee extensor activation. The mean activation time of knee extensor is labeled in black. The activation times for hip flexor and for knee extensor when noise is removed from the spike trains of stochastic interneuron populations (Figure 29, right) are labeled in red. Right: histogram over 10000 trials for knee extensor termination. The mean termination time of knee extensor is labeled in black. The termination times for hip flexor and for knee extensor when noise is removed from the spike trains of stochastic interneuron populations (Figure 29, right) are labeled in red.

We also consider the case of completely deterministic inputs: four sine waves with synaptic weights and amplitudes as in the symmetric parameter regime. This case is shown for pocket (top) and rostral (bottom) in Figure 31; note that knee extensor does not fire in either. It is possible to tune the amplitudes of the sine waves and the synaptic weights such that knee extensor fires. However, in these cases, at least one of the hip motoneurons fails to fire. Therefore, it does not appear that strictly deterministic inputs such as these are capable of producing motoneuron rhythms that meet the features of a successful rhythm outlined in Section 3.1.

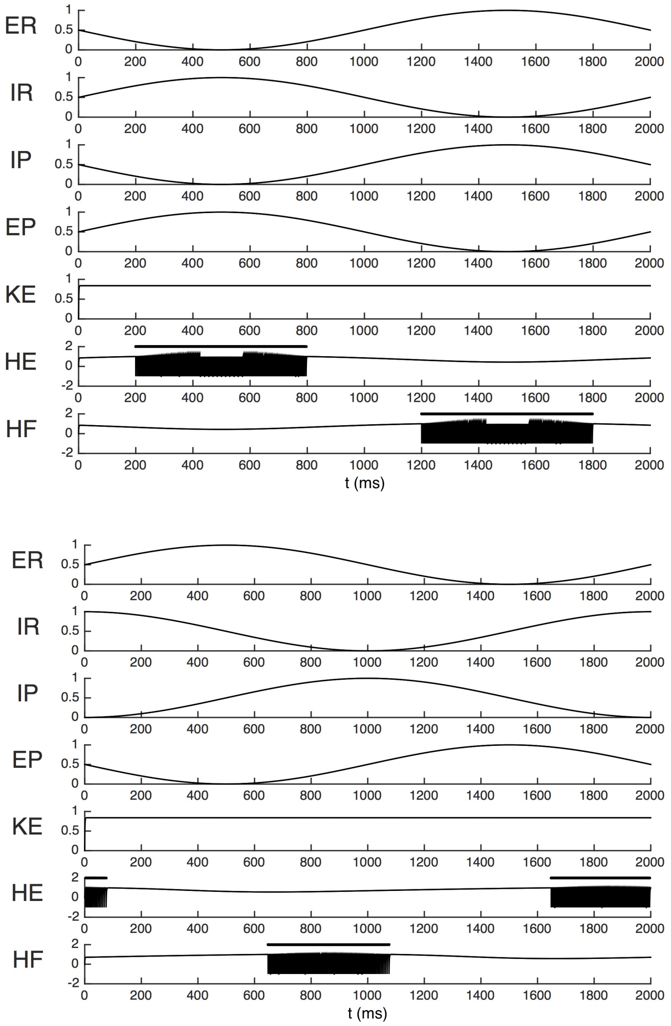

Figure 31: Impact of removing noise from spike trains of stochastic interneuron populations. The stochastic interneuron populations in each rhythm havebeen replaced with strictly deterministic sine waves.

We now consider the case of a step homogeneous Poisson process. In this scenario, the spike rate of the synaptic drive from the stochastic side is switched on from 0 at a set time, after which spikes are generated by a homogeneous Poisson process with constant rate $\lambda_{E,I}(t) = \lambda_{E,I}^{mid}$. In rostral there are only KE spikes once the stochastic excitation (EP) has turned on (Figure 32, left). That is, the deterministic inputs are sufficient to get knee extensor close to the firing threshold, but the step of stochastic excitation is necessary to fire. The delay in onset of knee extensor relative to hip flexor is too long, and the firing of hip extensor is too sparse. Pocket displays both a delay in onset and early termination for knee extensor, making this an undesirable rhythm (Figure 32, right). Similarly to the inhomogeneous Poisson process case, removing noise and modeling the interneurons as spike trains with deterministic interspike intervals fails to generate correct rhythms.

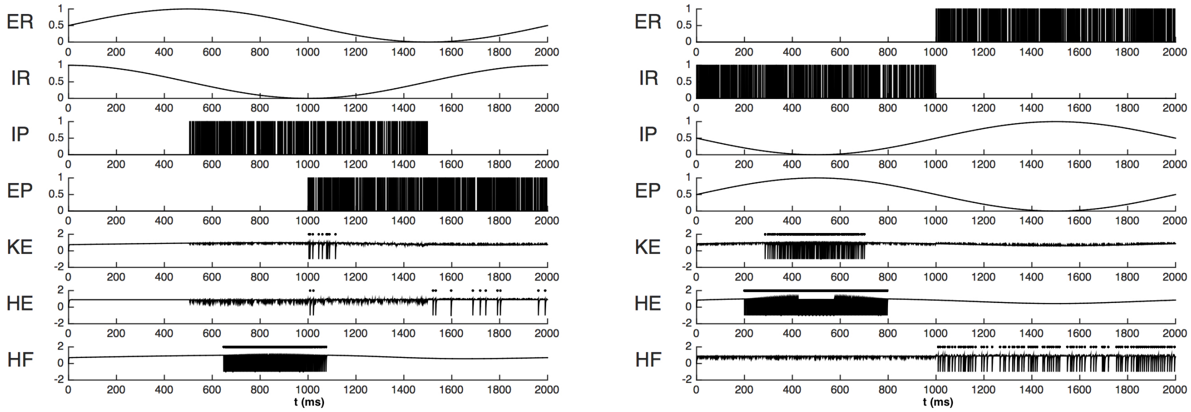

Figure 32: Effect of a step homogeneous Poisson process. Simulation results of equation (3.1) and: equation (3.3) for pocket (left), equation (3.2) for rostral (right) in the Symmetric parameter regime. The stochastic interneuron populations in each rhythm have spike times generated by a homogeneous Poisson process of rate $\lambda_E^{mid}, \lambda_I^{mid}$.

Asymmetric case This case shows that several qualitatively different regimes of interneuron output can produce the rhythms without having to adjust ϕ. Hence, it is the general features of the interneuron outputs that lead to rhythm generation, rather than a special set of parameters. Specifically, it is the relative phase of the outputs ϕ that dictates rhythm selection.

As in the symmetric network case, inhomogeneous Poisson processes lead to the most successful pocket and rostral rhythms, Figure 33. In pocket (top), the durations of HE and KE are shorter and the duration of HF is longer in this case than in the Symmetric case. In rostral (bottom), the durations of HF and KE are shorter and the duration of HE is longer in this case than in the Symmetric case. Both of these impacts are due to the higher values achieved by $\lambda_I(t)$ in the Asymmetric case.

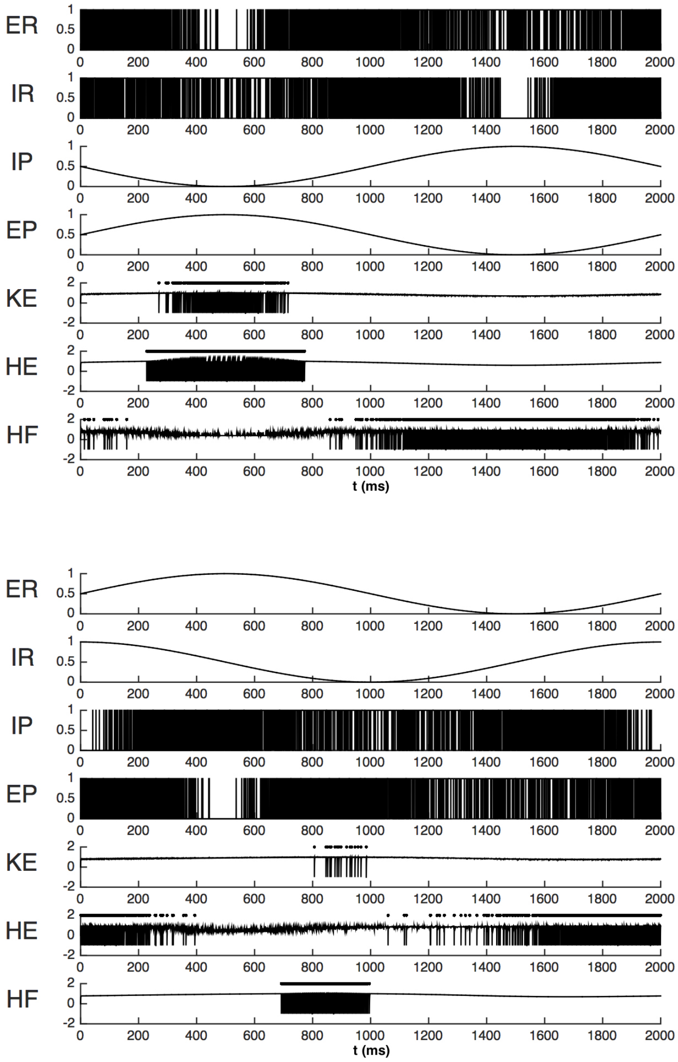

Figure 33: Basic simulation results of equation (3.1) and: equation (3.3) for pocket (top), equation (3.2) for rostral (bottom) with the Asymmetric parameter regime. Note that the relative timing and durations of activity in the simulation match the recordings in Figure 1 with the exception of HE and HF relative durations.

Replacing the inhomogeneous Poisson process generating the stochastic spike trains with simply sinusoidal interspike intervals (with no noise) leads to failures similar to those observed in the Symmetric case. Step homogeneous Poisson processes are more successful in the asymmetric network case than they were in the symmetric case. However, there are still issues with the rhythms generated: undesirably long periods of total motoneuron quiescence and the activity of knee extensor is shortened too much.

In this section, we presented baseline simulations that show our model is capable of producing both the pocket and the rostral scratch rhythms, and that the inclusion of noise in this spiking model improves the quality of rhythms produced. The choice of the spiking model used in this chapter, rather than the relaxation oscillator model used in Chapter 2, allows the investigation of experimental results that the relaxation oscillator model was ill-suited for, such as those depicted in Figures 22 and 23. In the next section, we will analyze our model's capability of reproducing the results depicted in Figure 22, and we will explore biological explanations for our findings.

3.4 PREDICTIONS

The rhythmic modulation of motoneurons results shown in Figure 22 were a key part of our choice to implement a stochastic spiking model. Recall, research performed by Berkowitz and Stein [5] found that motoneurons display a lower firing rate in response to inputs with greater rhythmic modulation. They proposed two different reasons for this result:

(E1) The activity of the observed neurons had saturated at peak firing rate and additional rhythmic depolarization would not affect the firing rate.

(E2) Rhythmic inhibition is more important than rhythmic excitation in generating the turtle scratch rhythms and thus whenever a motoneuron receives 'a greater proportion of inhibition, it fires at a lower rate but with stronger rhythmic modulation.'

Our results to this point have had $\lambda_E^{mid} = \lambda_I^{mid}$, equal modulation of excitation and inhibition.

We investigate (E1) as a possible explanation by increasing λ_E^{mid} while $\lambda_I^{mid} = 0.5$ remains fixed. As λ_E^{mid} varies, we average over 1000 trials to calculate both the active duration and the average firing rate while active for knee extensor and the hip motoneurons in each of pocket and rostral. The results for knee extensor in rostral are shown in Figure 34 (top). The firing rate increases without saturating. The same behavior is observed for both hip motoneurons in rostral and in pocket. By $\lambda_E^{mid} = 1.5$ the rhythm is no longer successful, shown in Figure 34 (bottom): KE activates before HF rather than with a delay, KE terminates after HF terminates, and HE activates during HF's active phase rather than in antiphase. Therefore, (E1) is not supported by this model: as λ_E^{mid} is increased, the model produces rhythms that do not meet all of the features required for success (outlined in Section 3.1) before firing rates saturate. This lack of saturation is a prediction of the model as it is posed here.

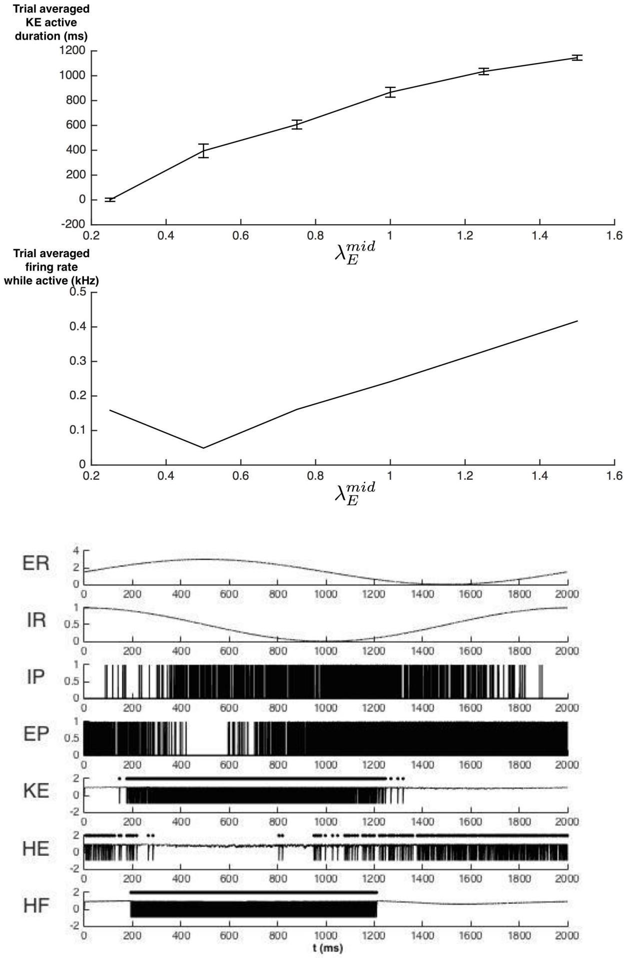

Figure 34: Impact of varying excitatory modulation on knee extensor in rostral. Top: Changes in knee extensor active duration as λ_E^{mid} is increased, averaged over 1000 trials. Middle: Average firing rate of knee extensor while active as λ_E^{mid} is increased, averaged over 1000 trials. Note that the firing rate does not saturate. Bottom: A simulation of the rostral rhythm with $\lambda_E^{mid} = 1.5$.

We examine (E2), the impact of a motoneuron receiving a greater proportion of inhibition than of excitation, in the same way. λ_I^{mid} is increased while $\lambda_E^{mid} = 0.5$ remains fixed. We again measure active duration and average firing rate while active for each motoneuron, each averaged over 1000 trials. The results for knee extensor in rostral are shown in Figure 35 (top). The results for all other cases are qualitatively similar. As λ_I^{mid} increases, the active duration and average firing rate both decrease as they did in experiment, Figure 22. We also show activity traces for rostral in the original $\lambda_I^{mid} = \lambda_E^{mid} = 0.5$ case and for $\lambda_I^{mid} = 1, \lambda_E^{mid} = 0.5$ in Figure 35 (bottom left and right, respectively) to further illustrate this phenomena. Therefore, we find that explanation (E2) is the one supported by this work: rhythmic inhibition is more important than rhythmic excitation in generating the turtle scratch rhythms. Berkowitz and Stein [5] also hypothesized that explanation (E2) was more likely than explanation (E1) to cause the results in Figure 22. That is, we predict that whenever a motoneuron receives a greater proportion of inhibition, it should fire at a lower rate but with stronger rhythmic modulation, and that whenever a motoneuron receives additional rhythmic depolarization, its firing rate should increase. This could be further verified with intracellular recordings.

In this section, we showed our model was capable of reproducing the results depicted in Figure 22, and we explored biological explanations for our findings. In the next section, we will explore how different parameters in the model affect rhythm generation.

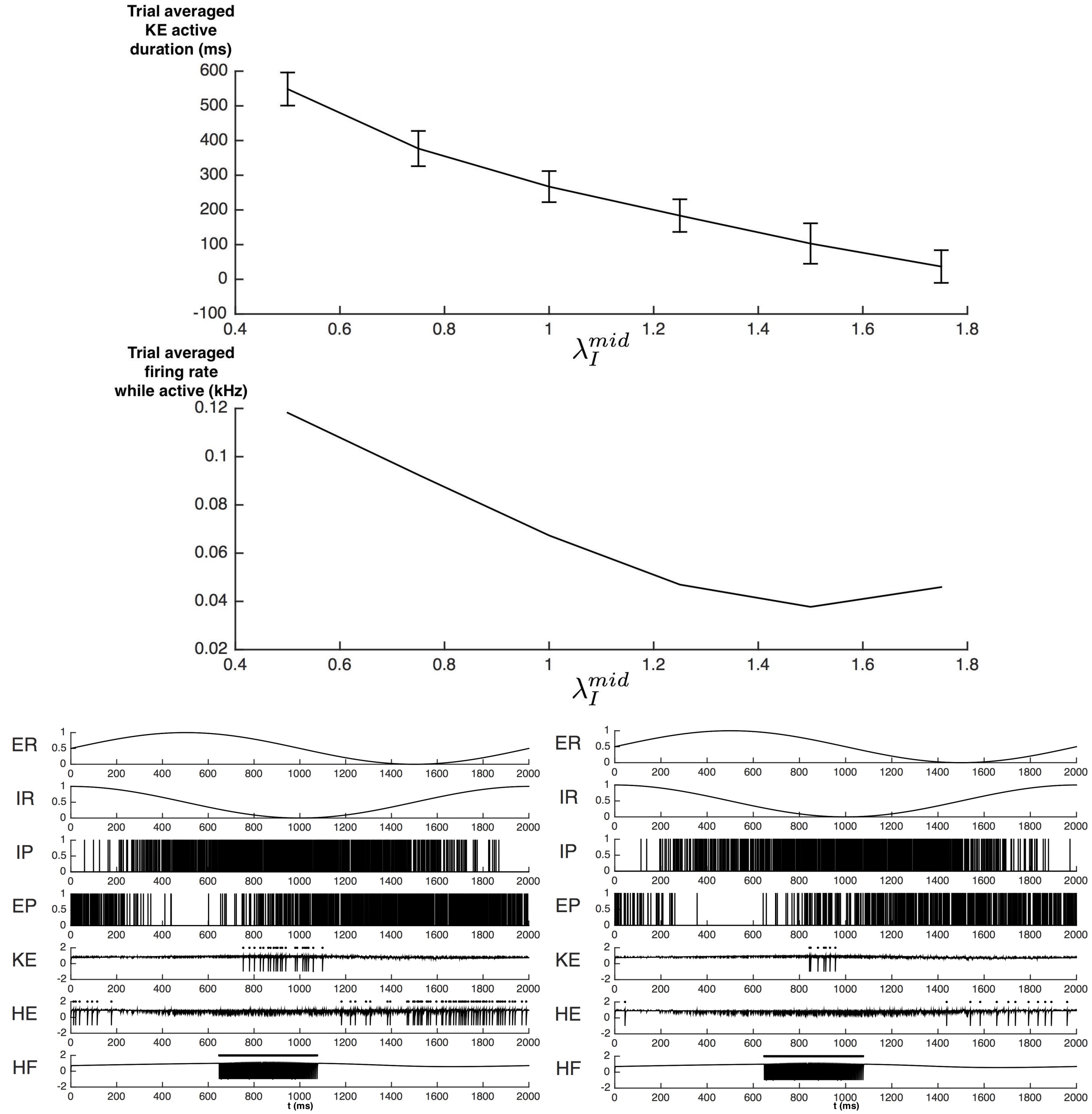

Figure 35: Impact of varying inhibitory modulation on knee extensor in rostral. Top: Changes in knee extensor active duration as λ_I^{mid} is increased, averaged over 1000 trials. Middle: Average firing rate of knee extensor while active as λ_I^{mid} is increased, averaged over 1000 trials. Bottom left: Simulation of the rostral rhythm with original $\lambda_E^{mid} = \lambda_I^{mid} 0.5$. Bottom right: Simulation of the rostral rhythm for $\lambda_I^{mid} = 1, \lambda_E^{mid} = 0.5$ demonstrating the decrease in firing rate and increase in modulation of motoneurons.

3.5 ADDITIONAL PARAMETER EXPLORATIONS

In this section, we perform a systematic but non-exhaustive computational exploration of the impact of different model parameters. First, we examine the interaction of stochastic synaptic weights and arrival rates to achieve successful rhythms. Second, we examine the role of phase shift ϕ in rhythm selection. Finally, we consider the role of input signal frequency on rhythm success.

3.5.1 KE on/off behavior as function of synaptic weights and rate

Because rostral is the more challenging rhythm to achieve, we have used it as the standard to select parameters throughout this chapter and the previous chapter. Therefore, our exploration here is restricted to the rostral case. We find that relatively stronger inhibition (as seen in the Symmetric regime compared to the Asymmetric) greatly restricts the rates of stochastic spike arrivals that allow for successful rostral rhythms.

We make three basic assumptions:

1. the ratio of g_{EP} to g_{IP} will be fixed as g_{EP} is varied. We consider $g_{IP} = g_{EP}/4$ (as used in the Symmetric regime) and $g_{IP} = g_{EP}/10$ (as used in the Asymmetric regime).
2. the modulation of stochastic excitation and inhibition will be the same as λ_E^{max} is varied: $\lambda_E^{max} = \lambda_I^{max}$.
3. $g_{ER} = 0.8, g_{IR} = 0.2$ throughout.

We construct a chart detailing where knee extensor correctly activates and terminates in the rostral rhythm based on simulations as λ_E^{mid} and g_{EP} vary. Details of the construction are provided in Section 3.7.1. We identify five ways in which knee extensor may fail to activate and terminate at the correct time:

(F1) knee extensor may activate too early in the active phase of hip flexor.
(F2) knee extensor may activate too late in the active phase of hip flexor.
(F3) knee extensor may terminate too early relative to hip flexor.
(F4) knee extensor may terminate too late relative to hip flexor.
(F5) knee extensor may fire too sparsely for the rhythm to be reasonable.

The simulation based chart is shown in Figure 36 for the Symmetric regime (left) and the Asymmetric regime (right). In each parameter regime, at larger values of $\lambda_E^{mid} = \lambda_I^{mid}$ (e.g. $\lambda_E^{mid} = 5$ in the Symmetric regime and $\lambda_E^{mid} = 10$ in the Asymmetric regime), increasingly large values of g_{EP} are necessary for a successful rhythm. We hypothesize that this is due to the peak of stochastic inhibition occurring in rostral, and excitatory spikes needing to have more strength to compensate for the more frequent arrivals of inhibitory spikes. This is, again, consistent with explanation (E2) of the modulation results shown in Section 3.4, Figures 22 and 35: inhibition matters more than excitation in turtle scratch rhythm generation. We find that in the weaker inhibition case (right), successful rhythms are possible at a wider range of λ_E^{mid} than seen in the stronger inhibition case (left). This is an additional area of exploration possible in intracellular recordings: the maximum modulation of excitatory and inhibitory inputs to motoneurons at which rhythms are successful may lead to insights about the relative strength of excitation versus inhibition.

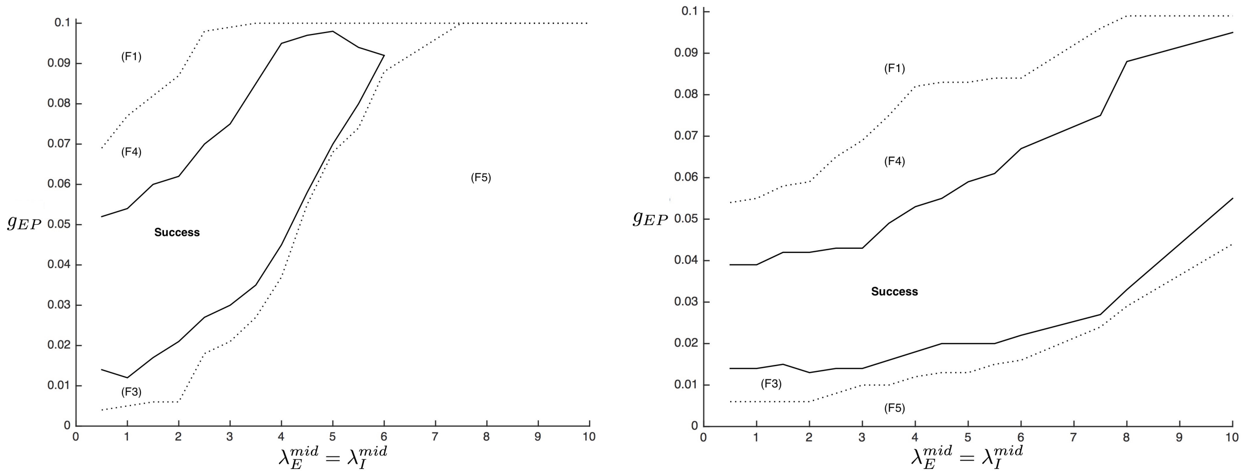

Figure 36: Simulation based regions of successful rhythm generation as g_{EP} and λ_E^{mid} vary. Common failure types in other regions are given as well. Left: Regions for $g_{IP} = g_{EP}/4$ (Symmetric case). Right: Regions for $g_{IP} = g_{EP}/10$ (Asymmetric case). Only the weaker inhibition case (bottom) is capable of producing successful rhythms at large values of λ_E^{mid}.

A similar chart based on firing rate theory can be constructed for each case. This theoretical chart is constructed in several steps (details in Sections 3.7.3 and 3.7.2) and shown in Figure 37. Many qualitative features are shared between theory and simulation in the $g_{IP} = g_{EP}/4$ case (Figures 37, 36 top): there are no successful rostral rhythms at higher values of λ_E^{mid} and the successful region is steeply increasing in g_{EP} for increasing λ_E^{mid}. The general shape of the successful region is very similar between theory and simulation, with theory appearing to compress the region from simulation to smaller values of both g_{EP} and λ_E^{mid}. There is less agreement between theory and simulation in the $g_{IP} = g_{EP}/10$ case (Figures 37, 36 bottom).

The theory does not see the dramatic increase in g_{EP} needed for success at high values of λ_E^{max} seen in simulation. We hypothesize that compensating for inhibition is the cause of this increase. We verify this hypothesis by increasing the role of inhibition in the calculations using theory. Interestingly, simply increasing λ_I when λ_E is fixed (breaking assumption 2 above, and increasing the proportion of inhibition received by a motoneuron as explored in Section 3.4), only introduces the increase in the upper boundary of the successful rostral region. In order to see both the upper and lower boundaries increase, g_{IP} must be increased (breaking assumption 1). That is, it is not sufficient for inhibitory spikes to arrive more frequently, they must also be stronger individual spikes. This once again supports the hypothesis that rhythmic inhibition is more important than rhythmic excitation in successfully generating turtle scratching rhythms.

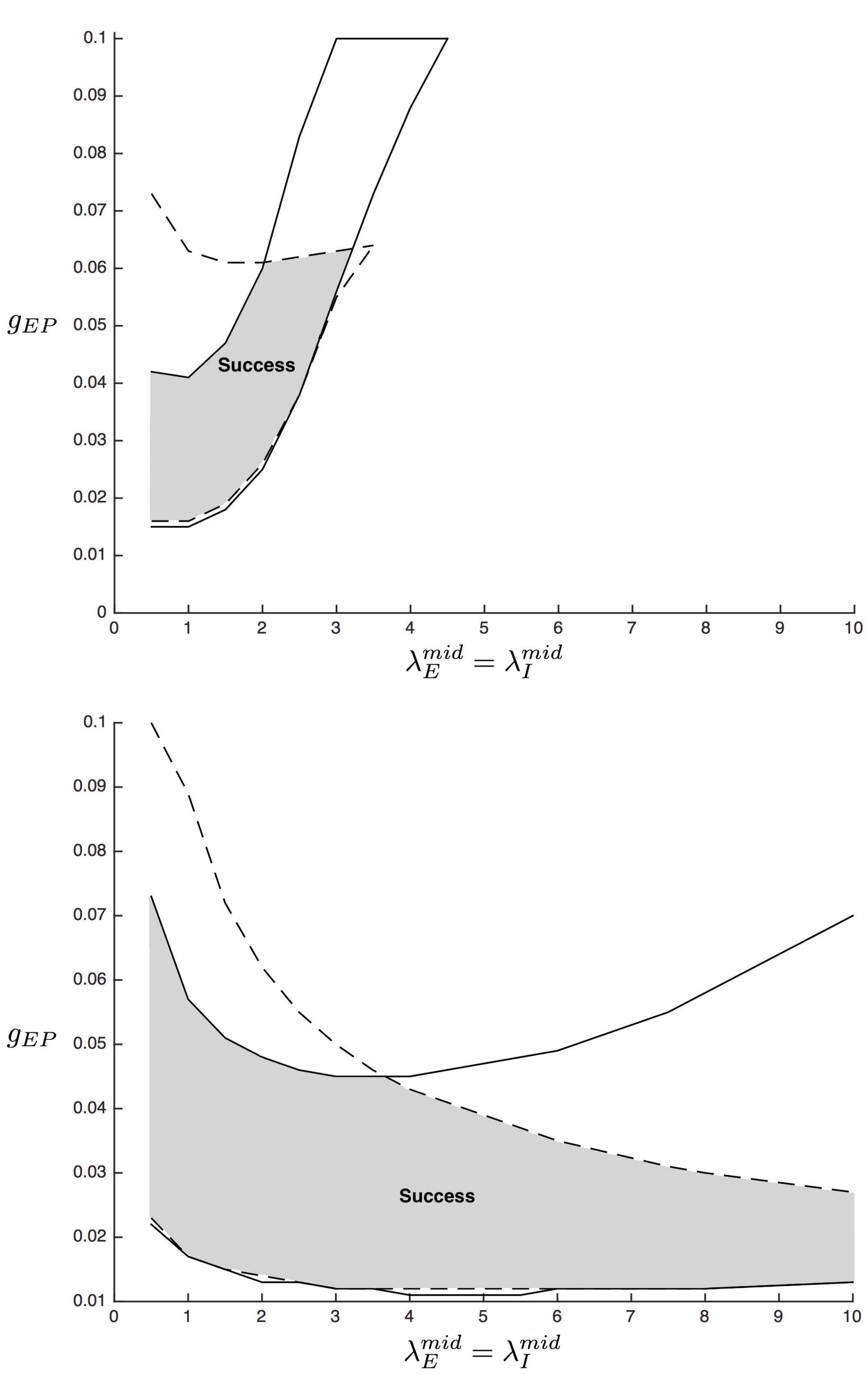

Figure 37: Theory based regions of successful rhythm generation as g_{EP} and λ_E^{mid} vary. Top: Region of success for $g_{IP} = g_{EP}/4$ (Symmetric case). This region is a reasonable qualitative match for the region found by simulation, in Figure 36. Bottom: Regions for $g_{IP} = g_{EP}/10$ (Asymmetric case). This case does not agree as closely with the region found by simulation, in Figure 36. Again, only the weaker inhibition case (bottom) is capable of producing successful rhythms at large values of λ_E^{mid}.

Finally, there are qualitatively different phenomena observed outside of this region in parameter space. As g_{EP} is increased beyond 0.1, knee extensor undergoes a period of behavior with two peaks of activity, Figure 38, top. The second peak is earlier and due to the additional input from EP. The termination between the peaks comes from the cessation of EP activity. Increasing g_{EP} further leads to the stochastic inputs overwhelming knee extensor, Figure 38, bottom.

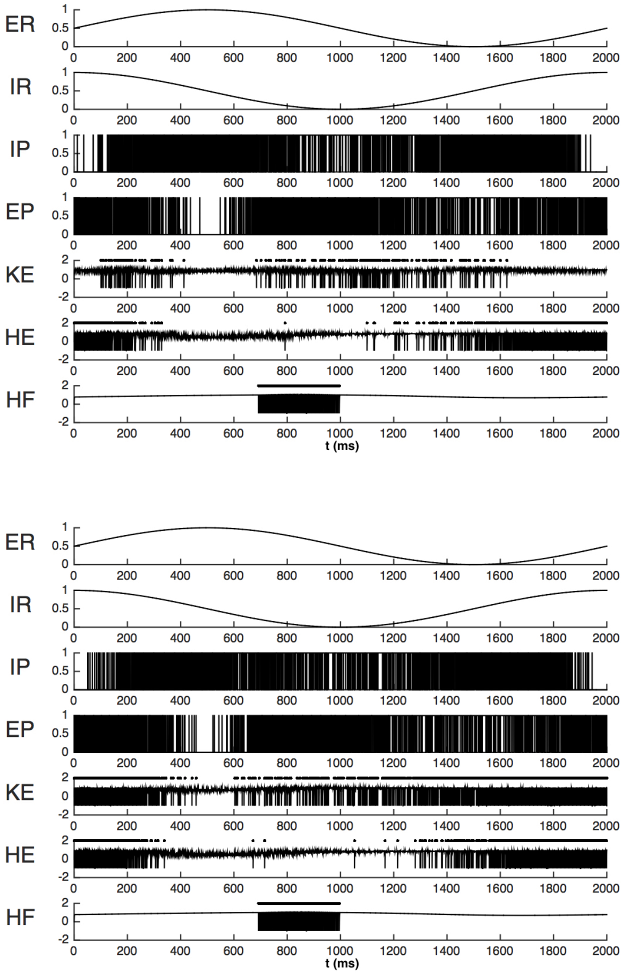

Figure 38: Impact of large excitatory spikes. In the rostral case with Symmetric parameter regime, g_{EP} is increased to $g_{EP} = 0.2$ (top) and $g_{EP} = 0.4$ (bottom). All other parameters remain as described in Section 3.2. In particular, g_{IP} remains proportionally to $g_{IP} = g_{EP}/4$. Similar results are seen in the Asymmetric regime.

In this section, we examined the impact of changing stochastic synaptic weights and the arrival rate of stochastic spikes on the on/off behavior of knee extensor. In the next section, we will examine the role of varying ϕ in rhythm selection.

3.5.2 Examination of phase shift ϕ in rhythm selection

For a fixed set of synaptic weights (e.g. the Symmetric regime), the rostral delay lasts for shifts of $\phi = \pi/3$ to $\phi = 0.8\pi$. Pocket requires ϕ between 0.8π and π.

For $g_{ER} = 0.8, g_{IR} = g_{ER}/4$, the weights used until now, knee extensor can fire in the absence of any stochastic input ($g_{EP} = g_{IP} = 0$) for $\phi = 3\pi/4$ for a rostral rhythm, Figure 39, top. There are issues with the pattern (early termination of knee extensor). Including noise symmetrically ($g_{EP} = 0.8, g_{IP} = g_{EP}/4$), gives the correct rhythm, Figure 39, bottom. Therefore, noise still plays a key role in rhythm generation even in regimes where deterministically-driven spiking is possible. Overall, as ϕ is decreased from 0.8π to $\pi/3$, knee extensor experiences both a greater delay in onset relative to hip flexor and decreasing firing rate.

For shifts $\phi < \pi/3$, qualitatively different behavior begins to emerge. We consider specifically the case of concurrent excitation and inhibition to all motoneuron populations [3]: $\phi = 0.1$. In general, knee extensor synchronizes with stochastic excitation rather than deterministic, because the phase shift between deterministic excitation and inhibition is small enough that the inputs essentially cancel each other. The Asymmetric case ($g_{DetE} = 0.827, g_{DetI} = 0.199, g_{StochI} = 0.0026$) is shown in Figure 40. More spiking is seen as the excitatory stochastic synaptic weight is increased, while the synaptic inhibition remains fixed, Figure 40 top to bottom. Note that the deterministic hip population is not firing, due to the cancellation of deterministic excitation and inhibition. This behavior holds as ϕ is increased, gradually breaking down until approximately $\phi = \pi/3$, at which point knee extensor synchrony is primarily with deterministic excitation.

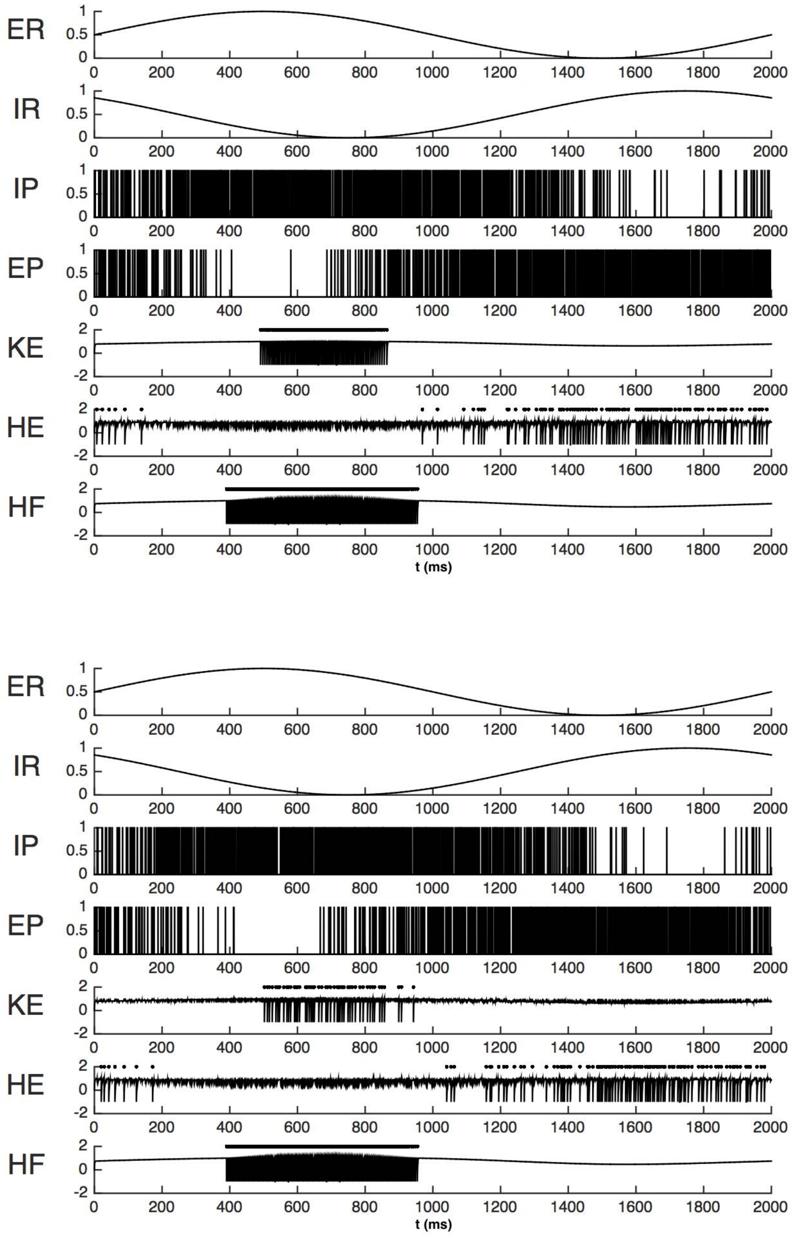

Figure 39: Impact of noise in regime where deterministically driven spiking is possible, $\phi = 3\pi/4$ in the Symmetric regime. Top: Only deterministic inputs to knee extensor are included, $g_{EP} = g_{IP} = 0$. Bottom: Stochastic inputs to knee extensor are included.The additional input improve the rostral rhythm, indicating knee extensor does require input from all four interneurons.

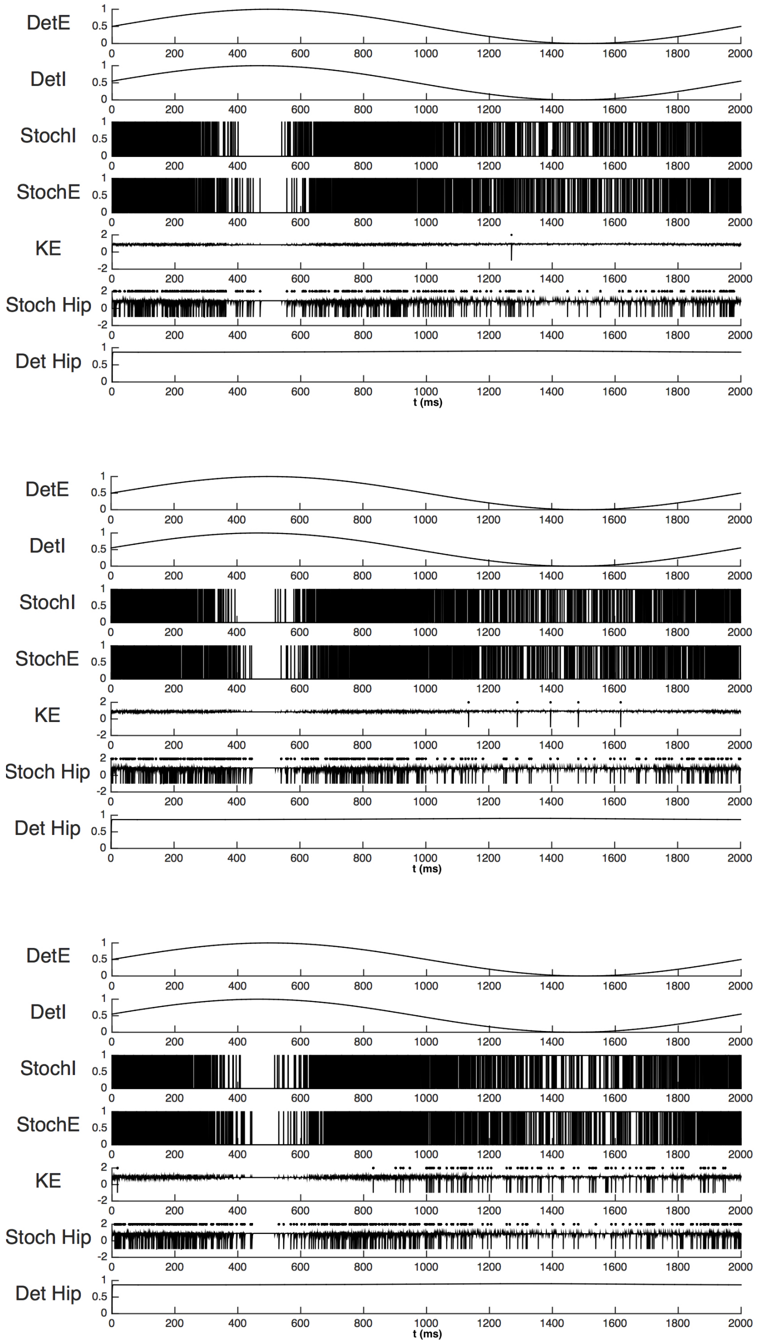

Figure 40: Effects of in phase stimuli, $\phi = 0.1$. We replace our previous neuron population labeling in this figure: StochE and StochI (DetE and DetI) are the excitatory and inhibitory stochastic (deterministic) interneuron populations. Stoch Hip (Det Hip) receives only these as inputs. KE still receives inputs from all four interneuron populations. Top: $g_{StochE} = 0.07$ instead of 0.026 to get spiking, $g_{DetE} = 0.827$. Middle: Only g_{StochE} is increased, to $g_{StochE} = 0.09$. Bottom: Only g_{StochE} is increased, to $g_{StochE} = 0.14$.

In this section, we examined the role of varying ϕ in rhythm selection. In the next section, we will investigate the range of frequencies that may generate successful rhythms.

3.5.3 Frequency of stimulus

The frequency of the inputs to knee extensor may be increased by several factors and the rhythms are maintained. This is shown for rostral rhythms in Figure 41, and is true in pocket rhythms as well. However, once the input signals to knee extensor become sufficiently fast, the likelihood of several stochastic inhibitory spikes occurring in quick succession increases. These blocks of inhibition can keep knee extensor from activating, and cycles of KE activity begin to be lost (Figure 42, red circles). While this is certainly explainable from a numerical point of view, it may also prove useful in understanding the knee extensor deletion variation of rostral scratch [61, 62].

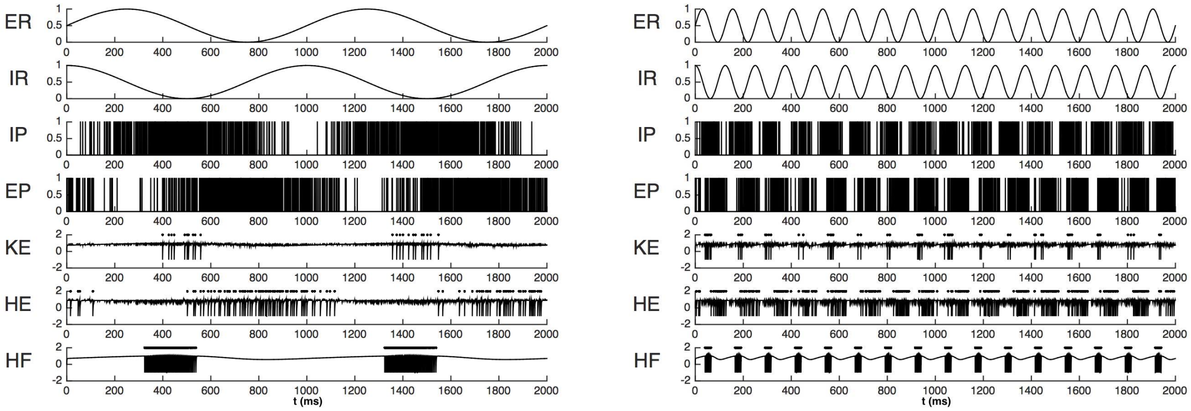

Figure 41: Increasing frequency of input signals. Left: two periods in two seconds. Right: sixteen periods in two seconds. In each, the relative timing and durations of activity in the simulation match the recordings in Figure 1, with the exception of HE and HF relative durations.

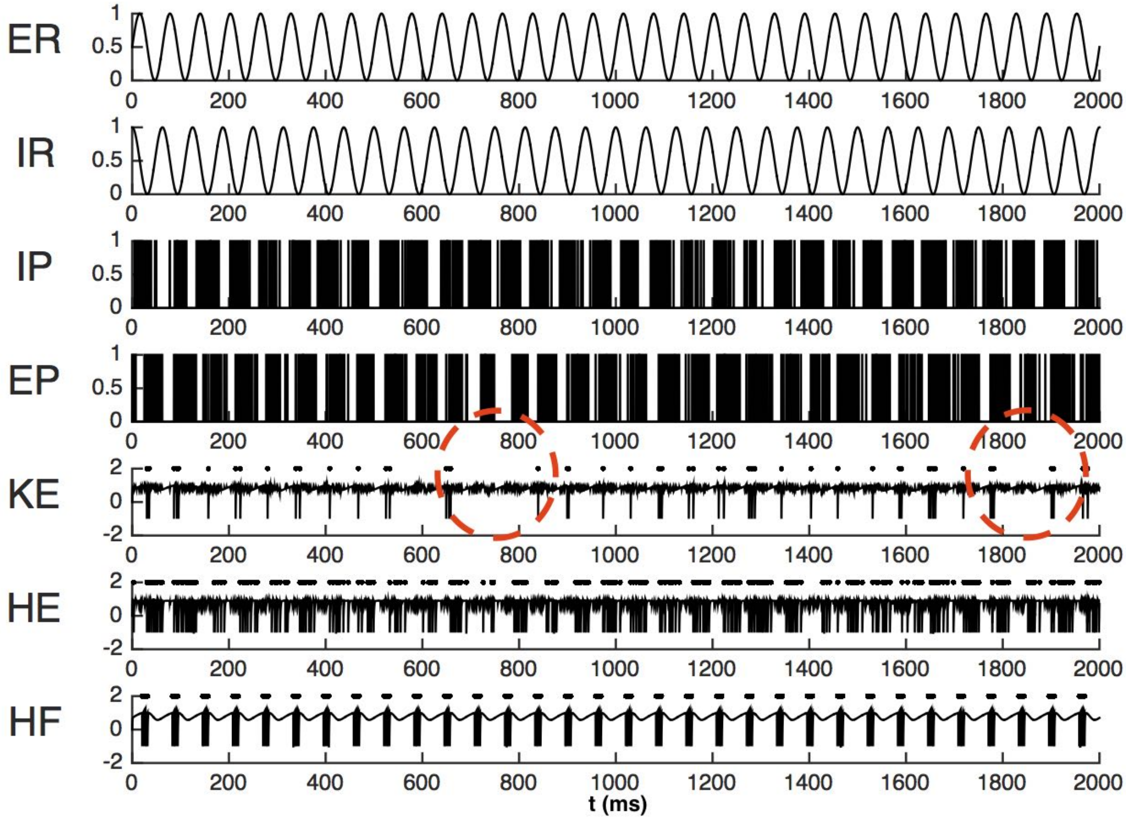

Figure 42: Thirty-two periods in two seconds. Cycles of knee extensor activity are lost at sufficiently high frequency, as indicated in the red circles.

3.6 DISCUSSION

Our motivation for a second model of the turtle system was to explain results not well-handled by the model in Chapter 2, namely results relating to changes in firing rate of the motoneurons [5] and the experimental observation of temporally overlapping excitatory and inhibitory inputs to motoneurons during rostral scratching [51]. We introduced a stochastic spiking model, and, because we omitted the connections at the interneuron level, we were able to consider a model that is more directly testable by intracellular recordings of motoneurons.

We demonstrated that noise improved the quality of rhythm generation in our model, in a variety of distinct parameter regimes. We showed that it is possible to generate both the rostral rhythm with non-antiphase relations among interneuron inputs and the pocket rhythm with antiphase relations among the interneuron inputs from the same network. We then used this successful model to investigate two experimentally proposed [5] explanations for motoneurons displaying a lower firing rate in the presence of inputs with greater rhythmic modulation. Our analysis supported the explanation that Berkowitz and Stein seemed to find more plausible in their paper [5] - that inhibition matters more than excitation in rhythm generation. We also performed a systematic (though non-exhaustive) computational exploration of the impact of different model parameters. By examining the interaction of stochastic synaptic weights and arrival rates, we were able to further support our hypothesis that inhibition matters more than excitation. We also found that it was possible to produce successful pocket and rostral rhythms over a range of phase relations and several factors of input frequencies.

To fully model the network underlying turtle scratching with all observed behaviors requires significantly more populations of neurons than we considered in Chapters 2 and 3. As was the case with our model in the previous chapter, this spiking approach cannot correctly reproduce behaviors seen during hip extensor deletions in rostral scratch. At very high frequency inputs, knee extensor begins to undergo deletions while hip extensor and hip flexor continue to burst in antiphase. This has been observed in experiments [65], although without a knee flexor population it is difficult to assert that this is a true knee extensor deletion. To continue bursting during a hip extensor deletions in rostral, KE would either have to be intrinsically rhythmogenic, as was found in some extensor populations in mice [30], or KE would have to receive inputs from populations not considered in this model. More recent experimental work has included recordings from knee flexor motoneurons, in addition to the three populations considered here. These findings suggest more complex architectures akin to the Unit-Burst-Generator Model [63, 64, 65]. We have, however, shown that a hip-dominated architecture can account for the relative durations and timing of motoneuron activity in pocket and rostral scratching.

3.7 METHODS

3.7.1 Construction of simulation based success chart

In order to characterize the relationship between the synaptic weights of the stochastic spike trains and the amplitude of the sine wave driving the process generating those trains, it is necessary to approach the many parameters in this system in an organized way. Therefore, restricting to the rostral case, the following assumptions are made:

1. the ratio of g_{EP} to g_{IP} will be fixed as g_{EP} is varied. We consider $g_{IP} = g_{EP}/4$ (as used in the Symmetric regime) and $g_{IP} = g_{EP}/10$ (as used in the Asymmetric regime).
2. the modulation of stochastic excitation and inhibition will be the same as λ_E^{max} is varied: $\lambda_E^{max} = \lambda_I^{max}$.
3. $g_{ER} = 0.8, g_{IR} = 0.2$ throughout.

Therefore the times at which HF activity begins (t_{HF}^{on}) and ends (t_{HF}^{off}) are fixed, since hip flexor only receives these deterministic inputs during rostral. With these times for reference, we define acceptable windows in which knee extensor may begin to fire, $[t_{min}^{on}, t_{max}^{on}]$, and in which knee extensor must cease firing, $[t_{min}^{off}, t_{max}^{off}]$. Figure 36 is then constructed by varying λ_E^{mid} and g_{EP} and examining whether or not a rhythm is falling successfully within these windows. There are several core ways in which a rhythm can fail:

(F1) knee extensor may activate too early in the active phase of hip flexor: $t_{min}^{on} \le t_{HF}^{on} + \tau_1$, for some acceptable minimum delay τ_1.

(F2) knee extensor may activate too late in the active phase of hip flexor: $t_{max}^{on} \ge t_{HF}^{on} + \tau_2$, for some acceptable maximum delay τ_2.

(F3) knee extensor may terminate too early relative to hip flexor: $t_{min}^{off} \le t_{HF}^{off} - \tau_3$.

(F4) knee extensor may terminate too late relative to hip flexor: $t_{max}^{off} \ge t_{HF}^{off} + \tau_4$.

(F5) knee extensor may fire too sparsely for the rhythm to be reasonable.

The inclusion of τ's accounts for the fact that, in practice, there is of course some variability trial to trial in the times at which knee extensor begins and ends, but that overall the rhythm is qualitatively correct.

3.7.2 Construction of theory success chart

Analytically, stochastic synaptic weight and amplitude of stochastic rate both appear in the calculation of theoretical firing rate estimates in Section 3.7.3, equations (3.4)-(3.6). Therefore, these firing rate estimates will be the primary criteria used in the construction of a theoretical chart similar to the simulation based chart.

For a fixed $t_{KE}^{on} \in [t_{min}^{on}, t_{max}^{on}]$, λ_E can be fixed, and g_{EP} can be varied to find the minimum value $g_{EP}^{min}(\lambda_E; on)$ and maximum value $g_{EP}^{max}(\lambda_E; on)$ for which knee extensor can begin firing at this specific t_{KE}^{on}. To do so, we return to our homogeneous approximations described in Section 3.7.3, Figure 46. A small window is taken before t_{KE}^{on}, and a small window is taken after. The steady state firing rate, r_0 is calculated in each window for varying g_{EP}, and the smallest value of g_{EP} for which $r_0 \leq r_{min}$ kHz in the first window and $r_0 > r_{min}$ kHz in the second is $g_{EP}^{min}(\lambda_E; on)$. The largest value of g_{EP} for which this holds is $g_{EP}^{max}(\lambda_E; on)$. The region constructed by this method for a particular t_{KE}^{on} is shown in Figure 43. The figures that follow are for $r_{min} = 0$. Figure 37 in Section 3.5.1 uses the criteria of $r_{min} = 0.02$ kHz due to our findings in Section 3.7.3. However, the construction of the figures are the same.

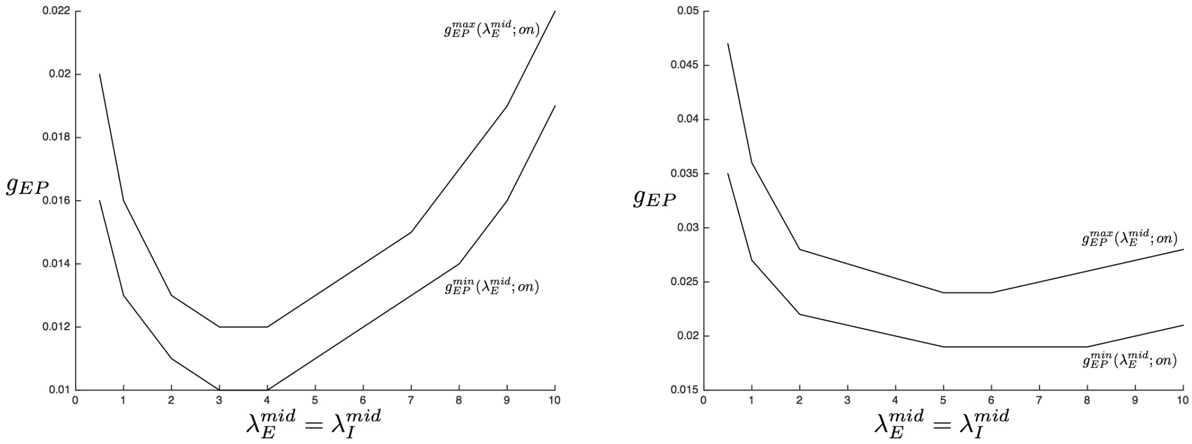

Figure 43: The curves $g_{EP}^{min}(\lambda_E; on)$ and $g_{EP}^{max}(\lambda_E; on)$, defining a region in $\lambda_E - g_{EP}$ space where knee extensor activates as desired, are shown for the cases: $g_{IP} = g_{EP}/4$ (Left) and $g_{IP} = g_{EP}/10$ (Right).

For a fixed $t_{KE}^{off} \in [t_{min}^{off}, t_{max}^{off}]$, a similar $\lambda_E - g_{EP}$ region of successful termination can be generated. For a particular t_{KE}^{off}, such a region is shown in Figure 44.

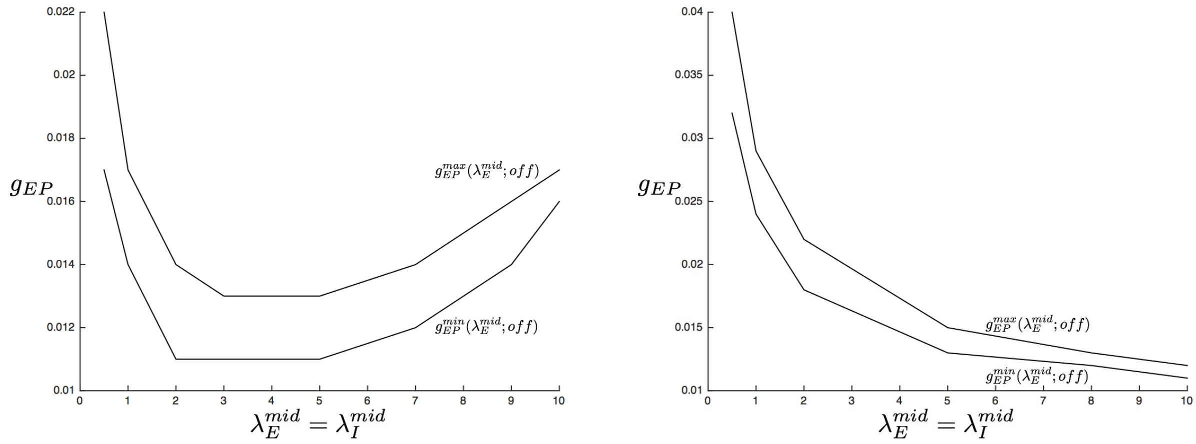

Figure 44: The curves $g_{EP}^{min}(\lambda_E; off)$ and $g_{EP}^{max}(\lambda_E; off)$, defining a region in $\lambda_E - g_{EP}$ space where knee extensor terminates as desired, are shown for the cases: $g_{IP} = g_{EP}/4$ (Left) and $g_{IP} = g_{EP}/10$ (Right).

By ranging over the interval $[t_{min}^{on}, t_{max}^{on}]$ and taking the ensemble of successful onset regions, a new $\lambda_E - g_{EP}$ region can be constructed for any $t_{KE}^{on} \in [t_{min}^{on}, t_{max}^{on}]$. The upper boundary of this region is the curve $g_{EP}^{max}(\lambda_E; on)$ generated for t_{min}^{on}, and the lower boundary is $g_{EP}^{min}(\lambda_E; on)$ generated for t_{max}^{on} (solid lines in Figure 45). Then, any (λ_E, g_{EP}) pairing in this ensemble region will give an acceptable onset of activity of knee extensor.

A similar ensemble can be taken for the interval $[t_{min}^{off}, t_{max}^{off}]$, with the effect that the upper boundary is $g_{EP}^{max}(\lambda_E; off)$ generated for t_{max}^{off}, and the lower boundary by $g_{EP}^{min}(\lambda_E; off)$ generated for t_{min}^{off} (dashed lines in Figure 45). The overlap of these two ensemble regions, shown in Figure 45, is then the region of successful rostral rhythms.

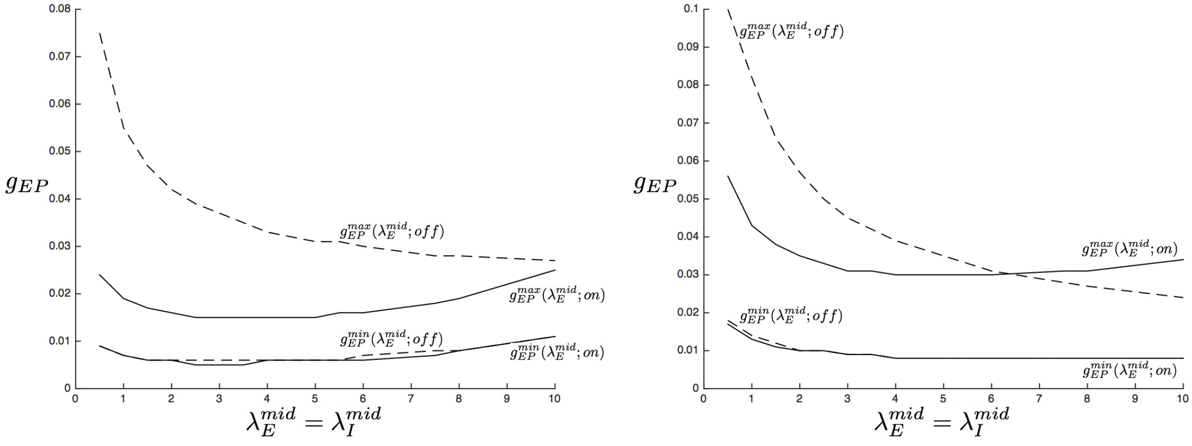

Figure 45: The overlap of successful termination regions from Figure 44 (dashed lines) and activation regions from Figure 43 (solid lines) give the region in parameter space for which successful rostral rhythms may occur. Left: $g_{IP} = g_{EP}/4$. Right: $g_{IP} = g_{EP}/10$.

3.7.3 Firing rate estimates

In order to have some measure of firing rate throughout a rhythm, we perform Fokker-Planck analysis following the numerical scheme set forth in [49]. This does require the case of very low synaptic weights with high Poisson process rates (the Asymmetric regime). Similar agreement can be achieved in other parameter regimes with lower rates for the Poisson process. The approach outlined here can quickly test sets of parameters, resulting in general regimes of activity versus non-activity for a given set of parameters.

We use the usual conservation equation to relate probability P of finding a neuron near voltage V to the current J of neurons whose dynamics bring them past a voltage V at time t: $\frac{\partial P}{\partial t} + \frac{\partial J}{\partial V} = 0$. Synaptic drive is treated in the diffusion approximation. The spike-reset mechanism used in integrate and fire models is implemented as boundary conditions: $J(V_{th-}, t) = J(V_{re+}, t) - J(V_{re-}, t) = r(t)$. This describes the current just below threshold, setting it equivalent to the firing rate, $r(t)$. Taking into account spike reset, we rewrite the Fokker-Planck conservation equation as

$$\frac{\partial P}{\partial t} + \frac{\partial J}{\partial V} = r(t)(\delta(V - V_{re}) - \delta(V - V_{th}))$$

.

Hence the Fokker-Planck equation is

$$\frac{\partial P}{\partial t} = \frac{\partial^2}{\partial V^2}\left(\frac{\sigma^2(V)}{\tau}P(V)\right) + \frac{\partial}{\partial V}\left(\frac{V-E}{\tau}P(V)\right),$$

with associated current operator

$$\mathcal{J} = \frac{E-V}{\tau} - \frac{\partial}{\partial V}\frac{\sigma^2}{\tau}$$

satisfying $\mathcal{J}P = J$.

To use this formulation, which finds steady state solutions, we must make a few assumptions. We subdivide the run time into small bins. In each bin, the deterministic synapses are held constant at the average value in the bin rather than time varying, and our stochastic spike trains are homogeneous Poisson process with rate $\lambda_{I,E}$ = the average of $\lambda_{I,E}(t)$ for the bin. An example of a few of these bins in the rostral rhythm are shown in Figure 46.

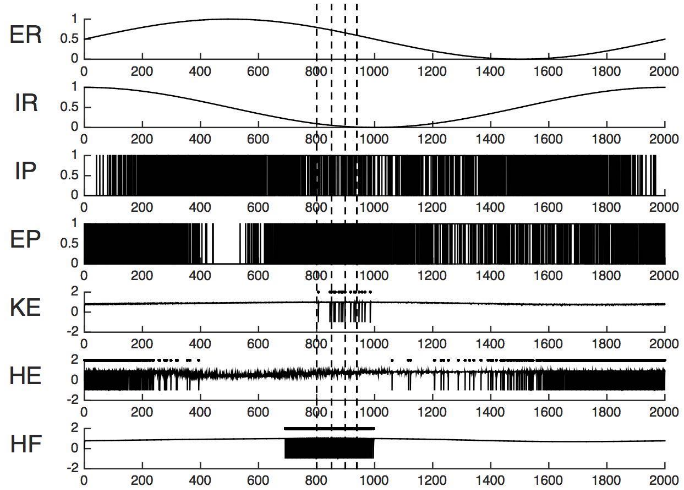

Figure 46: A rostral rhythm in the Asymmetric parameter regime is simulated. The dashed vertical lines represent a few of the time bins used for firing rate estimates.

With this assumption, the constant deterministic synaptic inputs can be absorbed into an effective leak current with reversal, $E_L = \frac{\mu + g_{detE}s_{detE}V_{exc} + g_{detI}s_{detI}V_{inh}}{1 + g_{detE}s_{detE} + g_{detI}s_{detI}}$ and time constant $\tau_L = \frac{C}{1 + g_{detE}s_{detE} + g_{detI}s_{detI}}$.

Recalling that the amplitude of each Poisson spike in our formulation is $1 - e^{-g_{stochE,I}} \equiv b_{stochE,I}$, we can now define the values used in the Fokker-Planck equation and current operator:

$$\begin{aligned} \frac{\sigma^2(V)}{\tau} &= \frac{1}{2}\left(\lambda_E b_{stochE}^2 (V - V_{exc})^2 + \lambda_I b_{stochI}^2 (V - V_{inh})^2\right) \\ \frac{V-E}{\tau} &= \frac{V-E_L}{\tau_L} + \lambda_E b_{stochE}(V - V_{exc}) + \lambda_I b_{stochI}(V - V_{inh}) \end{aligned} \tag{3.4}$$

Solving the latter for τ, E gives:

$$\begin{aligned} E &= \frac{E_L + \tau_L \lambda_E b_{stochE} V_{exc} + \tau_L \lambda_I b_{stochI} V_{inh}}{1 + \tau_L \lambda_E b_{stochE} + \tau_L \lambda_I b_{stochI}} \\ \tau &= \frac{\tau_L}{1 + \tau_L \lambda_E b_{stochE} + \tau_L \lambda_I b_{stochI}} \end{aligned} \tag{3.5}$$

The steady state solution takes $\frac{\partial P}{\partial t} = 0$, therefore quantities with a 0 subscript denote quantities at steady state. We relabel $\frac{V-E_0}{\tau_0} + \frac{\partial}{\partial V}\frac{\sigma_0^2}{\tau_0} \equiv \frac{(V-E_0\prime)}{\tau_0\prime}$. Then we can rewrite the Fokker-Planck conservation equation as

$$\begin{aligned} -\frac{\partial J_0}{\partial V} &= r_0(\delta(V - V_{th}) - \delta(V - V_{re})) \\ -\frac{\partial P_0}{\partial V} &= \frac{\tau_0}{\sigma_0^2}\left(\frac{(V-E_0\prime)}{\tau_0\prime} P_0 + J_0\right) \end{aligned} \tag{3.6}$$

which is suitable for solving numerically via integrating backwards from threshold, as described in [49], for each bin.

We can compare the firing rate of knee extensor predicted by this theory in assorted time bins with the firing rate from simulation, see Table 3 and Figure 47. The simulation values shown in Table 3 are the average of 5000 runs of the asymmetric case with rostral inputs. Figure 47 displays this data. The theory and simulation do not match. During knee extensor activity ($t = 840 - 980ms$), the spike rates seen in simulation are higher than those predicted by the theory, and the total period of activity appears shorter in simulation than predicted by theory. We hypothesize that the mismatch is due to the homogeneous being an insufficient estimate in each bin. Considering more slowly varying synaptic inputs to the motoneurons may improve the match.

Table 3: Firing rate estimates, theory versus simulation

Time (ms)	Theory (kHz)	Simulation (kHz)
620-640	0.000	0
640-660	0.000	0
660-680	0.000	0
680-700	0.000	0
700-720	0.000	0
720-740	0.0002	0
740-760	0.0012	0
760-780	0.0042	0
780-800	0.0104	0
800-820	0.0199	0.0002
820-840	0.0311	0.1997
840-860	0.0420	0.2496
860-880	0.0505	0.2997
880-900	0.0557	0.2498
900-920	0.0570	0.1499
920-940	0.0544	0.0001
940-960	0.0485	0.0001
960-980	0.0399	0.0001
980-1000	0.0300	0.0001
1000-1020	0.0201	0.0001
1020-1040	0.0117	0
1040-1060	0.0058	0
1060-1080	0.0024	0
1080-1100	0.0008	0
1100-1120	0.0002	0
1120-1140	0.0000	0

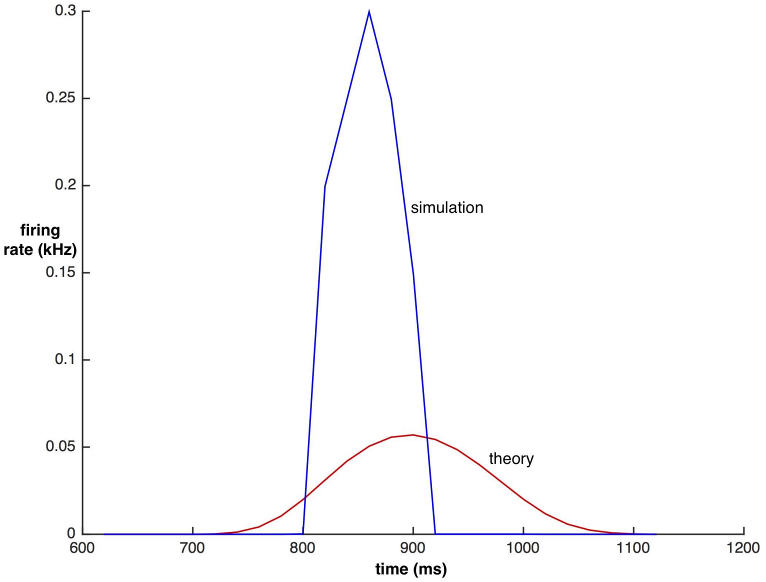

Figure 47: Firing rate estimates, theory versus simulation. Blue: plot of trial-averaged firing rate data. Red: plot of theory-based firing rate data. All data taken from Table 3.

The windows in which theory predicts a non-zero rate while the simulations fail to fire are an effect of our approximation. A rate of 0.0002 kHz translates to 1 spike occurring at some point in a 5 second window, or a spike having a 1 in 5 chance of occurring a 1 second window. However, the windows being considered are only 20 milliseconds. Therefore, an expected rate less than 0.05 kHz means there is no guarantee of a spike at all in the 20 millisecond window. We do, however, find that once theory predicts firing rates approximately ≥ 0.02 kHz, knee extensor does indeed fire in simulation. Therefore, this is a useful criteria for determining the time bins in which knee extensor will begin and cease activity. For times not included in this table, both theory and simulation find a firing rate of 0 kHz.

4.0 ALTERNATIVE APPROACHES TO EXTENSOR-FLEXOR CENTRAL PATTERN GENERATORS

In Chapters 2 and 3, we examined some of the rhythm generating properties of the turtle spinal cord. In this chapter, we investigate results not restricted to the turtle. The spinal locomotor central pattern generator can autonomously generate rhythmic activity with alternating flexion and extension phases over a wide range of frequencies. Due to the complexity of the spinal cord and the difficulty in identifying neurons, the organization of this CPG and the neural mechanisms involved in rhythmogenesis remain largely unknown [41]. It is commonly accepted that many of the rhythmic motor patterns observed in vertebrates, such as walking and scratching, involve inhibitory interactions between two neural populations representing flexor and extensor half-centers [10, 11, 40]. The classical half-center concept assumes a symmetrical organization in regard to cellular properties, operational regimes, and synaptic interactions between the half-centers [11, 42]. More contemporary study of deletions of one population or the other during animal activity has suggested alternative approaches. One such approach suggests an asymmetric, flexor-dominated CPG organization in which only the flexor half-center has intrinsic rhythmic capabilities. This suggestion comes from deletion experiments in which extensor activity completely ceases while the flexor continues to burst rhythmically [21, 71]. Other deletion experiments suggest the possibility that both populations can autonomously generate rhythmic activity [30].

We present a theoretical study examining whether all three mechanisms can operate in the same CPG depending on the methods used to produce the rhythm. A reduced mathematical model in which both extensor and flexor neurons are represented by single non-spiking neurons coupled by mutual inhibition is used for qualitative analysis of system dynamics. Stable rhythmic patterns occurred in both symmetric and asymmetric network structures.

Frequency modulation as external drive to one or both half-centers varies is dependent on the underlying rhythm-generating mechanisms and flexor-extensor symmetry. Our findings propose explanations for the coexistence of the three experimentally suggested yet seemingly contradictory mechanisms for rhythmogenesis. This work is ongoing in collaboration with the Rybak group at Drexel University, who are developing a large scale model of the same phenomena.

In Section 4.1, we will provide an overview of findings in deletion experiments, and we define the three CPG mechanisms we wish to investigate. We will define a reduced mathematical model in Section 4.2, and summarize the intrinsic behavior of an isolated model neuron. We will vary external drives to both extensor and flexor with fixed inhibition strength in Section 4.3; the bifurcation diagrams produced by this are a first step in categorizing the solution types each mechanism is capable of generating. We also explore the frequency modulations each mechanism is capable of producing in this regime. In Section 4.4, we will vary the external drive to extensor and the strength of inhibition for different fixed intrinsic behaviors of flexor. Doing so allows us to identify additional behaviors that each mechanism is capable of generating. We also explore frequency control and the roles of escape and release. In Section 4.5, we vary an equal external drive to both extensor and flexor and strength of inhibition in representative combinations of intrinsic extensor and flexor behavior, and again explore frequency control. In the discussion, we summarize our findings (including the unique properties we identified for each mechanism) and suggest future directions for research.

4.1 EXPERIMENTAL BACKGROUND

A wide variety of deletions are observed in vertebrates such as cats [21], turtles [61], and mice [71, 30]. Some of these variations suggest that non-traditional CPG organization may exist. Specifically, three mechanisms are considered, as discussed above:

(M1) The classical half-center concept assumes a symmetrical organization between the half-centers. Both extensor and flexor are tonic in isolation. This is the mechanism that would be suggested by hip extensor deletions during rostral scratch in turtle [61] and in several experiments in cat [10, 11].

(M2) An asymmetric, flexor-dominated CPG organization in which only the flexor half-center has intrinsic rhythmic capabilities. Extensor is tonic in isolation and flexor is bursting. This is observed during deletion experiments in cats and mice [21, 71].

(M3) Both populations can autonomously generate rhythmic activity and are bursting in isolation. This was found in mice by Hagglund et al [30].

Our goal is to characterize the types of behavior each mechanism may generate. We also seek to examine the frequencies of bursting solutions each mechanism can generate. Any distinctions we can identify among the three mechanisms may be useful in guiding future experiments.

In this section, we summarized three different potential mechanisms for rhythmogenesis in an extensor-flexor CPG that have been suggested by deletion experiments in a variety of vertebrates. In the next section, we will present the architecture we implement, provide a mathematical description of neurons in our model, and describe the intrinsic behavior of an isolated model neuron.

4.2 MODEL

We consider a pair (extensor E and flexor F) of mutually inhibitory neurons modeled with a persistent sodium current and driven by an external, excitatory conductance, shown in Figure 48. The persistent sodium current has been used in previous CPG modeling studies [20, 14, 54, 53], has been observed experimentally in neurons in other CPGs [68], and is well suited to supply the voltage plateaus underlying bursts of spikes. Due to this intrinsic mechanism, an increase of excitatory drive to each isolated half-center causes a transition from silence to rhythmic bursting to tonic activity. In this chapter, we define "bursting" here as an oscillating solution and "tonic activity" as convergence to a depolarized fixed point. By manipulating drives to each half-center, we can induce systematic transitions between all three half-center mechanisms described in the previous section. We analyze the bifurcations involved in transitions between them, the emergence of bistability, and the control of oscillation frequency in each regime.

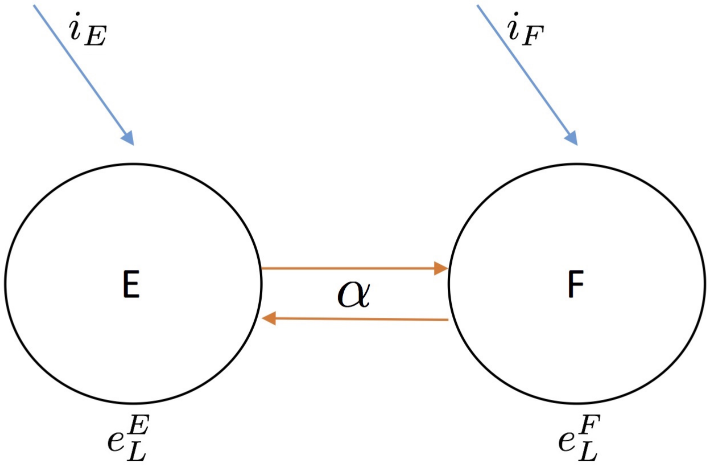

Figure 48: Architecture for reduced extensor-flexor model. The red connections are mutual inhibition of strength α between extensor E and flexor F. E has leak reversal potential e_L^E and receives external excitatory drive i_E (blue). F has leak reversal potential e_L^F and receives external excitatory drive i_F (blue).

The neurons obey the following equations with parameters listed in Table 4:

$$\begin{aligned} C_m\dot{V_i} &= -I_{NaP}(V_i,h_i) - I_L(V_i) - I_{syn}(V_i,V_j) - I_{ext}(V_i) \equiv F_i(V_i,h_i,V_j) \\ \dot{h_i} &= (h_\infty(V_i) - h_i)\tau_h(V_i) \equiv g_i(V_i,h_i) \end{aligned} \tag{4.1}$$

where, for $i \in \{E,F\}$, V_i denotes voltage and h_i denotes the inactivation of the persistent sodium current, I_{NaP}.

In the differential equation for evolution of the voltage for population i:

$$\begin{aligned}
I_{NaP}(V_i, h_i) &= -g_{NaP} m_\infty h_i (V_i - e_{Na}) \\
m_\infty(V_i) &= (1 + \exp((V_i - m_{half})/\theta_m))^{-1} \\
I_L(V_i) &= g_L(V_i - e_L^i) \\
I_{syn}(V_i, V_j) &= \alpha f(V_j)(V_i - e_{syn}^{inh}) \\
f(V_j) &= (1 + \exp(-(V_j - V_{avg})/V_{diff}))^{-1} \\
V_{avg} &= ((v_{max} + v_{min})/2) \\
V_{diff} &= ((v_{max} - v_{min})/10) \\
I_{ext}(V_i) &= i_i(V_i - e_{syn}^{exc})
\end{aligned} \tag{4.2}$$

In the differential equation describing the evolution of the persistent sodium current for population i:

$$\begin{aligned}
h_\infty(V_i) &= (1 + \exp((V_i - h_{half})/\theta_h))^{-1} \\
\tau_h(V_i) &= \cosh((V_i - V_{\tau NaP})/k_{\tau NaP})/\tau_{NaP}
\end{aligned} \tag{4.3}$$

The synaptic output from neuron j to neuron i, $f(V_j)$, is non-instantaneous and is shown in Figure 49. The persistent sodium current allows a neuron's intrinsic behavior (silent, oscillatory, or tonic) to be set using a combination of external drive and leak reversal. The details of this are given below. Therefore, exploring the transitions between the three mechanisms (M1)-(M3) comes down to varying: the intrinsic behavior of E (the values of i_E and/or e_L^E), the intrinsic behavior of F (i_F and/or e_L^F), and the strength of inhibition (α). These parameters are discussed as they arise in our analysis.

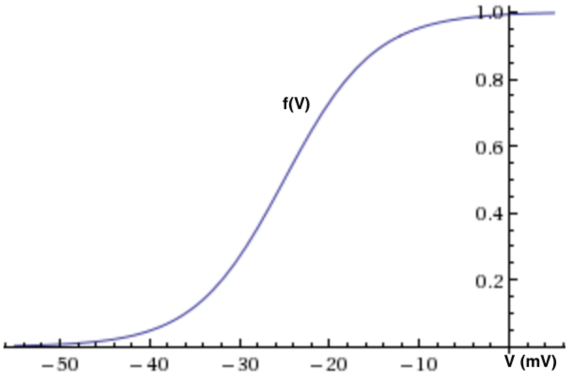

Figure 49: The non-instantaneous synaptic output function used, $f(V)$.

Table 4: Model Parameters

Parameter	Value
C_m	20 pF
g_{NaP}	5 nS
e_{Na}	50 mV
m_{half}	-40 mV
θ_m	-6 mV
g_L	2.8 nS
e_{syn}^{inh}	-75 mV
v_{max}	0 mV
v_{min}	-50 mV
e_{syn}^{exc}	0 mV
h_{half}	-55 mV
θ_h	12 mV
$V_{\tau NaP}$	-55 mV
$k_{\tau NaP}$	24 mV
τ_{NaP}	4000 ms

Intrinsic behavior. In the absence of mutual inhibition ($\alpha = 0$), the intrinsic behavior of a model population, i, is determined by a combination of leak reversal (e_L^i) and applied external drive. Figure 50 is an example phase plane of such an isolated model neuron. The red curves are the V-nullclines for different levels of external drive, and the green curve is the h-nullcline for the given cell. We fix $e_L^i = -63mV$. Then, in the absence of external drive, the neuron has a stable fixed point on the left branch of the cubic V-nullcline (labeled '1' in Figure 50) and so the neuron remains at a silent steady state solution. When external drive is applied, the V-nullcline is lowered. Eventually, the stable fixed point on the left branch of the V-nullcline is lost, and an unstable fixed point on the middle branch of the V-nullcline (labeled '2') is gained. In this case, the neuron has access to both a left knee to transition from silent to active and a right knee to transition from active to silent. There is also no stable fixed point corresponding to steady state behavior present, and so the neuron is intrinsically bursting. Finally, with additional external drive, the unstable middle fixed point is lost, and a stable fixed point on the right branch of the V-nullcline labeled '3' is gained. This corresponds to a tonically active, steady state solution. Note that, due to the parameters used in this model, there is only one fixed point at any given time.

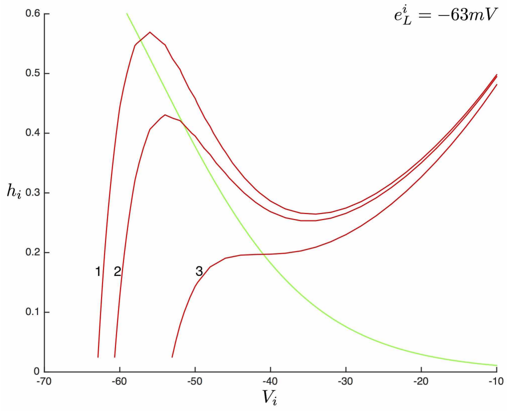

Figure 50: Nullclines depicting intrinsic behavior of an isolated model neuron. The red curves are the V-nullcline for different levels of external drive, and the green curve is the h-nullcline for the given cell. The V-nullcline labeled '1' is the case no external drive. The V-nullclines labeled '2' and '3' are cases as increasing external drive is added, showing how a fixed point can change from left, to middle, to right.

The intrinsic behavior can be further explored in a two-parameter bifurcation diagram. Figure 51 is the two parameter bifurcation diagram produced by AUTO [23] for this model. Beginning with neuron j in the silent state, increasing either e_L^j or i_j progresses the intrinsic activity from silent to bursting to tonic via Hopf bifurcations (the blue curves in Figure 51 and subsequent figures). The curves of Hopf bifurcations are straight lines in $i_j - e_L^j$ space because each parameter only appears in equations (4.1)-(4.2) as constant terms. Therefore, the overall input to neuron j is $g_L e_L^j + i_j$ and behavior remains qualitatively the same whenever this quantity is constant.

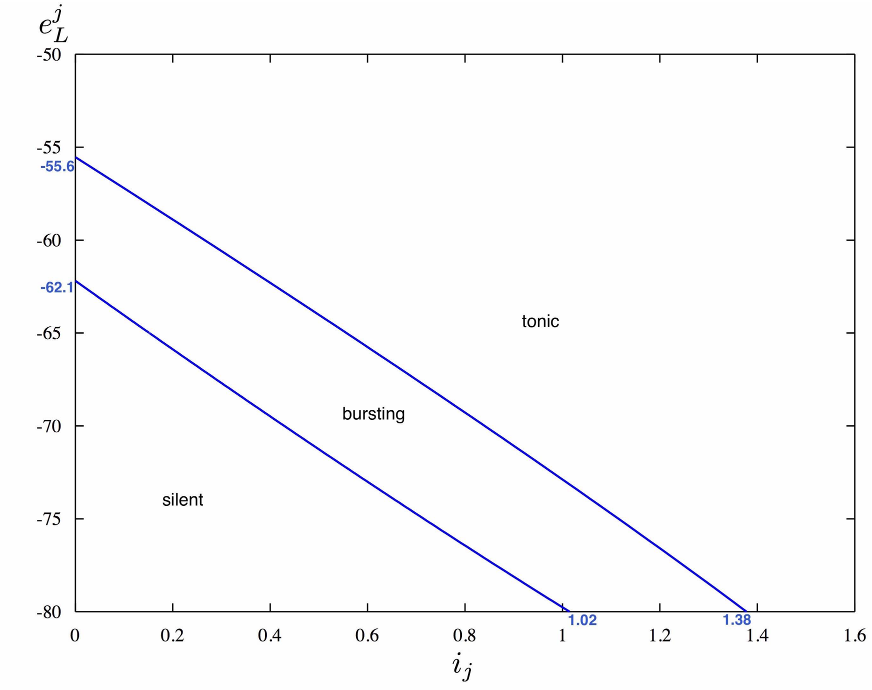

Figure 51: Intrinsic behavior of an isolated model neuron. When $\alpha = 0$, the intrinsic behavior of model neuron j is presented as a function of i_j and e_L^j via a two-parameter bifurcation diagram. The blue curves are Hopf bifurcations.

In our analysis, we vary intrinsic behavior of population j by varying either i_j or e_L^j as convenient. In this section, we presented the architecture we implement, provided a mathematical description of neurons in our model, and described the intrinsic behavior of an isolated model neuron. In the next section, we will examine how varying external drives to E and F impact the solution types and frequency changes each mechanism can produce.

4.3 FIXED α RESULTS

We begin our analysis by fixing inhibition strength at $\alpha = 1$, and leak reversal at $e_L^E = e_L^F = -62.5$. In the absence of external drive, E and F are each intrinsically silent but very close to the bursting region in Figure 51. In the absence of inhibition, neuron j is intrinsically silent for $0 < i_j < 0.023$; intrinsically bursting for $0.023 < i_j < 0.393$; and intrinsically tonic for $i_j > 0.393$. These values of i_E, i_F are depicted in Figure 52 as light gray, dashed lines.

Figure 52 is a two-parameter bifurcation diagram depicting regimes of behavior for E and F as i_E and i_F vary. Fixing either i_E or i_F and allowing the other to vary in AUTO generates a 1-parameter bifurcation diagram. Hopf bifurcations, fold bifurcations, and limit points of period cycles can all be easily grabbed in the 1-parameter figures, and continued in AUTO as both parameters vary. The results of this are the two-parameter bifurcation diagram shown in Figure 52. There is a small region where both E and F are silent, at values of $i_j < 0.0174$. As i_E, i_F are increased, curves of Hopf bifurcations (blue) signal the transition among different regimes of activity as labeled. There are two regions of bursting separated by a curve of Hopf bifurcations: bursting I and bursting II. In bursting I, the inputs to E and F are sufficiently low that both have an unstable fixed point on the middle branch of its V-nullcline. Thus transition mechanisms between E active and F active (and vice versa) such as intrinsic escape and intrinsic release [56] are more likely in bursting I. Additionally, pauses between E and F bursts are possible in bursting I. The curve of Hopf bifurcations that separates bursting I from bursting II indicates a change in fixed points: in bursting II, at least one of the neurons has a stable fixed point on the right branch of its V-nullcline (at least one neuron is intrinsically tonic).

In Figure 52, the regions of parameter space corresponding to (M1), (M2), and (M3) are defined by light gray dashed lines, and color coded in purple, green, and orange. (M1) is the region where E and F are both intrinsically tonic, $i_E, i_F > 0.393$. (M2) is the region where E is intrinsically tonic and F is intrinsically bursting, $i_E > 0.393$ and $0.023 < i_F < 0.393$. Finally, (M3) is the region where both E and F are intrinsically bursting, $0.023 < i_E, i_F < 0.393$.

For fixed $\alpha = 1$, we see that the (M1) region only admits bursting solutions and solutions where E and F are both tonic. Mechanism (M2) admits both bursting solutions and solutions where E is tonic and F is silent. Mechanism (M3) admits both bursting solutions and non-biological periodic solutions. All three mechanisms, then, are certainly capable of coexisting in the same mathematical model and the differences in permitted solution types provides a possible avenue for experimental validation of this model. It is noteworthy that mechanism (M3) is not capable of producing any tonic solutions. Therefore, tonic behavior observed in experiment would most likely be due to either (M1) or (M2).

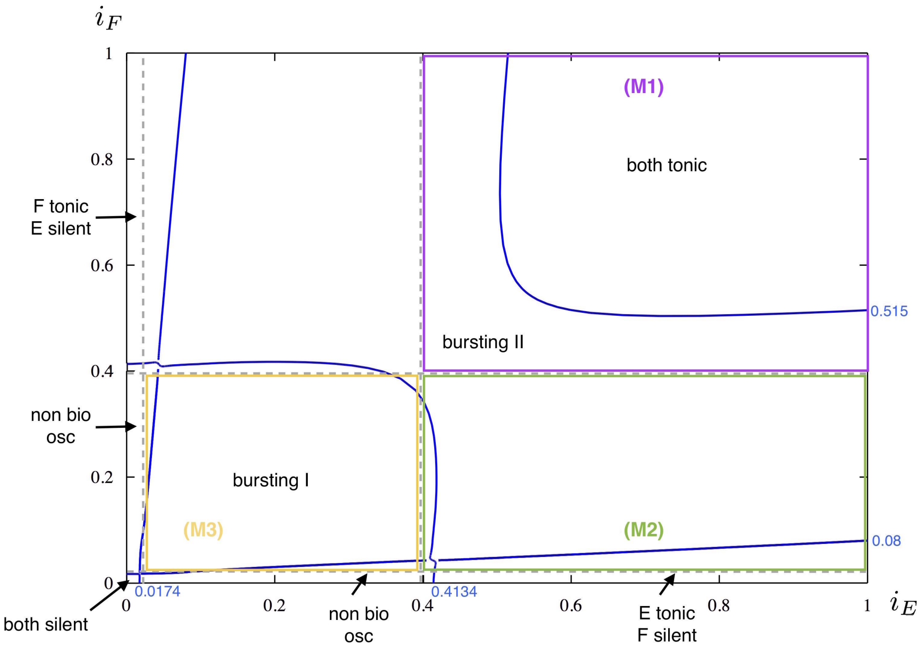

Figure 52: Two-parameter bifurcation diagram for fixed $\alpha = 1$ as i_E and i_F vary. Solution types are labeled in black and apply to regions defined by the blue curves of Hopf bifurcations. Light gray dashed lines correspond to different intrinsic behaviors of E and F in isolation ($\alpha = 0$). These intrinsic behaviors (gray dashed lines) define the regimes of behavior for each mechanism, which are color coded with outlined boxes.

Frequency control. Figure 53 depicts the frequency of oscillations for E as i_E and i_F are varied. The voltage threshold used for spike detection was -30mV in this and in all subsequent figures. Reflecting the body of the figure across the line $i_E = i_F$ gives the frequencies for F (because $e_L^E = e_L^F$ and the mutual inhibition is equally strong in both directions). Within Figure 53, there is significant symmetry across the diagonal $i_E = i_F$. Of note are the regions labeled n:1 and 1:n. In these regions, E experiences n active phases for every active phase of F (n:1) or vice versa. These are non-biological oscillations, and they account for a significant portion of the bursting I region. For values of i_E, i_F outside of this region, the bursting solutions are biologically relevant and diagonal symmetry is present. We do not consider cases in which E or F is intrinsically silent. Such a case is not seen in experiments, and our model produces biologically unrealistic bursting solutions in these regimes.

It is noteworthy that mechanism (M1) accounts for the highest frequency oscillations in this slice through parameter space. Mechanism (M2) displays the widest range of frequencies, and mechanism (M3) produces the lowest frequency bursting solutions.

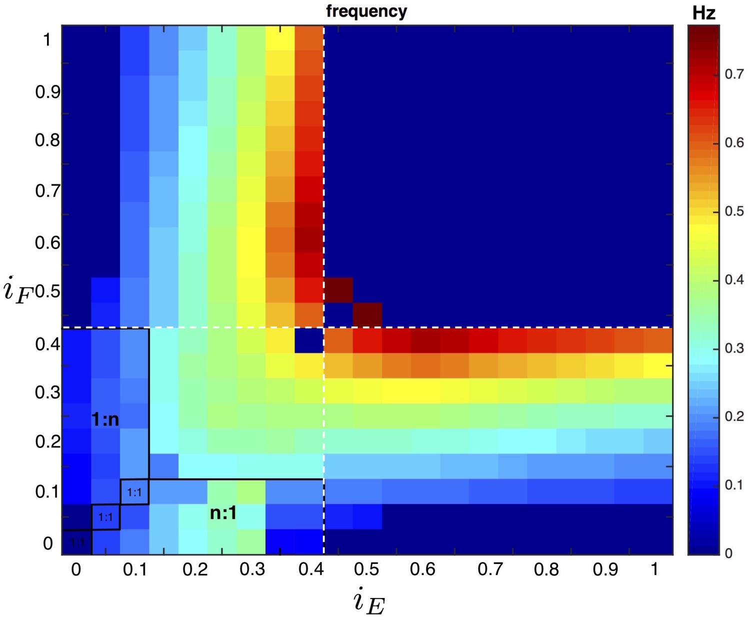

Figure 53: Frequency changes of E for fixed $\alpha = 1$ as i_E and i_F vary. Regimes of oscillation where E and F bursts do not occur in a 1:1 ratio are labeled. Reflecting across the $i_E = i_F$ diagonal line gives the frequency changes for F. The voltage threshold for spike detection is -30mV. The intrinsic behaviors (white dashed lines) define the regimes of behavior for each mechanism, as the gray dashed lines did in Figure 52.

In this section, we examined how varying external drives to E and F impact the solution types and frequency changes each mechanism can produce. In the next two sections, we consider how varying α impacts the solution behaviors possible from each mechanism (M1)-(M3). In Section 4.4, we will consider varying α and drive to E in a pair of cases in which F has prescribed intrinsic behavior. We will consider the impact of these variations on solution type and frequency control, and we will examine the relative contribution of escape and release transition mechanisms to frequency.

4.4 ASYMMETRIC DRIVE RESULTS

In this section, we examine the impacts of varying inhibition strength on the solution types each mechanism (M1)-(M3) can generate. To do so, we cannot simultaneously vary the behavior of E and F as we did in the previous section. Instead, we explore horizontal slices of Figure 52: the behavior of F is fixed to be either intrinsically bursting or tonic, and in the absence of inhibition, E is transitioned from silent to bursting to tonic by varying i_E. The behavior of F is fixed with e_L^F rather than i_F but Figure 51 shows these are interchangeable control mechanisms. In this approach, E and F receive equal strength mutual inhibition α, but only E receives external excitatory drive i_E. Examples of the horizontal slices we take through Figure 52 are sketched in Figure 54.

We use the intrinsic behavior of F (tonic or bursting) to define cases. In each case, E is intrinsically silent ($e_L^E = -65mV$) and i_E is increased from 0 so that E progresses from silent to bursting to tonically active without changing e_L^E. It is necessary to know where a neuron transitions from silent to bursting to tonic in the absence of inhibition so that we may correctly identify parameter regions corresponding to each CPG mechanism. Figure 55 displays the i_E one parameter bifurcation curve when $\alpha = 0$, $e_L^E = -65$. The transitions occur via Hopf bifurcations at $i_E = 0.152$ (silent to bursting) and at $i_E = 0.5566$ (bursting to tonic). Again, bifurcations in a 1-parameter diagram such as Figure 55 can be followed in AUTO to generate 2-parameter diagrams as i_E and α vary.

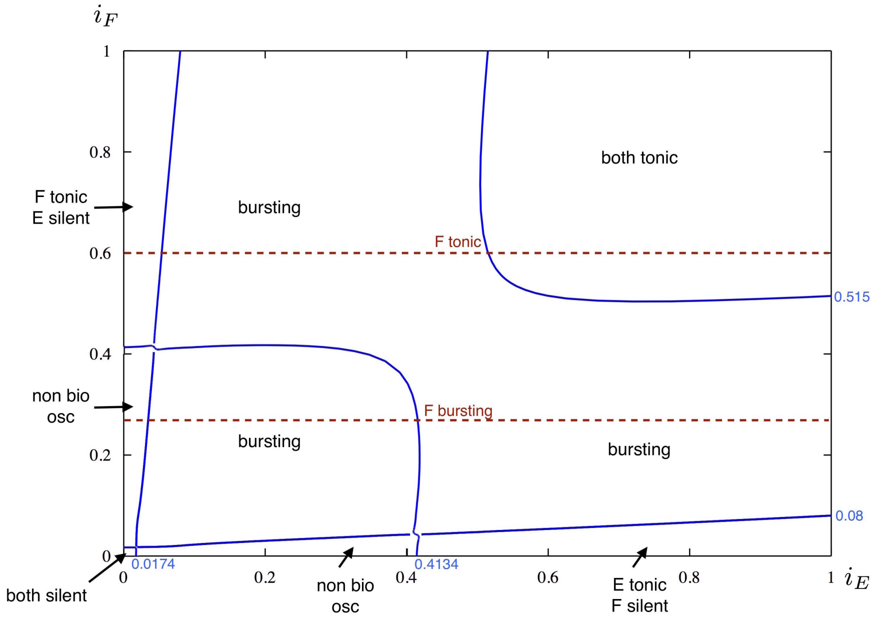

Figure 54: Two-parameter bifurcation diagram for fixed $\alpha = 1$ as i_E and i_F vary. Solution types are labeled in black and apply to regions defined by the blue curves of Hopf bifurcations. Dashed dark red horizontal lines represent the cases we consider.

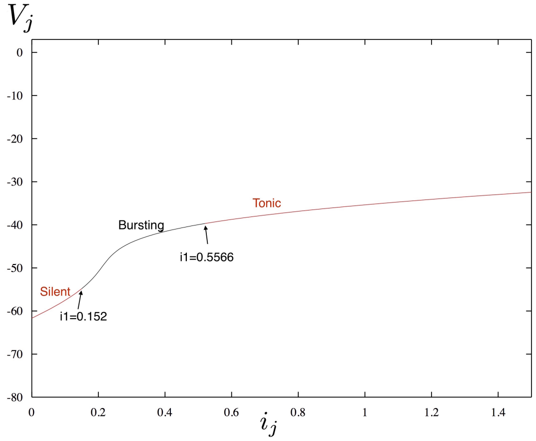

Figure 55: Transitions of intrinsic behavior for neuron j as i_j is varied. $\alpha = 0$ and $e_L^j = -65mV$. Stable steady state solutions are given in red. Unstable steady state solutions corresponding to bursting behavior are given in black.

The case where F is intrinsically tonic allows exploration of the impact of varying α on the behaviors possible from mechanism (M1). The case where F is intrinsically bursting allows exploration of the impact of varying α on the behaviors possible from (M2) and (M3).

We first consider the case where F is intrinsically tonic ($e_L^F = -53mV$). The 2-parameter bifurcation diagram for drive to E (i_E) versus inhibition strength (α) is given in Figure 56. The region to the right of the dashed gray line correspond to values of $i_E > 0.5566$, where E is tonic in the absence of inhibition (Figure 55). Therefore, the region to the right of the gray line corresponds to mechanism (M1) being responsible for oscillations and is labeled in light gray.

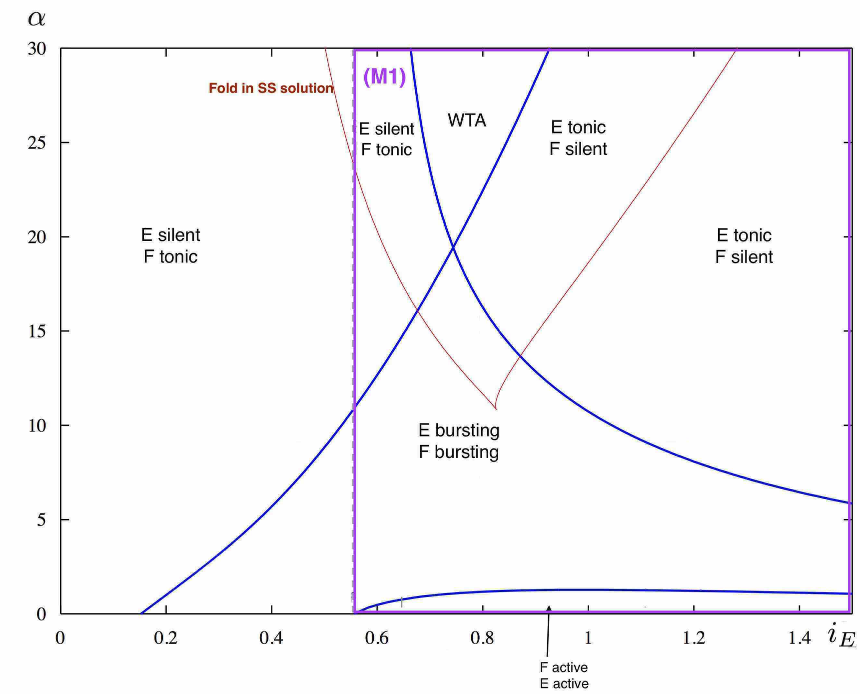

Figure 56: Two-parameter bifurcation diagram for $i_F = 0, e_L^F = -53mV$ as i_E and α vary. Solution types are labeled in black and apply to regions defined by the blue curves of Hopf bifurcations. The red curve is a curve of fold bifurcations in the steady state (SS) solutions. Light gray dashed lines correspond to different intrinsic behaviors of E and F in isolation ($\alpha = 0$). These intrinsic behaviors (gray lines) define the regimes of behavior for each mechanism, which are color coded with outlined boxes.

In addition to the region of bursting solutions and the region where E and F are both tonically active present in Figure 52, there are additional regimes of solution behavior once α is allowed to vary from 1. For stronger mutual inhibition, there are regimes of solutions where E is tonic and F is silent, F is tonic and E is silent, and a winner take all (WTA) regime. We define a winner take all regime to be a region of parameter space in which two stable steady state solutions coexist, and the ultimate solution is determined by the initial conditions used to solve the system of differential equations. Mechanism (M1) is the only case with WTA in this asymmetric drive approach, and this may be a useful benchmark for experiments. We find that this observation holds in the symmetrically driven cases we consider in Section 4.5.

The WTA regime is able to arise because the curves of Hopf bifurcations cross and are enveloped by curves of fold bifurcations. To demonstrate this, we fix $\alpha = 30$ and examine the 1-parameter bifurcation diagram generated as i_E varies. This is shown in Figure 57. Note that in the region labeled WTA, two stable steady state solutions coexist. Diagrams for other values of α in the WTA regime in Figure 56 are similar to Figure 57. Prior to this crossing of Hopf bifurcation curves, no such regime may arise. This is demonstrated in Figure 58: we fix $\alpha = 12$ and examine the 1-parameter bifurcation diagram generated as i_E varies. Because the Hopf bifurcation curves have not crossed and the fold bifurcations occur between them, a stable bursting solution may still be produced, rather than a WTA regime. The maximum and minimum voltages achieved during the burst are plotted in green in Figure 58.

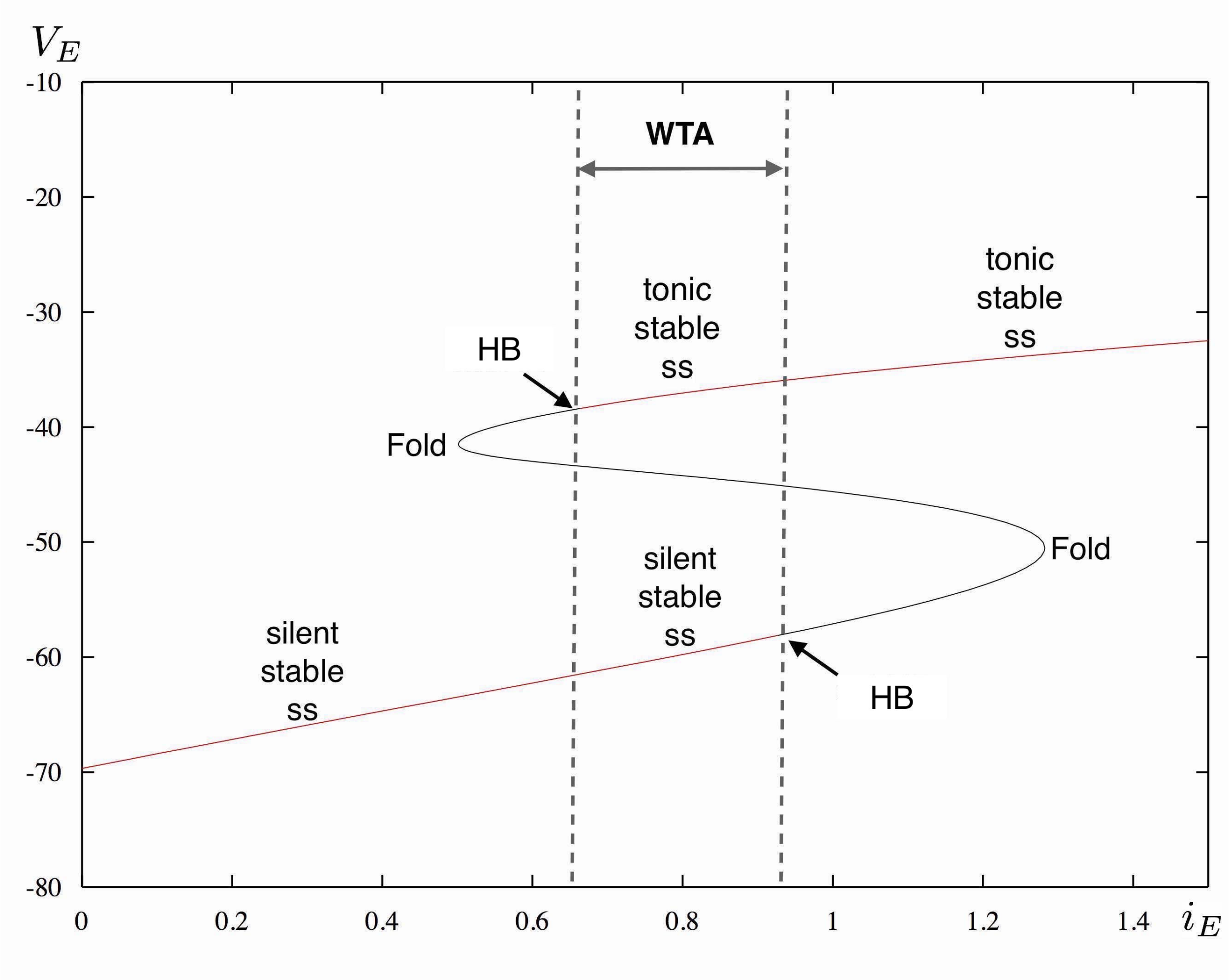

Figure 57: Transitions of intrinsic behavior for E as i_E is varied with $\alpha = 30$ fixed, in the region labeled WTA in Figure 56. Stable steady state solutions are given in red. Unstable steady state solutions are given in black. Fold and subcritical Hopf bifurcations in the steady state solution are labeled. The region in which both a tonic and a silent stable steady state solution exist is defined by dashed vertical lines, and labeled WTA.

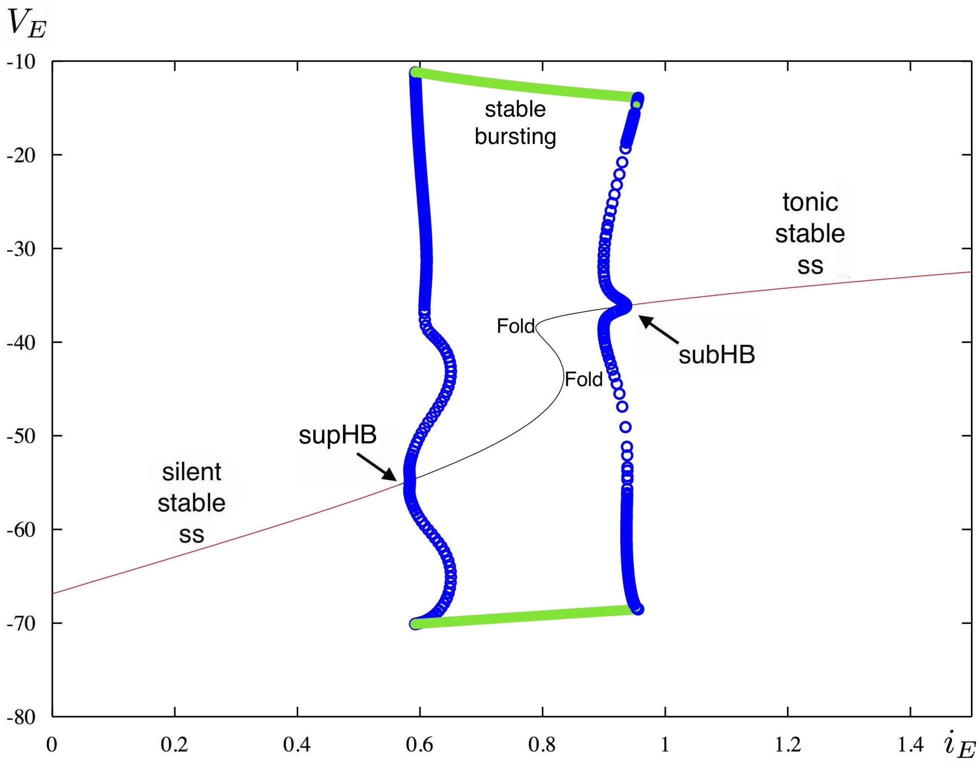

Figure 58: Transitions of intrinsic behavior for E as i_E is varied with $\alpha = 12$ fixed, in the region labeled WTA in Figure 56. Stable steady state solutions are given in red. Unstable steady state solutions are given in black. Fold and subcritical Hopf bifurcations in the steady state solution are labeled. The maximum and minimum voltages achieved during bursting are plotted in green.

We next consider the case where F is intrinsically bursting ($e_L^F = -59mV$) so that we may explore mechanisms (M2) and (M3) further. The 2-parameter bifurcation diagram for external drive to E (i_E) versus inhibition strength (α) is given in Figure 59.

At low values of α and i_E, E transitions from displaying subthreshold periodic oscillations to a biological bursting solution. This transition is not structural; it occurs once E receives enough external drive to escape oscillating between two left fixed points. This transition is consistent the one seen in Figure 53 in which E moves from n:1 (1:n) solutions to biologically reasonable solutions.

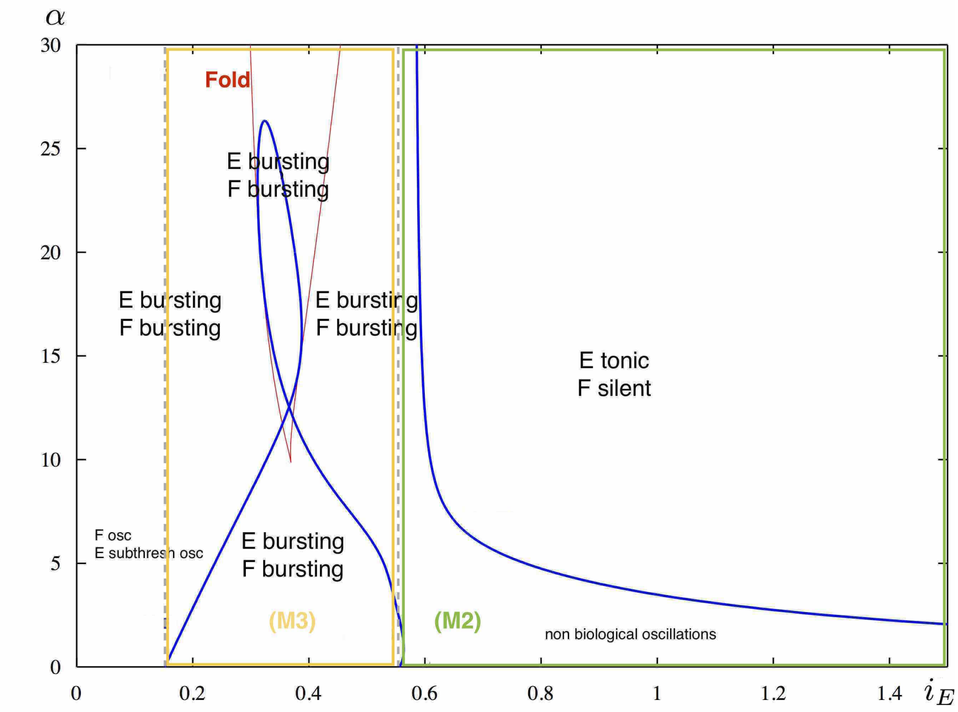

Figure 59: Two-parameter bifurcation diagram for $i_F = 0, e_L^F = -59mV$ as i_E and α vary. Solution types are labeled in black and apply to regions defined by the blue curves of Hopf bifurcations. The red curve is a curve of fold bifurcations in the steady state (SS) solutions. Light gray dashed lines correspond to different intrinsic behaviors of E and F in isolation ($\alpha = 0$). These intrinsic behaviors define the regimes of behavior for each mechanism, which are color coded and labeled.

There is no WTA regime as was seen in the (M1) case, despite the presence of a Fold bifurcation enveloping crossed Hopf bifurcations. This is due to the additional Hopf curve occurring at larger values of i_E. Stable, biologically realistic oscillations emanate from this Hopf, backwards towards smaller i_E. The Hopf curves between the folds generate unstable orbits, and so there is no stable steady state between them for winner take all to be possible.

Although the (M1) case has a greater variety of solution types, the regime corresponding to (M3) has the largest region of biological oscillations, persisting over similar excitatory drives for a much larger range of inhibition strengths than considered here. The region corresponding to (M2) finds a very narrow i_E-band of biologically reasonable oscillations persisting to large values of α. However, much of the (M2) region consists of non-biological oscillations. In these non-biological oscillations, the large external drive to E, i_E, raises the voltage to non-realistic values rather than any structural change occurring.

4.4.1 Frequency control

In this section we examine frequency changes within the bursting regions in Figures 56 and 59. Figure 60 corresponds directly to Figure 56, and Figure 61 corresponds directly to Figure 59.

Figure 60 displays frequency changes of E in the F tonic case, as the parameters α and i_E are varied. The regions of oscillations in this figure do match those bounded by the Hopf bifurcation curves in the two-parameter Figure 56. In this case, the greatest frequency for each value of i_E occurs at small α. Mechanism (M1), then, is not capable of producing large frequency bursting solutions (or indeed, any bursting solutions) at very large values of α. Oscillations in the presence of very strong inhibition are likely due to either (M2) or (M3).

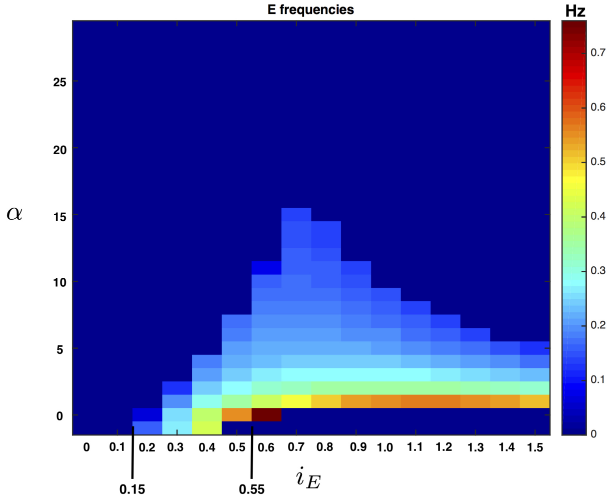

Figure 60: Frequency changes of E for $i_F = 0, e_L^F = -53mV$ as i_E and α vary. The values of i_E at which the intrinsic state of E changes as in Figure 55 are labeled. The voltage threshold for spike detection is -30mV.

Figure 61 displays frequency changes of E in the F bursting (M2), (M3) cases as the parameters α and i_E are varied. The regions of bursting in the frequency figure do match those bounded by the Hopf bifurcation curves in the two-parameter Figure 59. In the F bursting case, oscillations persist to large α, and the frequency decreases more gradually as α is increased than was the case for (M1). It is, however, worth noting that the maximum frequency achieved by mechanism (M1) is about twice as high as that achieved by either (M2) or (M3). Finally, the frequency of solutions produced by mechanisms (M2) and (M3) is far less variable than those solutions produced by (M1). These frequency differences, in addition to the dramatic solution differences at large α, provide a possible future avenue for experiment.

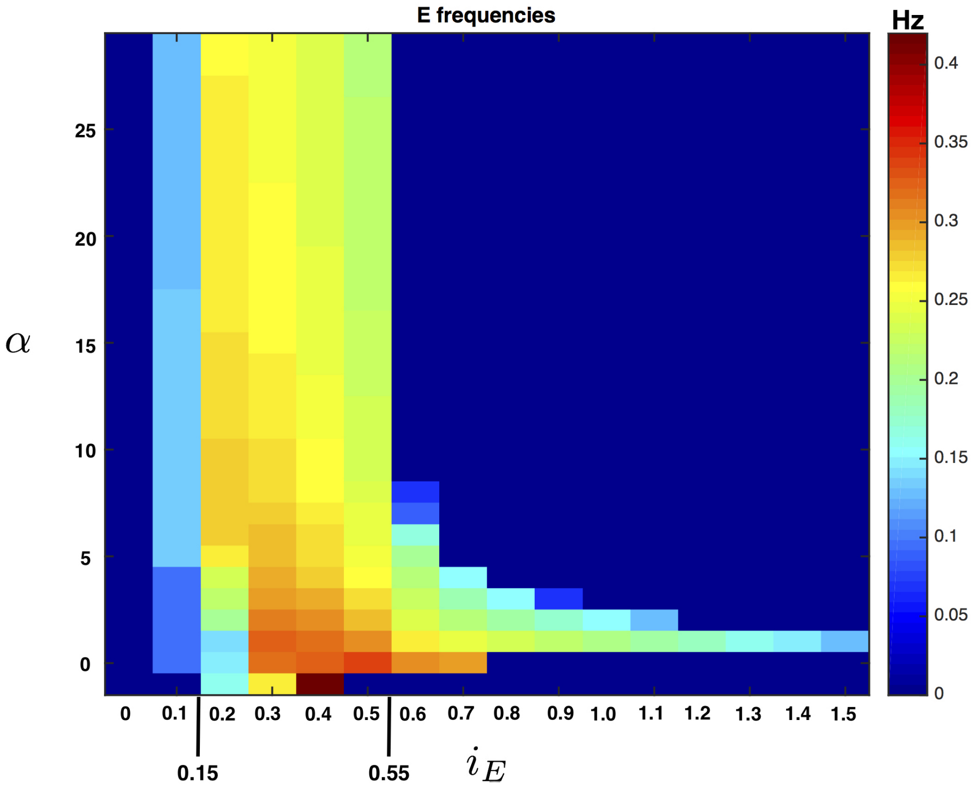

Figure 61: Frequency changes of E for $i_F = 0, e_L^F = -59mV$ as i_E and α vary. The values of i_E at which the intrinsic state of E changes as in Figure 55 are labeled. The voltage threshold for spike detection is -30mV.

The clear regions of increasing and decreasing frequency shown in Figures 60 and 61 suggest that an examination of the role escape versus release is worthwhile. Classically, escape is associated with increasing frequency as drive is increased, and release is associated with decreasing frequency as drive is increased. This is systematically examined in the next section.

4.4.2 Escape versus release

In this section, we consider the roles escape and release play in the frequency changes observed in the previous section. Classical frequency criteria for determining escape versus release can be helpful in our investigation, but are not the entire story. *Escape* is typically characterized by increasing frequency with increasing external drive. *Release* is typically characterized by decreasing frequency with increasing external drive. In Skinner et al [56], four escape/release mechanisms are identified with the following caveat: "The synaptic coupling is assumed to have a sharp threshold and a fast time constant... If some of these assumptions are relaxed, the qualitative behavior remains similar, but the distinction between the four mechanisms becomes less sharp." We certainly have relaxed these assumptions: Skinner et al use a Heaviside function as opposed to our sigmoid $f(V)$. Therefore, there is a lack of sharp distinction in transition mechanisms in our results.

In each F case, we examine the regions of parameter space where frequency is increasing and where frequency is decreasing. Within each of those regions, we examine the transition from E active to F active and the transition from F active to E active separately, since they may be controlled by different mechanisms. Table 5 summarizes the basic mechanisms responsible for transitions in these different cases. The column "Freq" refers to the parameter regions labeled as "inc freq" or "dec freq" in Figures 62 and 65. We use the abbreviation "Es" for escape and "Re" for release. What we label as "escape mediated by release" in Table 5 is similar to what Skinner et al [56] referred to as "Synaptic release," Similarly, what we label as "release mediated by escape" is comparable to Skinner's "Synaptic escape." Details of these mechanisms are provided in our analysis below. There are often competing mechanisms between the two transitions in the rhythm.

Table 5: Summary of basic transition mechanisms for the Asymmetrically driven approach to extensor-flexor CPGs.

F	**Freq**	α	**E to F mechanism**	**F to E mechanism**	**CPG Mechanism**
Tonic	inc	very small	Es mediated by Re	intrinsic Es	(M1)
	inc	larger	Es mediated by Re	Es mediated by Re	(M1)
	dec	any	Es mediated by Re	Re mediated by Es	(M1)
Burst	inc	any	intrinsic Re	intrinsic Es	(M3)
	dec	any, $i_E \leq 0.7$	intrinsic Re	Re mediated by Es	(M2) or (M3)
	dec	small w/ large i_E	intrinsic Es	Re mediated by Es	(M2)

We first consider the case when F is tonic, mechanism (M1). Figure 62 outlines the region of increasing frequency versus decreasing frequency for the E cell.

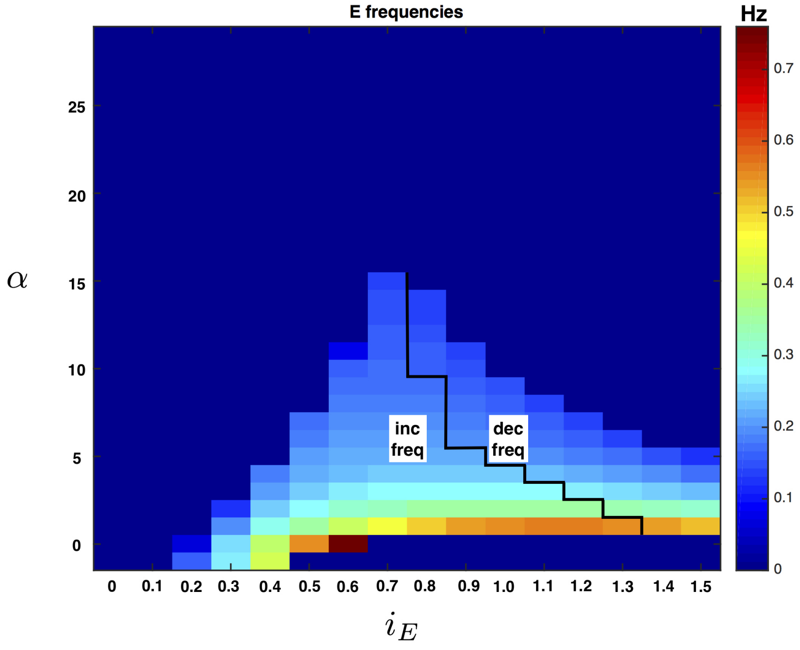

Figure 62: Frequency changes of E from Figure 60 are reproduced. The regions in which frequency increases as i_E increases for fixed α, and in which frequency decreases as i_E increases for fixed α are labeled.

The region of increasing frequency corresponds to rows 1 and 2 of Table 5. For both E to F and F to E transitions, the inhibited cell gets above the left knee of its V-nullcline and escapes, suppressing the free cell. In the case of E activating, this is through intrinsic escape. However, in the case of F activating, this is only possible because the inhibition from the free cell to the inhibited cell has sufficiently decayed, lowering the left knee. This is illustrated in Figure 63. Hence, escape is the mechanism for transition, but it is only possible because some release has occurred. The frequency increases in this region because the escape has a stronger impact than the release. For example, at $\alpha = 3$, increasing i_E from 0.4 to 0.6 results in the active phase of E being largely unchanged, and the active phase of F shortening, explaining the increasing frequency. Carefully tracking the trajectories of E and F in $V - h$ phase space verifies that E begins to activate and is on the fast portion of its trajectory while F is still on slow (active) branch of its trajectory indicating escape is the primary transition mechanism. The story is the same as F approaches activation from the silent phase. Behavior is similar at other parameter values in the increasing frequency region.

The region of decreasing frequency in Figure 62 corresponds to row 3 of Table 5. Here, the E to F transition is due to escape of F made possible by decaying inhibition from E, as in the increasing frequency regime. The transition from F to E, however, is via release mediated by escape: once $V_E > V_{min} = -50$, $f(V_E)$ increases and this slight increase in inhibition to F raises its V-nullcline, allowing F to be below the right knee of its V-nullcline and transition to the silent phase. This occurs while E is still on the slow portion of its trajectory in the silent phase. Once F has transitioned to silent, E is released and able to activate. This mechanism is depicted in Figure 64. The frequency decreases in this region because an increase in i_E moves the E fixed point further right to a higher voltage. Voltages are all still less than $V_{max} = 0mV$, so synaptic output $f(V)$ has not saturated. This shift in E fixed point therefore leads to stronger inhibition from E to F, raising the left knee of the V-nullcline of F, and extending the time F spends in the silent phase (and E in the active phase) before reaching the knee and escaping. The active duration of F is largely unchanged. A study of E and F duty cycles in addition to frequency would likely be very useful in the future.

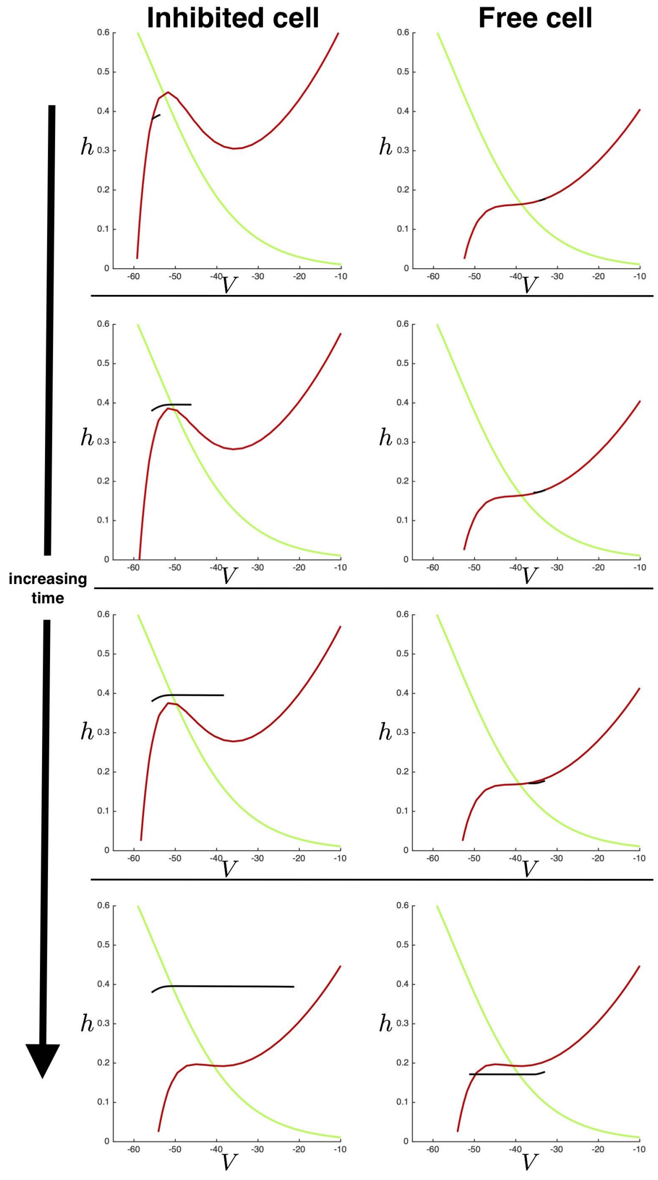

Figure 63: The escape mediated by release mechanism is demonstrated. Each row is a pair of $V - h$ phase planes for the Inhibited Cell (Left) and the Free Cell (Right) at a certain point in time. The red curve is the V-nullcline and the green curve is the h-nullcline for the given cell. The black curve is a portion of the trajectory. As time increases (going down), the inhibition from the Free Cell to the Inhibited Cell wears off, lowering the V-nullcline of the Inhibited Cell. The V-nullcline is lowered sufficiently, the Inhibited Cell rises above the left knee and escapes, row two. The Inhibited Cell is on the fast transition to the active phase while the Free Cell is still on the slow portion of its trajectory, row three. Finally, as time progresses and the Inhibited Cell is sufficiently far in its fast transition to active, the Free Cell begins its fast transition to silent, row four.

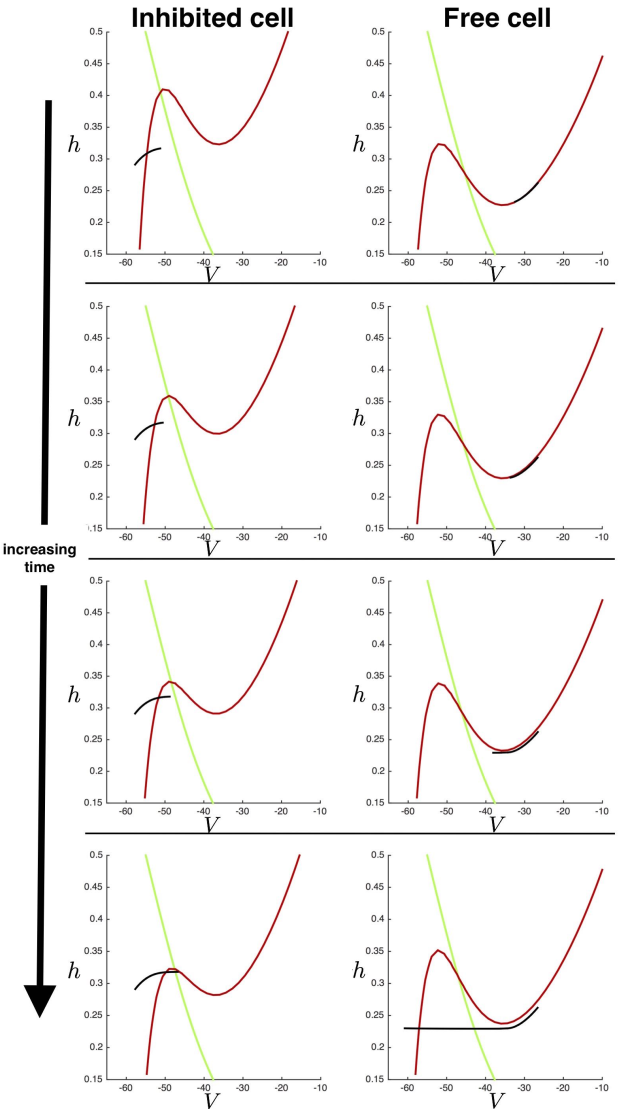

Figure 64: The release mediated by escape mechanism is demonstrated. Each row is a pair of $V - h$ phase planes for the Inhibited Cell (Left) and the Free Cell (Right) at a certain point in time. The red curve is the V-nullcline and the green curve is the h-nullcline for the given cell. The black curve is a portion of the trajectory. As time increases (going down), the Inhibited Cell crosses $V_{min} = -50$ and begins to slightly inhibit the Free Cell. This occurs before the Free Cell has reached the right knee of its V-nullcline, row two. The V-nullcline of the Free Cell is raised sufficiently by this additional inhibition that the Free Cell is now below the right knee of its V-nullcline and begins its fast transition to the silent phase, row three. This occurs while the Inhibited Cell still has not reached the left knee of its V-nullcline to activate. Once the Free Cell has progressed sufficiently on the transition to silent, the Inhibited Cell is released and will begin its fast transition to active, row four.

We next consider the case of F intrinsically bursting, mechanisms (M2), (M3). Figure 65 outlines the region of increasing frequency versus decreasing frequency for the E cell. Figure 65 suggests that mechanism (M2), where $i_E > 0.55$, can only display bursting solutions of decreasing frequency as more external drive is given to E. This is not actually the case. In Figure 52, the region corresponding to mechanism (M2) displays both increasing and decreasing frequencies as i_E is increased for fixed values of i_F. This illustrates one of the challenges of tackling this three-parameter system: by taking two-parameter slices, it is very possible to miss information and make incorrect conclusions. It is true that *in this two-parameter slice*, (M2) is only capable of producing bursting solutions of decreasing frequency as more external drive is given to E. But across the entire three-parameter space, this does not hold and therefore is not a useful identifying feature of solutions produced by mechanism (M2).

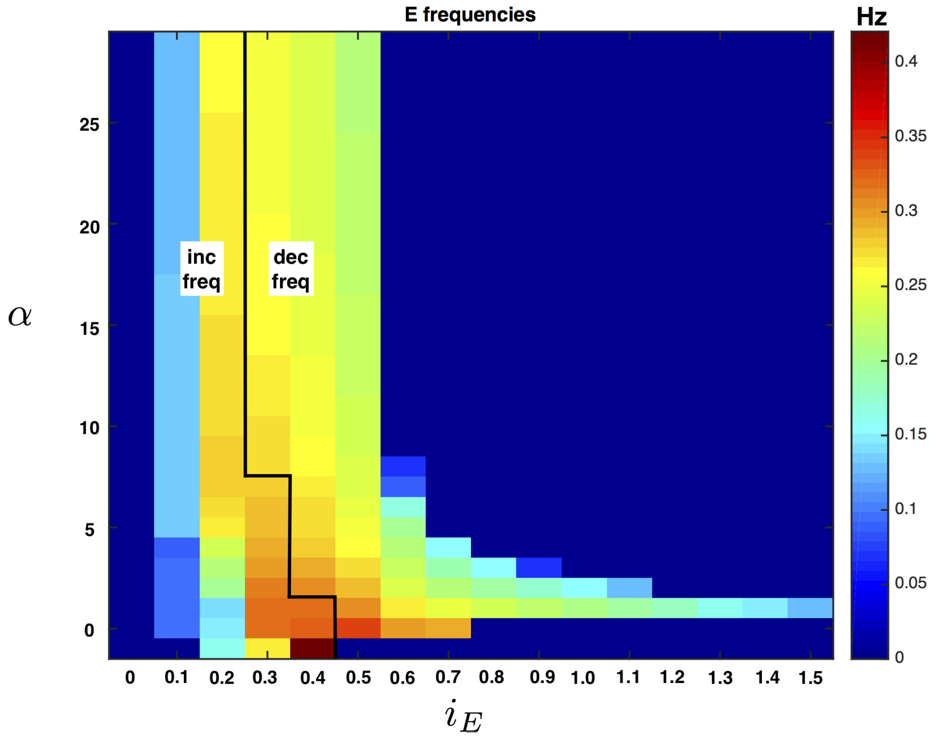

Figure 65: Frequency changes of E from Figure 61 are reproduced. The regions in which frequency increases as i_E increases for fixed α, and in which frequency decreases as i_E increases for fixed α are labeled.

For small α, as i_E is increased beyond 0.7, there is a switch from F activating by intrinsic release to F activating by intrinsic escape (row 6 of Table 5). This is because F maintains a middle fixed point while in the silent phase, and E is trapped at a stable right fixed point with a non-cubic V-nullcline due to the high i_E. E has no right knee to fall below and release F. Therefore, transition does not occur until F reaches the left knee of its V-nullcline and escapes. The mechanism by which E activates in this case is more nuanced. The combination of α and i_E means the V-nullcline for E is monotonic even when E is in the silent phase. Therefore, while it appears to follow the same pattern of release mediated by escape, it is difficult to say with certainty. E gets to approximately $-40mV$ on its slow trajectory before F is inhibited enough to fall below a right knee and release E. Once α grows sufficiently large at large i_E, the V-nullcline of F is raised to have a left fixed point (rather than middle) and F can no longer escape. E is still trapped at the same right fixed point with a non-cubic V-nullcline prohibiting release, and so oscillations cease.

Just as in the F tonic case, the frequency decreases because an increase in i_E moves the E fixed point further right to a higher voltage. Voltages are all still less than $V_{max} = 0mV$, so $f(V)$ has not saturated. This shift in E fixed point therefore has a stronger inhibitory effect on F, raising its left knee and extending the time F spends in the silent phase (and E in the active phase) before reaching the knee and escaping. The active duration of F is largely unchanged.

For smaller values of i_E (rows 4 and 5 of Table 5), the V-nullcline for E is still cubic and examining the transition mechanisms is relatively straightforward. The region of increasing frequency is due to the intrinsic escape in the F to E transition dominating the intrinsic release in the E to F transition. The region of decreasing frequency sees the F to E transition occur by release mediated by escape. The intrinsic release in the E to F mechanism dominates the frequency changes, leading to the decrease. Across both increasing and decreasing frequency regimes, for fixed $i_E \leq 0.7$, the frequency increases as α is decreased because the lower α facilitates E escape.

In this section, we've systematically explored the role of escape and release mechanisms in frequency changes. We've considered an asymmetric set up in which only E receives external drive and the intrinsic state of F is fixed so that we could explore the regimes of behaviors each mechanism (M1)-(M3) can create as α varies. However, we had to consider mechanism (M1), with F tonic, separately from mechanisms (M2) and (M3) with F bursting. In the next section, we explore a symmetrically driven approach to explore the three mechanisms more coherently.

4.5 SYMMETRIC DRIVE RESULTS

The previous section used an asymmetrically driven approach to analyze the properties of mechanisms (M1)-(M3) as strength of inhibition, α, varies. This amounted to essentially taking horizontal slices through Figure 52 and then varying α. While this did lead to finding additional regimes of behavior not found in Figure 52, the approach required examining mechanism (M1) separately from mechanisms (M2) and (M3). In this section, we will consider diagonal slices through Figure 52 so that the mechanisms can be examined more cohesively. Examples of the diagonal slices we take through Figure 52 are sketched in Figure 66.

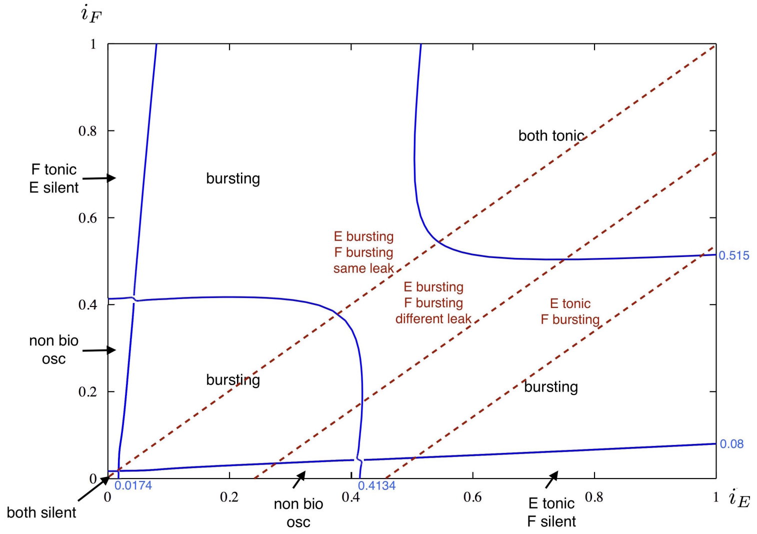

Figure 66: Two-parameter bifurcation diagram for fixed $\alpha = 1$ as i_E and i_F vary. Solution types are labeled in black and apply to regions defined by the blue curves of Hopf bifurcations. Dark red horizontal lines represent the cases we consider.

We consider 3 cases. First we consider F intrinsically bursting ($e_L^F = -60mV$) and E intrinsically tonic ($e_L^E = -50mV$) so that we may explore how mechanism (M2) transitions to mechanism (M1). Second, we consider E and F intrinsically bursting ($e_L^E = e_L^F = -60mV$), so that we may consider how mechanism (M3) transitions to mechanism (M1). Finally, we consider E and F intrinsically bursting, but with different leak reversals ($e_L^E = -60mV, e_L^F = -62mV$) so that we may consider (M3) to (M2) to (M1) in one figure. In each case, E and F will receive equal external excitatory drive, $i_F = i_E$. As i_E and α vary, we examine different solution behaviors possible from the different mechanisms.

In the absence of inhibition, a neuron with $e_L = -60mV$ will transition from bursting to tonic behavior at $i_F = i_E = 0.2654$. A neuron with $e_L = -62mV$ will transition from bursting to tonic behavior at $i_F = i_E = 0.39$. In Figures 67, 68, and 69, these values of i_E are denoted by dashed gray lines, and the resulting regions corresponding to (M1), (M2), and (M3) are marked with light gray labels.

We first consider the case of F intrinsically bursting ($e_L^F = -60mV$) and E intrinsically tonic ($e_L^E = -50mV$) so that we may explore how mechanism (M2) transitions to mechanism (M1). The two-parameter bifurcation diagram as i_E and α vary is given in Figure 67. We find that mechanism (M2) admits the following solution types: E tonic and F silent and both E and F bursting. This is consistent with the behaviors observed in Figure 59. Mechanism (M1) admits many of the same solution types identified in Figure 56. However, in this slice, there is no regime of WTA behavior. Additionally, a new regime of behavior is found: for both (M1) and (M2) bistability between solutions where E and F are bursting and where E is tonic and F is silent, defined by the (blue) curve of subcritical Hopf bifurcations and the (dark gray) curve of limit points of periodic orbits. The bistability region for (M1) is, however, significantly larger in $i_E - \alpha$ space than the bistability region for (M2). The region for (M2) is so small that (M1) would almost certainly be responsible for the observance of bistability between tonic and bursting solutions in experiment.

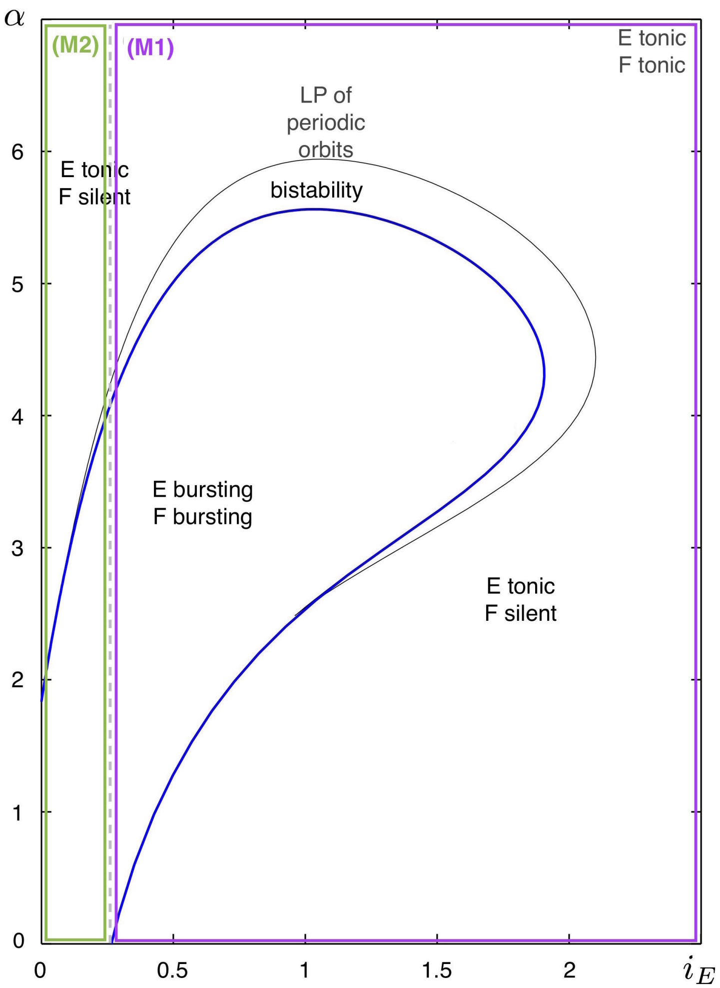

Figure 67: Two-parameter bifurcation diagram for $e_L^E = -50mV, e_L^F = -60mV$ as $i_E(= i_F)$ and α vary. Solution types are labeled in black and apply to regions defined by the blue curves of Hopf bifurcations. The dark gray curve is a curve of limit points of periodic orbits. This curve defines a region of bistability between solutions in which E and F burst and solutions in which E is tonic and F is silent. Light gray dashed lines correspond to different intrinsic behaviors of E and F in isolation ($\alpha = 0$). These intrinsic behaviors define the regimes of behavior for each mechanism, which are color coded and labeled.

We next consider E and F intrinsically bursting ($e_L^E = e_L^F = -60mV$), so that we may consider how mechanism (M3) transitions to mechanism (M1). The two-parameter bifurcation diagram as i_E and α vary is given in Figure 68. We find that mechanism (M3) admits only bursting solutions, as was the case in the previous section. Mechanism (M1) admits the same solutions identified in Figure 56, and a new region of bistability between E and F bursting solutions and WTA solutions is present.

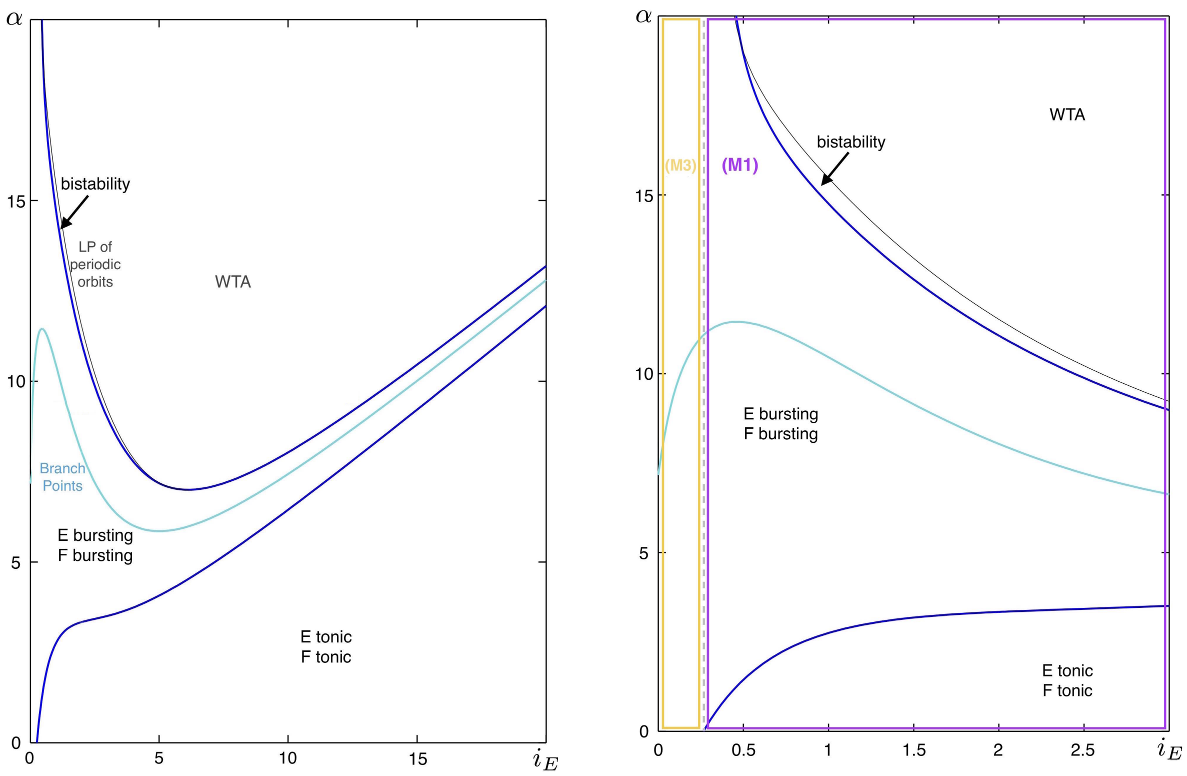

Figure 68: Two-parameter bifurcation diagram for $e_L^E = e_L^F = -60mV$ as $i_E(= i_F)$ and α vary. Solution types are labeled in black and apply to regions defined by the blue curves of Hopf bifurcations. The dark gray curve is a curve of limit points of periodic orbits. This curve defines a region of bistability between solutions in which E and F burst and WTA solutions. Light gray dashed lines correspond to different intrinsic behaviors of E and F in isolation $(\alpha = 0)$. These intrinsic behaviors define the regimes of behavior for each mechanism, which are color coded and labeled. Left is the full two-parameter bifurcation diagram for a wide range of i_E values, including those that produce biologically unrealistic oscillatory solutions. Right is the same diagram restricted to smaller values of i_E, where bursting solutions are biologically relevant.

Finally, we consider E and F intrinsically bursting, but with different leak reversals ($e_L^E = -60mV, e_L^F = -62mV$) so that we may consider (M3) to (M2) to (M1) in one figure, Figure 69. The solution types admitted by (M1) and (M2) are consistent with those depicted in Figure 67. The solutions types admitted by (M3) are consistent with those depicted in Figure 68. Thus, no new information is found in this case.

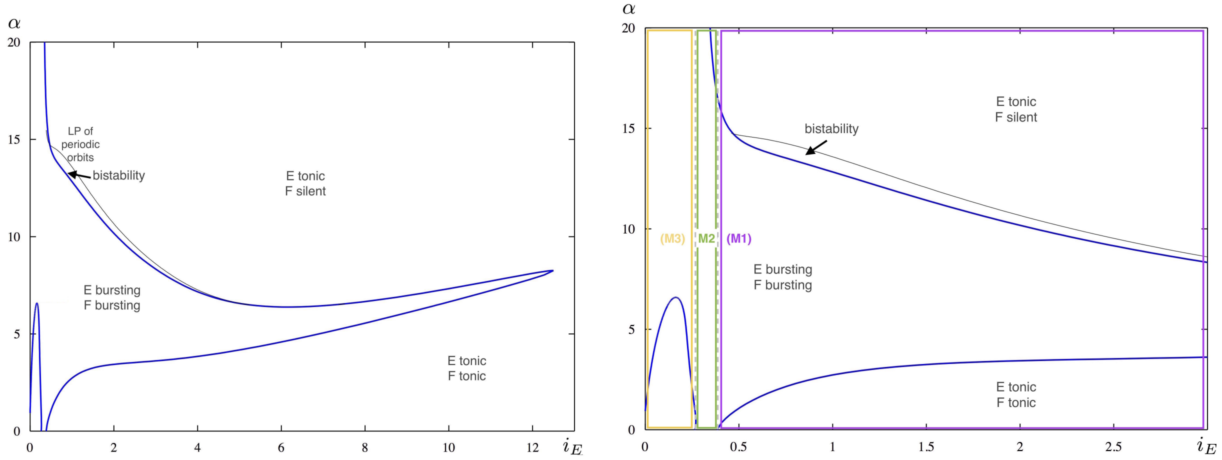

Figure 69: Two-parameter bifurcation diagram for $e_L^E = -60mV, e_L^F = -62mV$ as $i_E (= i_F)$ and α vary. Solution types are labeled in black and apply to regions defined by the blue curves of Hopf bifurcations. The dark gray curve is a curve of limit points of periodic orbits. This curve defines a region of bistability between solutions in which E and F burst and solutions in which E is tonic and F is silent. Light gray dashed lines correspond to different intrinsic behaviors of E and F in isolation ($\alpha = 0$). These intrinsic behaviors define the regimes of behavior for each mechanism, which are color coded and labeled. Left is the full two-parameter bifurcation diagram for a wide range of i_E values. Right is the same diagram restricted to smaller values of i_E.

Frequency control. The frequencies as i_E and α vary corresponding to each two parameter bifurcation diagram are given below: Figure 70 is the case where E is intrinsically tonic and F is intrinsically bursting, and corresponds to Figure 67; Figure 71 is the case where E and F are intrinsically bursting with the same leak reversal, and corresponds to Figure 68; and Figure 72 is the case where E and F are intrinsically bursting with different leak reversals, and corresponds to Figure 69.

The frequencies achieved with symmetric drive are greater than those found in Sections 4.3 and 4.4. Once again the maximum frequency is produced by mechanism (M1), with mechanism (M3) producing the lowest frequency bursting solutions. Overall, there is greater heterogeneity in the patterns of frequency change than were observed in Section 4.4, particularly in the cases where E and F are both intrinsically bursting. These differences again emphasize the issues with taking two-dimensional slices through a three-dimensional parameter space. In the future, a more rigorous method for sampling i_E, i_F and α must be found so that the properties of solutions generated by each mechanism can be more confidently stated.

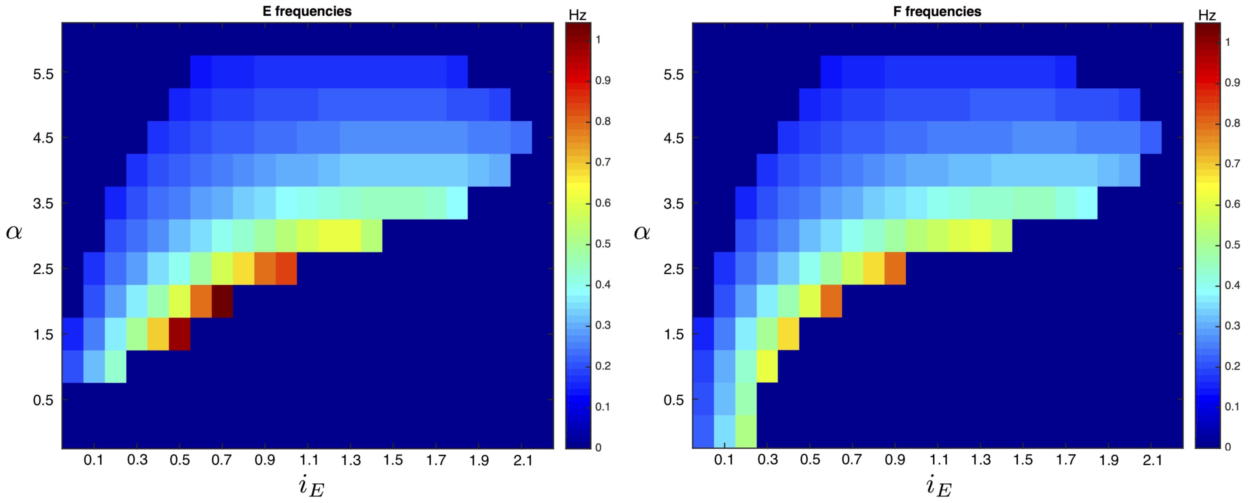

Figure 70: Frequency changes of E (Left) and F (Right) for $e_L^E = -50mV, e_L^F = -60mV$ as $i_E (= i_F)$ and α vary. The voltage threshold for spike detection is -30mV.

The cases where E and F are both intrinsically bursting (Figures 71 and 72) display a new trend in frequency changes. For fixed values of α ranging from approximately 3 to 11, the frequency decreases, increases, and decreases again as i_E is increased. This was not seen in the cases examined in Section 4.4. This is likely due to changes in the roles of escape and release in the E to F and F to E transition mechanisms. We are currently performing the same systematic analysis done in Section 4.4.2 to better understand this observation.

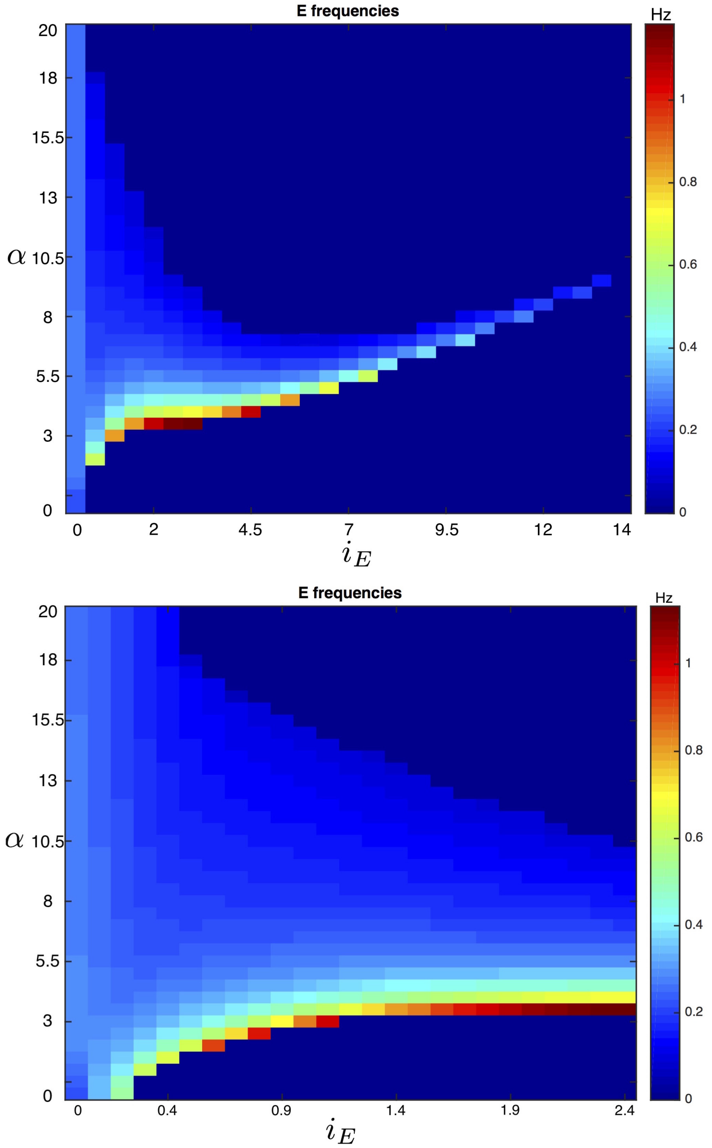

Figure 71: Frequency changes of E for $e_L^E = e_L^F = -60mV$ as $i_E (= i_F)$ and α vary. The voltage threshold for spike detection is -30mV. The frequency changes for F are identical for those of E. Top is for the full two parameter region shown in Figure 68. Bottom is for the range of i_E in which biologically realistic bursting solutions are produced.

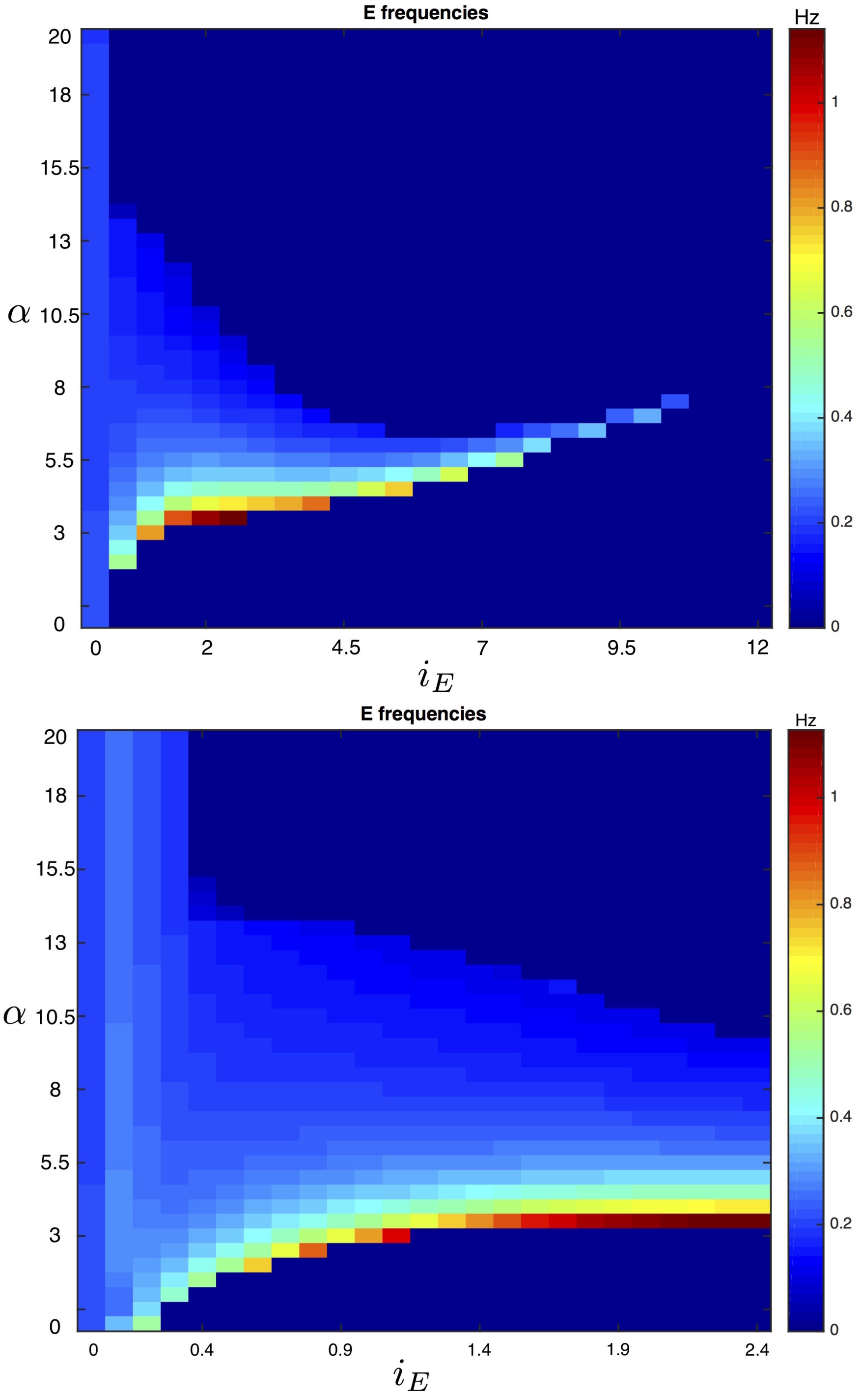

Figure 72: Frequency changes of E for $e_L^E = -60mV, e_L^F = -62mV$ as $i_E (= i_F)$ and α vary. The voltage threshold for spike detection is -30mV. Top is for the full two parameter region shown in Figure 69. Bottom is for the range of i_E in which biologically realistic bursting solutions are produced.

4.6 DISCUSSION

In normal vertebrate motor function, deletions can occur. Experimental investigation has proposed at least three distinct mechanisms in extensor-flexor CPGs: (M1), the classical half-center concept assumes a symmetrical organization between the half-centers with both extensor and flexor are tonic in isolation [61, 10, 11]. (M2), an asymmetric, flexor-dominated CPG organization in which only the flexor half-center has intrinsic rhythmic capabilities. Extensor is tonic in isolation and flexor is bursting [21, 71]. (M3), both populations can autonomously generate rhythmic activity and are bursting in isolation [30].

Computational model simulations support the hypothesis that all three of these mechanisms can coexist in the same CPG model. We simulated a reduced model based on the persistent sodium current. By manipulating three major parameters (the intrinsic state of E, the intrinsic state of F, and the strength of inhibition) we were able to find all three mechanisms in the same model. The transitions between these mechanisms are the Hopf bifurcations in this model: when a population is isolated, Hopf bifurcations occur at the transition from silent to bursting and at the transition from bursting to tonic activity, as external drive is varied. These isolated behaviors are what define each CPG mechanism.

By taking tractable two-dimensional slices through our three-dimensional parameter space, we were able to use bifurcation theory to observe unique features of each mechanism. Mechanism (M1) is capable of producing the following solution types: both E and F tonic, E and F bursting, E tonic and F silent, E silent and F tonic, and winner take all depending on initial conditions. Solutions in which both E and F are tonically active, E silent and F tonic, and winner take all appear to be unique to mechanism (M1), based on our analysis so far. In general, it would be dangerous to over-generalize the trends we have observed in two-parameter slices, and so it is difficult to state with confidence that these are truly unique to (M1). Mechanism (M1) also displays bistability between bursting solutions and tonic solutions in many regimes. Additionally, mechanism (M1) cannot produce oscillations at strong levels of inhibition. (M1) generates the highest frequency bursting solutions seen, with the largest frequency occurring at low α and a dramatic decrease in frequency occurring as α increases. In many of our cases, (M1) generates bursting solutions of approximately double the frequency of (M2) or (M3).

Mechanism (M2) is capable of producing the following solution types: E and F bursting and E tonic and F silent. (M2) displays small regions of bistability in some parameter regimes, but these are generally negligible relative to the bistability displayed by (M1). (M2) generally produces the second highest frequency burst solutions of the three mechanisms, and maintains bursting solutions to large α with significantly less decrease in frequency than (M1) displays.

Mechanism (M3) is capable of producing the following solution types: biologically unrealistic oscillations and E and F both bursting. Therefore, any steady state solutions must be generated by either mechanism (M1) or (M2). (M3) produces the lowest burst frequencies of the three mechanisms, and maintains bursting solutions to large α with less decrease in frequency than (M1) displays. Therefore, bursting behavior observed at strong inhibition in experiment is likely due to either (M2) or (M3).

This list of features for each mechanism can help guide future experiments. However, to be more confident that these features are accurate, an analysis of the full three dimensional parameter space must be undertaken. It may be possible to develop a quantitative cost function and use sampling methods to explore the space more fully. Another avenue for research would be to take a (perhaps larger than considered here) collection of more carefully chosen two-dimensional slices to insure the entire parameter space is represented. It may even be possible to develop a three-parameter bifurcation diagram for the problem, given enough time. In an asymmetrically driven setup, we analyzed the role escape and release transitions [69, 56] played in determining frequency in certain regimes of all three mechanisms. This analysis can, and should, be repeated in other approaches (such as fixing inhibition or a symmetrically driven approach, as we generated frequencies for here). However, it is time consuming to do and it would ultimately be more efficient to deal with the three-dimensional parameter space issue first so that work is not wasted. A more thorough study of the relative contributions of escape and release to rhythm generation by each of the three mechanisms would be valuable. Finally, the question of duty cycle was not examined in depth here. Analyzing duty cycle, in addition to frequency information, would likely provide additional unique features for each mechanism that may be useful in future experiments.

Recent experimental and theoretical work studying left-right leg coordination during locomotor gait in limbed animals has found that certain deletions of interneuron populations connecting a left extensor-flexor pair and a right extensor-flexor pair can cause an animal to switch from a normal left-right alternating activity to a left-right synchronized "hopping" pattern [67, 43, 44]. Specifically, coordination between left and right neural activities in the spinal cord controlling left and right legs is provided by commissural interneurons (CINs). Several CIN types have been genetically identified, including both excitatory and inhibitory types. Recent studies demonstrated that genetic elimination of all CINs caused switching from a normal left-right alternating activity to a left-right synchronized hopping pattern. Interestingly, removal of only the inhibitory CINs resulted in hopping at low locomotor frequencies and normal left-right alternation at high frequencies, whereas removal of certain subpopulations of excitatory CINs maintained the left–right alternation at low frequencies and switched to hopping at high frequencies [67]. Theoretical examination of these observations was undertaken in first a large, biologically detailed computational model [43], and then in a a simplified mathematical model more amenable to analysis [44]. The simplified mathematical model demonstrated all of the experimentally observed behaviors: normal left-right alternation under control conditions, switching to a hopping activity at any frequency after removing both CIN connections, a synchronized pattern at low frequencies with alternation at high frequencies after removing only inhibitory CIN connections, and an alternating pattern at low frequencies with hopping at high frequencies after removing only excitatory CIN connections. A key hypothesis of their work was that the flexor populations had to be intrinsically bursting while the extensor populations had to be intrinsically tonic (our mechanism (M2)) in order for their model to reproduce the observed behaviors. Our work identifying solution types that each extensor-flexor CPG mechanism is capable of producing may allow a relaxation of this requirement in certain parameter regimes, allowing further study and predictions.

5.0 CONCLUSIONS

In this thesis, we used reduced mathematical models to investigate motor pattern generation in vertebrates. In Chapters 2 and 3, we proposed two different models for a single network to generate two distinct scratch rhythms in turtle (rostral and pocket). With our relaxation oscillator based model in Chapter 2, we performed a computational and mathematical study to investigate whether a proposed, unified CPG network, which features only hip-related populations of interneurons, could indeed be responsible for the generation of two different turtle scratch rhythms with distinct knee-hip synchrony patterns. In the model, these patterns are selected by changing external inputs to the interneurons, with the same synaptic weights between interneurons, and from interneurons to motoneurons, preserved for both. We showed through simulation that the proposed network can achieve the desired multi-functionality, even though it relies solely on hip unit generators to recruit appropriately timed knee extensor motoneuron activity, including the delay relative to hip flexor activation in rostral scratch. We also developed a phase space representation, focusing on the inputs to and the intrinsic slow variable of the knee extensor motoneuron. Through the use of slow phase plane arguments, we were able to explain how particular phase space and bifurcation structures underlie the generation of the rhythms and to derive sufficient conditions on these structures that guarantee the existence of stable rhythms. This analysis was possible due to time scale decomposition and certain model reductions, despite the relative high-dimensionality of the model system. Our slow phase plane framework also illustrated that a saddle-node bifurcation is a robust method for achieving the knee extensor delay in rostral, and produced a key differentiator that can be used in future experiments. The slow phase space framework also produced conditions stated in terms of dynamic structures, meaning our representation could be adapted to analyze other models that include slow, inactivating currents. Due to this more general nature, the slow phase space framework may be useful in predicting the impact of a therapeutic drug on motor patterns generated in the spinal cord. We reproduced dual-stimulation experimental results, and used our slow phase space framework to provide our collaborators with negative criteria to rule out certain parameter sets. We also predicted the effects of input scaling on motoneuron duty cycles, for future experimental testing. This work has been published in [57].

In our stochastic spiking model in Chapter 3, we investigated changes in the firing rate of motoneurons in response to modulation of excitatory and inhibitory inputs. In particular, we explored the transformation of hip interneuron signals with prescribed properties into knee extensor motoneuron output signals. We successfully produced the pocket and rostral rhythms when time-varying noise was included in the model, and we reproduced experimental results regarding input modulation and supported our collaborator's hypothesis. By exploring the roles of different model parameters, we were also able to suggest additional tests for investigating the impact of input modulation. The results in Chapters 2 and 3 are very different approaches to the same system. Both models found that inhibition was fundamental to the successful generation of multiple rhythms from the same model: the relaxation oscillator model relied on carefully structured model neuron behavior so that inhibition controlled the delay of knee extensor activity in rostral through a saddle-node bifurcation without causing issues in pocket. The stochastic spiking model supported the hypothesis that rhythmic inhibition was more important than rhythmic excitation in generating the turtle scratch rhythms through the investigation of input modulation. As more experimental work identifying the network architecture in turtle spinal cord and testing the predictions of each model is performed, the modeling approach that appears more accurate could be expanded upon. A stochastic component could be introduced to the relaxation oscillator model. It is incredibly difficult to get a phase shift such as that described in Figure 23 [51] to emerge from the interneuron architecture we have implemented (rather than being prescribed as in Chapter 3), but it may be possible with the addition of synaptic depression and all of the connections proposed in Figure 2, left. The stochastic spiking model could be more rigorously analyzed, if it proves to be the more promising modeling approach.

Our finding that hip related controls are sufficient to produce multiple knee-hip synchrony patterns may be useful in other areas, since it is essentially a statement that multiple patterns of synchrony involving multiple joints can be controlled with fewer inputs than may be expected. Additional populations could be added to this model to describe limb dynamics and feedback, as in [60]. If the model still produces multiple knee-hip synchrony patterns with these additions, this may be useful in designing more efficient control of walking robots. Finally, chapter 2 does not address many of the deletions that have been studied experimentally in turtle [5, 63, 64, 65]. Chapter 3 only finds knee extensor deletions for high frequency rhythms, but deletions are nonetheless seen experimentally and provide valuable information about underlying CPG architecture. This motivates our transition to an even simpler modeling framework in Chapter 4 to study the issues deletions raise.

In Chapter 4, we turned our attention to deletions seen during vertebrate motor function. In collaboration with the Rybak group at Drexel University, we developed a reduced mathematical model of an extensor-flexor pair in mammalian spinal cord that is capable of producing three distinct CPG mechanisms suggested by deletion experiments. Both extensor and flexor neurons were represented by single non-spiking neurons coupled by mutual inhibition. Neuronal oscillations were based on the slowly inactivating persistent sodium current. This current allowed us to induce systematic transitions between all three half-center mechanisms by manipulating external drives to each half-center. We identified three key parameters (the intrinsic state of extensor, the intrinsic state of flexor, and the strength of mutual inhibition) to vary in order to investigate the solution behaviors and frequency control that each mechanism can produce. By using a variety of two-parameter slices through this three-parameter space and exploiting the two-parameter bifurcation capabilities of XPPAUT [23], we identified several unique features of each mechanism. We also examined frequency in each of these two parameter slices, adding to our understanding of solution features produced by each mechanism. In some cases, we were able to investigate through nullcline arguments the role of escape and release transition mechanisms in producing some of these frequency results. A final note is that, in experiment and in the models presented in this thesis, the frequency of fictive rhythms is often much slower than that of intact behaviors. In the case of turtles, this is likely due to the experiemental preparation, in which turtles are anesthetized by an ice bath for several hours, lowering their temperature and slowing neuronal activity. In other animals, such as cats and mice, this of course may not be the explanation. There are a variety of constants in each model presented in this thesis that can increase the frequency of the resulting motor rhythms: the model in Chapter 2 is tuned for transitions by escape and so increasing external excitatory drive will increase the frequency of the resulting rhythm; the model in Chapter 3 is capable of tracking relatively high frequency inputs well, producing rhythms that are more on the time scale of intact behavior; and finally, the time constants used in Chapter 4 are particularly slow and come from our experimental collaborators. Changing these time constants would certainly increase the frequency of the output rhythm; whether that is biologically justified is a question for future study.

We are currently extending the extensor-flexor CPG results. We intend to further examine the three-parameter space by repeating our escape and release transition mechanism analysis in additional carefully chosen two-parameter slices. Other future approaches could include developing a quantitative cost function and sampling the three-parameter space or attempting a three-parameter bifurcation diagram. Future work investigating in a more quantifiable way how the relative contributions of escape mechanisms and release mechanisms change as parameters vary, and examining duty cycle changes in addition to frequency would also be valuable. Finally, it may be possible to apply our findings to the relaxation oscillator model of turtle scratching in Chapter 2 to account for the variety of motoneuron deletions that have been studied during turtle rostral scratching [63, 64, 65]. This may lead to changing the intrinsic nature of the motoneuron populations, or including knee-related motor pools.

BIBLIOGRAPHY

[1] Cornelia I Bargmann and Eve Marder, *From the connectome to brain function*, Nat Methods **10** (2013), no. 6, 483–490.

[2] Randall D Beer, Hillel J Chiel, and John C Gallagher, *Evolution and analysis of model cpgs for walking: Ii. general principles and individual variability*, J Comp Neurosci. **7** (1999), no. 2, 119–147.

[3] Rune W Berg, Aidas Alaburda, and Jørn Hounsgaard, *Balanced inhibition and excitation drive spike activity in spinal half-centers*, Science **315** (2007), no. 5810, 390–393.

[4] Ari Berkowitz, *Physiology and morphology of shared and specialized spinal interneurons for locomotion and scratching*, J Neurophysiol. **99** (2008), no. 6, 2887–2901.

[5] Ari Berkowitz and PS Stein, *Activity of descending propriospinal axons in the turtle hindlimb enlargement during two forms of fictive scratching: phase analyses*, J Neurosci. **14** (1994), no. 8, 5105–5119.

[6] Victoria Booth and John Rinzel, *A minimal, compartmental model for a dendritic origin of bistability of motoneuron firing patterns*, J Comput Neurosci. **2** (1995), no. 4, 299–312.

[7] Victoria Booth, John Rinzel, and Ole Kiehn, *Compartmental model of vertebrate motoneurons for ca2+-dependent spiking and plateau potentials under pharmacological treatment*, J Neurophys. **78** (1997), no. 6, 3371–3385.

[8] Amitabha Bose, Nancy Kopell, and David Terman, *Almost-synchronous solutions for mutually coupled excitatory neurons*, Physica D: Nonlinear Phenomena. **140** (2000), no. 1, 69–94.

[9] KL Briggman and WB Kristan Jr, *Multifunctional pattern-generating circuits*, Annu Rev Neurosci. **31** (2008), 271–294.

[10] T Graham Brown, *The intrinsic factors in the act of progression in the mammal*, Proceedings of the Royal Society of London. Series B, containing papers of a biological character **84** (1911), no. 572, 308–319.

[11] ———, *On the nature of the fundamental activity of the nervous centres; together with an analysis of the conditioning of rhythmic activity in progression, and a theory of the*

evolution of function in the nervous system, The Journal of Physiology **48** (1914), no. 1, 18–46.

[12] James T Buchanan and Sten Grillner, *A new class of small inhibitory interneurones in the lamprey spinal cord*, Brain research **438** (1988), no. 1, 404–407.

[13] Ansgar Büschges, *Sensory control and organization of neural networks mediating coordination of multisegmental organs for locomotion*, Journal of neurophysiology **93** (2005), no. 3, 1127–1135.

[14] Robert J Butera Jr, John Rinzel, and Jeffrey C Smith, *Models of respiratory rhythm generation in the pre-bötzinger complex. ii. populations of coupled pacemaker neurons*, J Neurophysiol. **82** (1999), no. 1, 398–415.

[15] Hillel J Chiel, Randall D Beer, and John C Gallagher, *Evolution and analysis of model cpgs for walking: I. dynamical modules*, J Comp Neurosci. **7** (1999), no. 2, 99–118.

[16] Scott N Currie and PS Stein, *Electrical activation of the pocket scratch central pattern generator in the turtle*, J Neurophysiol. **60** (1988), 2122–2137.

[17] Gennady Cymbalyuk and Andrey Shilnikov, *Coexistence of tonic spiking oscillations in a leech neuron model*, J Comp Neurosci. **18** (2005), no. 3, 255–263.

[18] Gennady S Cymbalyuk, Ronald L Calabrese, and Andrey L Shilnikov, *How a neuron model can demonstrate co-existence of tonic spiking and bursting*, Neurocomputing **65** (2005), 869–875.

[19] N Dale, *Reciprocal inhibitory interneurones in the xenopus embryo spinal cord.*, The Journal of Physiology **363** (1985), no. 1, 61–70.

[20] Silvia Daun, Jonathan E Rubin, and Ilya A Rybak, *Control of oscillation periods and phase durations in half-center central pattern generators: a comparative mechanistic analysis*, J Comput Neurosci. **27** (2009), no. 1, 3–36.

[21] J Duysens and KG Pearson, *The role of cutaneous afferents from the distal hindlimb in the regulation of the step cycle of thalamic cats*, Experimental Brain Research **24** (1976), no. 3, 245–255.

[22] Gammon M Earhart and Paul SG Stein, *Step, swim, and scratch motor patterns in the turtle*, J Neurophysiol. **84** (2000), no. 5, 2181–2190.

[23] Bard Ermentrout, *Simulating, analyzing, and animating dynamical systems: a guide to xppaut for researchers and students*, vol. 14, SIAM, 2002.

[24] G Bard Ermentrout and David H Terman, *Mathematical foundations of neuroscience*, vol. 35, Springer, 2010.

[25] Jens Peter Gabriel, Riyadh Mahmood, Alexandros Kyriakatos, Iris Söll, Giselbert Hauptmann, Ronald L Calabrese, and Abdeljabbar El Manira, *Serotonergic modulation of locomotion in zebrafish—endogenous release and synaptic mechanisms*, The Journal of Neuroscience **29** (2009), no. 33, 10387–10395.

[26] Sten Grillner, *The motor infrastructure: from ion channels to neuronal networks*, Nature Reviews Neuroscience **4** (2003), no. 7, 573–586.

[27] ———, *Biological pattern generation: the cellular and computational logic of networks in motion*, Neuron **52** (2006), no. 5, 751–766.

[28] ———, *Control of locomotion in bipeds, tetrapods, and fish*, Comprehensive Physiology (2011).

[29] Sten Grillner and Thomas M Jessell, *Measured motion: searching for simplicity in spinal locomotor networks*, Curr Opin Neurobiol. **19** (2009), no. 6, 572–586.

[30] Martin Hägglund, Kimberly J Dougherty, Lotta Borgius, Shigeyoshi Itohara, Takuji Iwasato, and Ole Kiehn, *Optogenetic dissection reveals multiple rhythmogenic modules underlying locomotion*, Proc Natl Acad Sci USA **110** (2013), no. 28, 11589–11594.

[31] Z. Z. Hao, L. E. Spardy, E. B. Nguyen, J. E. Rubin, and A Berkowitz, *Strong interactions between spinal cord networks for locomotion and scratching*, J. Neurophysiol. **106** (2011).

[32] Ronald M Harris-Warrick and Eve Marder, *Modulation of neural networks for behavior*, Annual review of neuroscience **14** (1991), no. 1, 39–57.

[33] J Hounsgaard, O Kiehn, and I Mintz, *Response properties of motoneurones in a slice preparation of the turtle spinal cord.*, J Physiol. **398** (1988), no. 1, 575–589.

[34] Auke Jan Ijspeert, *A connectionist central pattern generator for the aquatic and terrestrial gaits of a simulated salamander*, Biol Cybern. **84** (2001), no. 5, 331–348.

[35] Eugene M Izhikevich, *Dynamical systems in neuroscience*, MIT press, 2007.

[36] Patrick Jahn, Rune W Berg, Jørn Hounsgaard, and Susanne Ditlevsen, *Motoneuron membrane potentials follow a time inhomogeneous jump diffusion process*, J Comp Neurosci **31** (2011), no. 3, 563–579.

[37] Jonathan A Kahn, *Patterns of synaptic inhibition in motoneurons and interneurons during fictive swimming in the lamprey, as revealed by cl- injections*, Journal of comparative physiology **147** (1982), no. 2, 189–194.

[38] Jens Kolind, Jørn Hounsgaard, and Rune W Berg, *Opposing effects of intrinsic conductance and correlated synaptic input on vm-fluctuations during network activity*, Front Comp Neurosci. **6** (2012).

[39] Nancy Kopell and G Bard Ermentrout, *Coupled oscillators and the design of central pattern generators*, Math Biosci. **90** (1988), no. 1, 87–109.

[40] A Lundberg, *Half-centres revisited*, Regulatory functions of the CNS. Motion and organization principles (1981), 155–167.

[41] Eve Marder and Ronald L Calabrese, *Principles of rhythmic motor pattern generation*, Physiological reviews **76** (1996), no. 3, 687–717.

[42] David A McCrea and Ilya A Rybak, *Organization of mammalian locomotor rhythm and pattern generation*, Brain research reviews **57** (2008), no. 1, 134–146.

[43] Yaroslav I Molkov, Bartholomew J Bacak, and Ilya A Rybak, *Mathematical modeling and analysis of spinal circuits involved in locomotor pattern generation and frequency-dependent left-right coordination*, BMC Neuroscience **15** (2014), no. 1, 1.

[44] Yaroslav I Molkov, Bartholomew J Bacak, Adolfo E Talpalar, and Ilya A Rybak, *Mechanisms of left-right coordination in mammalian locomotor pattern generation circuits: a mathematical modeling view*, PLoS Comput Biol **11** (2015), no. 5, e1004270.

[45] Lawrence I Mortin and PS Stein, *Spinal cord segments containing key elements of the central pattern generators for three forms of scratch reflex in the turtle*, The Journal of neuroscience **9** (1989), no. 7, 2285–2296.

[46] Brian Mulloney and Carmen Smarandache, *Fifty years of cpgs: two neuroethological papers that shaped the course of neuroscience*, Frontiers in behavioral neuroscience **4** (2010), 45.

[47] Hiroshi Nishimaru, Carlos E Restrepo, and Ole Kiehn, *Activity of renshaw cells during locomotor-like rhythmic activity in the isolated spinal cord of neonatal mice*, The Journal of neuroscience **26** (2006), no. 20, 5320–5328.

[48] Morten Raastad, Bruce R Johnson, and Ole Kiehn, *Analysis of epscs and ipscs carrying rhythmic, locomotor-related information in the isolated spinal cord of the neonatal rat*, Journal of neurophysiology **78** (1997), no. 4, 1851–1859.

[49] Magnus JE Richardson, *Firing-rate response of linear and nonlinear integrate-and-fire neurons to modulated current-based and conductance-based synaptic drive*, Physical Review E **76** (2007), no. 2, 021919.

[50] Gail A Robertson, Lawrence I Mortin, Joyce Keifer, and Paul SG Stein, *Three forms of the scratch reflex in the spinal turtle: central generation of motor patterns*, J Neurophysiol. **53** (1985), no. 6, 1517–1534.

[51] GAIL A Robertson and PS Stein, *Synaptic control of hindlimb motoneurones during three forms of the fictive scratch reflex in the turtle.*, J Physiol. **404** (1988), no. 1, 101–128.

[52] Jonathan E Rubin, *Bursting induced by excitatory synaptic coupling in nonidentical conditional relaxation oscillators or square-wave bursters*, Phys Rev E **74** (2006), no. 2, 021917.

[53] Jonathan E Rubin, Natalia A Shevtsova, G Bard Ermentrout, Jeffrey C Smith, and Ilya A Rybak, *Multiple rhythmic states in a model of the respiratory central pattern generator*, J Neurophysiol. **101** (2009), no. 4, 2146–2165.

[54] Ilya A Rybak, Natalia A Shevtsova, Myriam Lafreniere-Roula, and David A McCrea, *Modelling spinal circuitry involved in locomotor pattern generation: insights from deletions during fictive locomotion*, J Physiol. **577** (2006), no. 2, 617–639.

[55] Kosei Sasaki, Vladimir Brezina, Klaudiusz R Weiss, and Jian Jing, *Distinct inhibitory neurons exert temporally specific control over activity of a motoneuron receivingconcurrent excitation and inhibition*, The Journal of Neuroscience **29** (2009), no. 38, 11732–11744.

[56] Frances K Skinner, Nancy Kopell, and Eve Marder, *Mechanisms for oscillation and frequency control in reciprocally inhibitory model neural networks*, J Comput Neurosci. **1** (1994), no. 1-2, 69–87.

[57] Abigail C Snyder and Jonathan E Rubin, *Conditions for multi-functionality in a rhythm generating network inspired by turtle scratching*, The Journal of Mathematical Neuroscience (JMN) **5** (2015), no. 1, 1.

[58] David Somers and Nancy Kopell, *Waves and synchrony in networks of oscillators of relaxation and non-relaxation type*, Physica D: Nonlinear Phenomena. **89** (1995), no. 1, 169–183.

[59] Lucy Spardy and Jonathan Rubin, *Multifunctional central pattern generators controlling turtle scratching and swimming*, in preparation.

[60] Lucy E Spardy, Sergey N Markin, Natalia A Shevtsova, Boris I Prilutsky, Ilya A Rybak, and Jonathan E Rubin, *A dynamical systems analysis of afferent control in a neuromechanical model of locomotion: Ii. phase asymmetry*, Journal of neural engineering **8** (2011), no. 6, 065004.

[61] Paul SG Stein, *Motor pattern deletions and modular organization of turtle spinal cord*, Brain research reviews **57** (2008), no. 1, 118–124.

[62] ———, *Alternation of agonists and antagonists during turtle hindlimb motor rhythms*, Ann NY Acad Sci. **1198** (2010), no. 1, 105–118.

[63] Paul SG Stein and Susan Daniels-McQueen, *Modular organization of turtle spinal interneurons during normal and deletion fictive rostral scratching*, The Journal of neuroscience **22** (2002), no. 15, 6800–6809.

[64] ———, *Timing of knee-related spinal neurons during fictive rostral scratching in the turtle*, Journal of neurophysiology **90** (2003), no. 6, 3585–3593.

[65] ———, *Variations in motor patterns during fictive rostral scratching in the turtle: knee-related deletions*, Journal of neurophysiology **91** (2004), no. 5, 2380–2384.

[66] Paul SG Stein, Margaret L McCullough, and Scott N Currie, *Spinal motor patterns in the turtles*, Ann NY Acad Sci. **860** (1998), no. 1, 142–154.

[67] Adolfo E Talpalar, Julien Bouvier, Lotta Borgius, Gilles Fortin, Alessandra Pierani, and Ole Kiehn, *Dual-mode operation of neuronal networks involved in left-right alternation*, Nature **500** (2013), no. 7460, 85–88.

[68] Sabrina Tazerart, Laurent Vinay, and Frédéric Brocard, *The persistent sodium current generates pacemaker activities in the central pattern generator for locomotion and regulates the locomotor rhythm*, J Neurosci. **28** (2008), no. 34, 8577–8589.

[69] Xiao-Jing Wang and John Rinzel, *Alternating and synchronous rhythms in reciprocally inhibitory model neurons*, Neural Comput. **4** (1992), no. 1, 84–97.

[70] James M Weimann, Pierre Meyrand, and E Marder, *Neurons that form multiple pattern generators: identification and multiple activity patterns of gastric/pyloric neurons in the crab stomatogastric system*, Journal of Neurophysiology **65** (1991), no. 1, 111–122.

[71] Guisheng Zhong, Natalia A Shevtsova, Ilya A Rybak, and Ronald M Harris-Warrick, *Neuronal activity in the isolated mouse spinal cord during spontaneous deletions in fictive locomotion: insights into locomotor central pattern generator organization*, The Journal of physiology **590** (2012), no. 19, 4735–4759.